Yrast states in the neutron-deficient isobars ^{163}W and ^{163}Ta

Thesis submitted in accordance with the requirements of the University of Liverpool for the degree of Doctor in Philosophy

by

James Thomson

Oliver Lodge Laboratory

2009

Abstract

Excited states in the neutron-deficient in ^{163}Ta and ^{163}W were investigated using the^{60}Ni + ^{106}Cd reaction at a bombarding energy of 270 MeV in an experiment using the JUROGAM and GREAT spectrometers in conjunction with the RITU gas-filled separator.

The excitation level scheme for ^{163}W has been extended significantly with the observation of five new bands. These results suggest that the negative-parity $\nu(f_{7/2}, h_{9/2})$ states form the first rotationally aligned configurations. The decay paths from the $13/2^+$ isomer to the $7/2^-$ ground state and the multipolarities of the transitions have been determined using γ-ray and conversion electron spectroscopy. This observation has allowed the relative excitation energies of single-particle $f_{7/2}$, $h_{9/2}$ and $i_{13/2}$ band heads to be fixed. In addition, the yrast band in ^{162}W has been confirmed by recoil-decay tagging and the level scheme of ^{164}W has been augmented.

The newly established level scheme for ^{163}Ta contains three strongly coupled bands establishing the excitation level scheme to high spin ($61/2\ \hbar$). The yrast band is assigned to feed the $11/2^-$ state and exhibits large signature splitting at low spin. This is discussed in terms of coupling an odd proton in the $[514]9/2^-$ Nilsson orbital to a γ-soft core. The absence of signature splitting at higher spins is interpreted in terms of aligned neutron configurations.

Configuration assignments have been based on comparisons of the deduced aligned angular momentum, as a function of rotational frequency, with the predictions of the cranked shell model. The assigned configurations are also supported, where possible, by the measured ratios of reduced transition strengths.

Acknowledgements

I acknowledge the financial support provided by the EPSRC studentship.

I would like to thank Dr David Joss for his supervision, guidance, friendship and the opportunity to spend his grant!

I would also like to thank Iain Darby, Panu Rahkila and Cath Scholey for helping me obtain spectra! A big thank you to Eddie Paul, David Joss, Robert Page, John Simpson, Neil Rowley and Rodi Herzberg for helping me understand what the spectra meant!

I would like to thank David Joss, Eddie Paul, Robert Page and Marcus Scheck for reviewing and commenting on the various drafts of this thesis.

Thanks to all of my past and present nuclear colleagues, especially the ones who shared the odd pint or football match with me!

I would also like to thank all of my collaborators, especially those located in Daresbury, Stockholm, York and JYFL.

I would like to thank Andy Mackenzie and Bruce Sinclair who were constant role models and supporters during my studies at the University of St Andrews.

I would like to thank my family, especially my parents who have been a constant source of inspiration and the odd bit of additional funding! I would also like to thank my wonderful Liverpool family, you made Liverpool home for me.

Finally I would like to thank my fiancée Natalie, your simply wonderful! I'm truly blessed just to know you Dr Taylor!

A working class hero is something to be.

John Lennon.

Contents

List of Figures

Chapter 1

Introduction to Nuclear Structure

A rich variety of phenomena has been observed to originate from the nucleus due to the interactions between its constituent nucleons. The aim of nuclear structure physics is to identify and understand the mechanisms that lead to these observations. Measuring γ-ray emissions from the nucleus is an invaluable method for determining nuclear structure. As the electromagnetic interaction is well understood the observations and measurement of γ-ray emission is directly related to changes in the underlying nuclear structure. Highly efficient multi-detector arrays and ancillary detectors have allowed the study of γ-ray emissions in many exotic nuclei that do not exist naturally on earth.

The neutron-deficient A $\sim$163 nuclei approaching the proton drip line and the $N = Z = 82$ closed shells exhibit large changes in nuclear structure over a few nucleons. This thesis is concerned with the spectroscopic study of the neutron-deficient isobars ^{163}W and ^{163}Ta. The thesis is arranged as follows. This chapter contains an introduction to the relevant aspects of nuclear structure that relate to the study of ^{163}W and ^{163}Ta. The second chapter is concerned with the experimental methodology detailing the apparatus and analysis methods.

The third chapter presents the experimental measurements and discussion of the results obtained for ^{163}W and its neighbouring isotopes. Chapter 4 reports the first observation of excited states in odd-Z nucleus, ^{163}Ta, and interprets these measurements in the context of nearby nuclei. The final chapter provides summarises the results of this research in the context of changing nuclear structure approaching the N=82 shell gap and the prospects for future work.

1.1 Shell Structure and the Mean Field

Many different models have been used in the quest to understand the nucleus. One of the earliest models of the atomic nucleus, the Liquid Drop Model (LDM) proved successful in explaining certain bulk properties of the atomic nucleus. The LDM treated the nucleus as an incompressible drop of liquid. It became apparent that there are certain physical features of the nucleus that could not be explained solely by the LDM. For example,

- the excitation energies of the first (2^+) excited states peak around certain 'magic' numbers of protons or neutrons;
- the proton and neutron separation energies drop sharply with increasing proton and neutron energies above the 'magic' numbers.

Nuclei that contained either a 'magic' number of protons or neutrons were observed to be more bound than expected from the LDM. Such discontinuities are interpreted as evidence of shell structure analogous to electronic orbitals in atoms [Ni95]. In the case of atoms, electrons move in a central potential generated by an attractive Coulomb force between the nucleus and electrons. In atomic nuclei no such central potential exists. Instead, each individual nucleon is assumed to move in a mean field generated by the interactions of all the other nucleons. The mean field approximation incorporating an effective interaction is used to create

a nuclear potential that reproduces experimental observables. Thus, if the short range interaction potential between two nucleons, i and j, is $v(r_{i,j})$ then the average potential $V_i(r_i)$ acting on each particle is

$$V_i(r_i) = \langle \sum_i v(r_{i,j}) \rangle. \tag{1.1}$$

The Hamiltonian $\hat{H}$ becomes

$$\hat{H} = \sum_i T_i + \frac{1}{2} \sum_{ij} v(r_{i,j}) \tag{1.2}$$

where T_i is the kinetic energy of a single nucleon. Restricting to two-body interactions only [Hey90], the Hamiltonian can be rewritten as

$$\hat{H}' = \sum_i [T_i + V_i(r_i)] + \lambda [\frac{1}{2} \sum_{ij} v(r_{i,j}) - \sum_i V_i(r_i)], \tag{1.3}$$

where H' is the perturbed Hamiltonian and the second term describes residual interactions and λ quantifies the strength of the residual interactions. The mean field shell model assumption is that $\lambda \rightarrow 0$, thus the central potential is much larger than the residual interactions, which can be treated as a perturbation. The nuclear many-body problem is complicated. However, by assuming different potentials and modifying them to make them realistic, the structure of the nucleus can be modelled.

1.2 The Harmonic Oscillator Potential

The harmonic oscillator potential is a useful starting point for nuclear models due to its analytical simplicity. That is to say the solutions of the harmonic oscillator can be written in a closed form. The potential describes the presence of a restoring force that acts to return a system to an equilibrium condition. The potential is defined as,

$$V_{HO}(r) = \frac{m\omega_0{}^2 r^2}{2}, \tag{1.4}$$

and so the Hamiltonian can be written as,

$$\widehat{H}_{HO} = -\frac{h^2}{2m}\nabla^2 + \frac{m{\omega_0}^2 r^2}{2}, \tag{1.5}$$

where ω_0 is the oscillator frequency and r the displacement from the centre of the potential. The energy eigenvalues are then given by

$$E_{nl} = \hbar\omega_0\left(N + \frac{3}{2}\right) = \hbar\omega_0\left(2n + l + \frac{3}{2}\right), \tag{1.6}$$

where l represents the angular momentum quantum number and n the number of nodes in the wavefunction. The energy levels are evenly spaced and have a degeneracy given by

$$\frac{1}{2}(N+1)(N+2). \tag{1.7}$$

where N represents the principal quantum number and oscillator shell. Each oscillator shell contains states of the same parity,

$$\pi = (-1)^N = (-1)^l \tag{1.8}$$

where each N level is $(N+1)(N+2)$ degenerate. States are grouped such that,

$$l = N, N-2, N-4..... \tag{1.9}$$

Using Eq. 1.8 and Eq. 1.9 the states that contribute to each oscillator shell can be identified. For example the $N = 5$ shell will contain degenerate states with $l = 5, 3$ and 1. This corresponds to the $1h$, $2f$ and $3p$ states, which contain 22, 14 and 6 degenerate nucleons, respectively. The harmonic oscillator is useful for replicating certain characteristics of nuclei. The potential produces 'magic' numbers of protons and neutrons, though these are somewhat different to those observed. Also the harmonic oscillator potential fails to replicate the range of the nuclear force since $V_{HO}(r) \to \infty$ as $r \to \infty$.

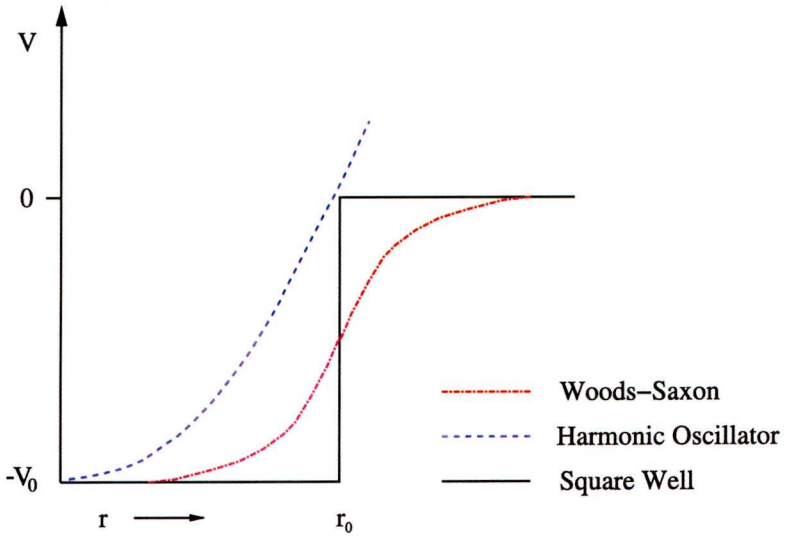

Figure 1.1: Comparison between the harmonic oscillator, Woods-Saxon and square well potentials [Paul07]

1.3 The Woods-Saxon Potential

The Woods-Saxon potential is thought to be a more realistic potential [WS54]. The Woods-Saxon potential is defined such that $V(r) \rightarrow 0$ when $r > R_0$,

$$V_{ws}(r) = \frac{-V_0}{1 + \exp[\frac{r-R_0}{a}]}. \tag{1.10}$$

Since nucleons at the centre of the potential experience no net force ($\partial V/\partial r = 0$) a flat-bottomed potential is desirable. The Woods-Saxon potential approximates this feature. The R_0 term represents the radius and can be approximated as $R_0 = r_0 A^{1/3}$ with r_0=1.2 fm. The a term in Eq. 1.10 represents the surface diffuseness. The potential depth is V_0, which can be adjusted to fit experimentally measured observables. Typically (V_0) $\approx$ 50MeV and $a \approx$ 0.5 fm. The 'magic numbers' extracted from the Woods-Saxon potential, like the harmonic oscillator potential, are different from those observed experimentally. The Woods-Saxon potential is compared with the harmonic oscillator and square potential in Fig. 1.1.

1.4 The Spin-Orbit Interaction

The spin-orbit interaction was introduced so that the correct magic numbers could be extracted from the shell model [Hax49, Ma49]. To incorporate the spin-orbit interaction a term is added to the potential such that,

$$V(r) \rightarrow V(r) + \mu(r)\underline{l}.\underline{s}. \tag{1.11}$$

A negative μ term is required to reproduce the correct 'magic numbers'. The consequence of the spin-orbit term is to remove the degeneracy of states with the same l value. The spin-orbit interaction is attractive, states with $j = l + \frac{1}{2}$ are more tightly bound (lower in energy) than the $j = l - \frac{1}{2}$ states. The Woods-Saxon potential with the spin-orbit interaction included is then

$$V_{ws+so}(r) = \frac{-V_0}{1 + \exp[\frac{r-R_0}{a}]} + \mu(r)\underline{l}.\underline{s}. \tag{1.12}$$

The nuclear Hamiltonian including the spin-orbit term is then written as,

$$\widehat{H} = -\frac{h^2}{2m}\nabla^2 + \frac{-V_0}{1 + \exp[\frac{r-R_0}{a}]} + \mu(r)\underline{l}.\underline{s}. \tag{1.13}$$

It can be seen that the spin-orbit term is proportional to l. High-j ($j = l + s$) states are more tightly bound and can even 'intrude' into the lower oscillator ($N-1, N-2, ...$) shells. Such states have different parity to the neighbouring states and are termed 'intruders'. Figure 1.2 shows how the degeneracy of the spherical shell model states is relieved by adding an $l.s$ term to the Hamiltonian. The degeneracy of these states is further effected by increasing nuclear deformation and rotation.

1.5 Definition of the Nuclear Shape

The nuclear surface must be parameterised to represent dynamical shape or surface oscillations. The nuclear shape is parameterised using the β deformation

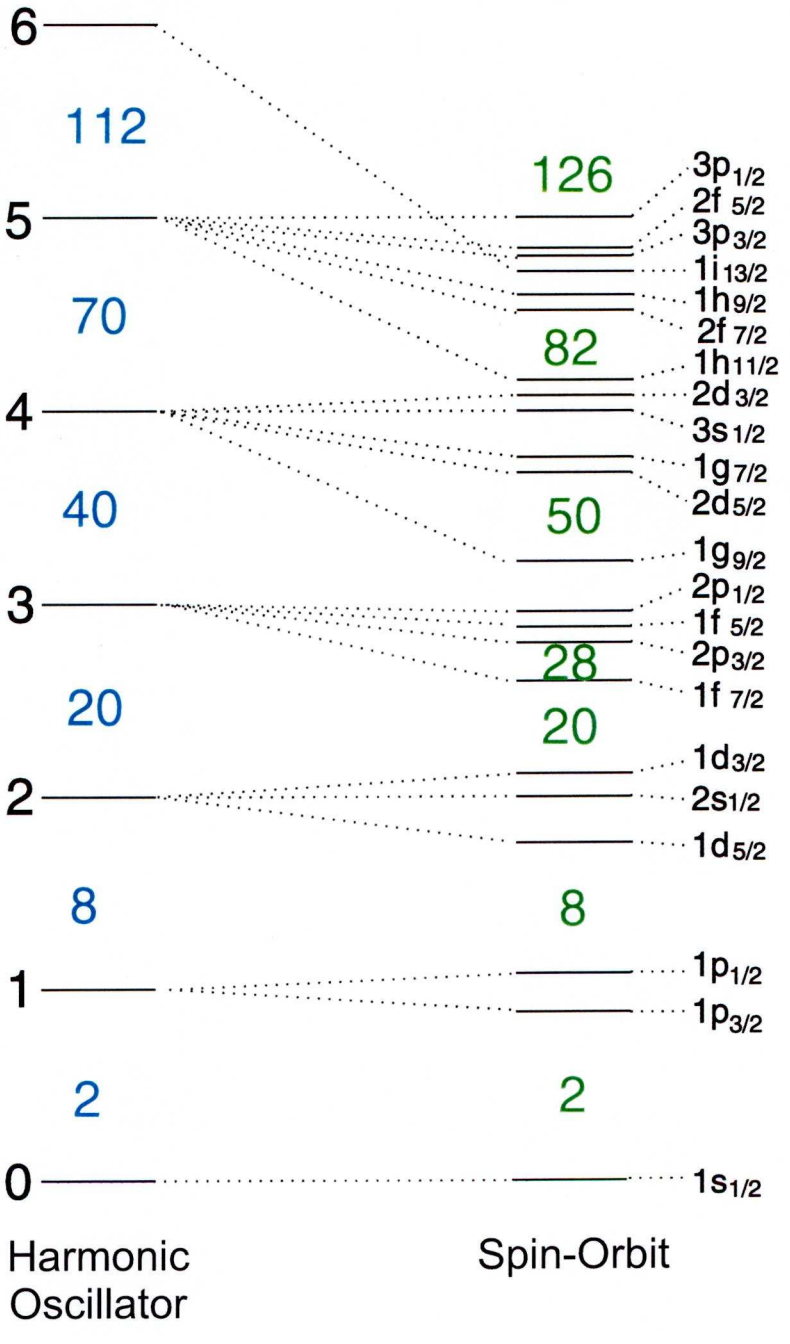

Figure 1.2: Modification of the harmonic oscillator potential allows calculation of the correct magic numbers [Paul07].

parameter for the Wood-Saxon potential, which is analogous to the to the ε used in the Anisotropic Harmonic Oscillator model. The β parameter originates by

specifying the length of a radius vector pointing from the origin to the surface,

$$R(\theta,\phi) = R_0\left(1 + \alpha_{00} + \sum_{\lambda=1}^{\infty}\sum_{\mu=-\lambda}^{\lambda}\alpha_{\lambda\mu}Y_{\lambda\mu}(\theta,\phi)\right), \tag{1.14}$$

where R_0 specifies the radius of a sphere that would have the same volume as the deformed ellipsoid and α_{00} is introduced to conserve volume. The radius vector in Eq. 1.14 is defined in terms of the spherical harmonics $Y_{\lambda\mu}(\theta,\phi)$ and volume changes $\alpha_{\lambda\mu}$ where λ defines the deformation type. For quadrupole deformations ($\lambda = 2$) there are five $\alpha_{\lambda\mu}$ parameters. Three of the parameters represent Euler angles and can be removed by transforming the body-fixed system so that it corresponds to the principal axes of the mass distribution. The five coefficients $\alpha_{2\mu}$ are then reduced to two independent variables α_{20} and $\alpha_{22} = \alpha_{2-2}$ that completely define the system spatially. It is convenient to express $\alpha_{2\mu}$ in an alternative polar coordinate parameterisation using β_2 and γ (the Hill-Wheeler coordinates) through the relation,

$$\alpha_{20} = \beta_2 \cdot \cos\gamma, \tag{1.15}$$

$$\alpha_{22} = \frac{1}{\sqrt{2}}\beta_2 \cdot \sin\cdot\gamma, \tag{1.16}$$

such that,

$$\sum_{\mu}|\alpha_{2\mu}|^2 = \alpha_{20}^2 + 2\alpha_{22}^2 = \beta_2^2. \tag{1.17}$$

1.6 The Deformed Shell Model

The existence of large quadrupole moments and rotational bands indicate the existence of stable ground state deformations in nuclei. Correlated nucleonic motion occurs through the long range residual interactions of the nucleon-nucleon force. Such long-range correlations are not included in the central potential created by the short-range nucleon-nucleon interactions or in the spin-orbit correction. As the number of valence nucleons increases the suitability of the spherical shell

model potential diminishes. Nilsson proposed a model in which the potential was deformed to take into account the long-range residual interactions and the quadrupole moments. The onset of deformation relieves the degeneracy of the spherical shell model with important consequences for nuclear structure.

1.6.1 The Anisotropic Oscillator or Nilsson Model

It is assumed that the nuclear density distribution and therefore the mean field potential is ellipsoidal. The deformed average nuclear potential may be described by an anisotropic oscillator potential [Nil55]

$$V_{AHO} = \frac{1}{2}M(\omega_x{}^2x^2 + \omega_y{}^2y^2 + \omega_z{}^2z^2). \tag{1.18}$$

The potential can be separated into solvable 1-D potentials in x, y and z. Here $\omega_{x,y,z}$ are the one-dimensional oscillator frequencies and are chosen such that $\omega_v \propto \omega_0(R_0/a_v)$, where $a_v(v = x, y, z)$ is the half axis of the ellipsoid. This potential can be simplified for the case of axially symmetric shapes

$$V_{AHO} = \frac{1}{2}M\omega_\perp{}^2(x^2 + y^2) + \omega_z{}^2z^2. \tag{1.19}$$

Here the z-axis defines the deformation axis. In the axially symmetric case,

$$\omega_x = \omega_y = \omega_\perp = \omega_0(\delta)\left(1 + \frac{1}{3}\delta\right), \tag{1.20}$$

$$\omega_z = \omega_0(\delta)\left(1 - \frac{2}{3}\delta\right), \tag{1.21}$$

where δ is a deformation parameter defined as $\delta = (\Delta R/R_0)$. Here ΔR is the difference between the radii parallel and perpendicular to the symmetry axis and R_0 is the mean radius. Volume conservation is taken care of by the following,

$$\omega_x\omega_y\omega_z = \omega_0{}^3 \text{and } \omega_0 = \left(1 - \frac{4}{3}\delta^2 - \frac{16}{27}\delta^3\right)^{-\frac{1}{6}}. \tag{1.22}$$

The oscillator frequency ω_0 has an isospin and mass number dependence,

$$\hbar\omega_0 = 41A^{-1/3}[1 \pm \frac{(N-Z)}{3A}]\,(MeV)\,. \tag{1.23}$$

The introduction of 'stretched' coordinates [Ni69a, Ni69b] allows the potential to be calculated in terms of ε_2,

$$V_{AHO} = \frac{1}{2}\hbar\omega(\varepsilon_2)\rho^2[1 - \frac{2}{3}\varepsilon_2 P_2(\cos\theta_t)]. \tag{1.24}$$

The ρ^2 relates to the sum of the squares of stretched coordinates and θ_t is the angle in stretched coordinates. Higher multipoles of deformation can be added to Eq.1.24 by adding terms proportional to $\varepsilon_\lambda \rho^2 P_\lambda(\cos\theta_t)$.

The solutions of the modified oscillator are

$$E_{n_z,n_\perp} = \left(n_z + \frac{1}{2}\right)\hbar\omega_z + (n_\perp + 1)\,\hbar\omega_\perp \tag{1.25}$$

or in terms of deformation, δ,

$$E_{N,n_z,n_\perp} \approx \left(N + \frac{3}{2}\right)\hbar\omega_0 - \frac{1}{3}\delta\,(2n_z - n_\perp)\,\hbar\omega_0, \tag{1.26}$$

where $N = n_{/bot} + n_z$. In the limit where $\delta \to 0$ the spherical harmonic energies are calculated. Nilsson added terms proportional to the spin-orbit term $l.s$ and an l^2 term to flatten the potential. The resulting potential is

$$V_{nil} = V_{AHO} - \kappa\hbar\omega[2l.s + \mu(l^2 - \langle l^2\rangle_N)]. \tag{1.27}$$

The κ and μ terms are adjustable parameters and vary for each different oscillator shell. These coefficients can be chosen by fitting to experimental energies.

The Nilsson states are typically labelled as

$$\Omega^\pi[Nn_z\Lambda], \tag{1.28}$$

where $\Omega = \Sigma + \Lambda$ is the total projection of the single-particle angular momentum j on the symmetry axis. The Σ term represents the single-particle spin angular

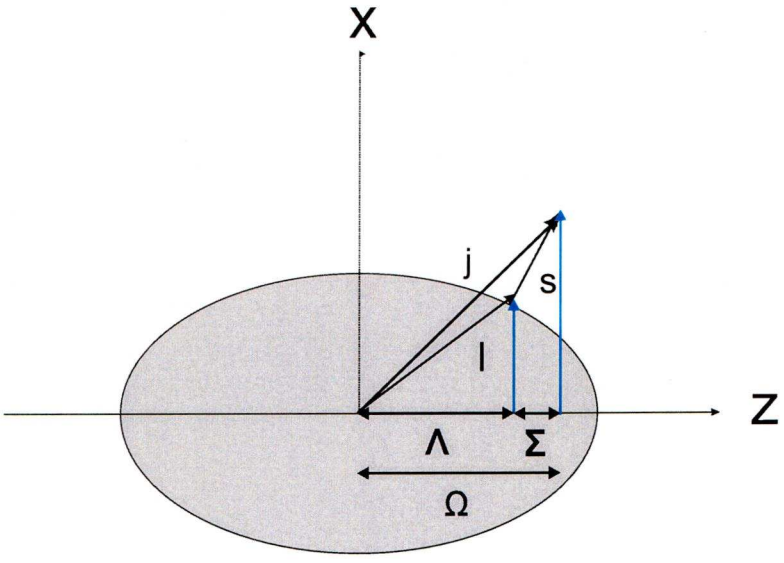

Figure 1.3: Graphical representation of the quantum numbers used as Nilsson labels [Paul07].

momentum projection on the symmetry axis and Λ is the single-particle orbital angular momentum projection on the symmetry axis. The projections of j and l are good quantum numbers in the deformed regime unlike the quantities themselves. The N represents the total number of oscillator quanta, n_z is the number of oscillator quanta along the z-axis. The parity of the state is represented by π. Some of the quantum numbers are represented graphically in Fig.1.3

1.6.2 Deformed Woods-Saxon Potential

In order to make the anisotropic oscillator potential realistic an l^2 term is required to reproduce a flat-bottomed potential. Gustafson *et al.* found that states with high oscillator numbers N, shift the single-particle energies too much [GLN67]. An l^2 term is not required with a deformed Woods-Saxon. Thus, the deformed Woods-Saxon potential reproduces the single-particle state energies better in heavier nuclei. The surface diffuseness is described by the a parameter is roughly constant among spherical nuclei. To obtain such a constant surface diffuseness in

deformed nuclei requires that a has a dependance on the θ and ϕ angles [BM75] [Br72].

$$V(r,\theta,\phi) = -V_0 \left[1 + \exp\left(\frac{\mathrm{r} - \mathrm{R}(\theta,\phi)}{\mathrm{a}(\theta,\phi)}\right)\right]^{-1}, \tag{1.29}$$

The spin-orbit interaction term is added to the Hamiltonian to reproduce the correct magic numbers.

$$\hat{H} = -\frac{\hbar}{2m}\nabla^2 + V_{DWS} - f(r)\mathrm{l.s}, \tag{1.30}$$

Deformed Woods-Saxon potentials are used in the quasiparticle cranking calculations reported in Chapters 4 and 5.

1.7 The Cranked Shell Model

The cranked shell model provides a fully microscopic description of single nucleon motion in a rotating potential generated by all the other nucleons. The cranked shell model incorporates the effects of the Coriolis and centrifugal forces in relieving the two-fold degeneracy of the deformed shell model states [Ing54]. The transformation from the laboratory frame to the rotational frame occurs via the rotational operator $\widehat{R}$,

$$\widehat{R} = \exp\left[\frac{-i\omega t j_x}{\hbar}\right], \tag{1.31}$$

The wavefunction in the rotating frame, Ψ_{rot} can therefore be related to the laboratory frame wavefunction Ψ_{lab} via

$$\Psi_{rot} = \widehat{R}\Psi_{lab} = \exp\left[\frac{-i\omega t j_x}{\hbar}\right]\Psi_{lab}, \tag{1.32}$$

The Schrödinger equation in the rotating frame is,

$$\widehat{H}_{rot}\Psi_{rot} = -i\hbar\frac{d\Psi_{rot}}{dt}, \tag{1.33}$$

Differentiation of Eq. 1.32 and substitution into Eq. 1.33 gives the cranking Hamiltonian as,

$$\widehat{H}_{rot} = \widehat{H}_{lab} - \omega j_x. \tag{1.34}$$

The $\widehat{H}_{rot}$ term describes the Hamiltonian in the laboratory system which is defined by a deformed single-particle potential, for example a deformed Woods-Saxon potential. The $-\omega j_x$ term incorporates the effects of the Coriolis and centrifugal forces on the nucleon energy and has a different sign depending on whether the nucleon is moving in with or against the collective core rotation. Thus, the degeneracy of the deformed shell model states and time reversal symmetry are broken by rotational forces resulting in two states of opposite signature, α. The $-\omega j_x$ term has a dependence on the spatial orientation of the nucleon with respect to the core leading to variations in the degree of signature splitting for orbits with different Ω projections.

The eigenvalues of the single-particle cranking Hamiltonian are known as routhians, e' [Beng79]. They are defined as,

$$e' = \langle u|\widehat{H}_{rot}|u\rangle, \tag{1.35}$$

where

$$\langle u|\widehat{H}_{rot}|u\rangle = \langle u|\widehat{H}_{lab}|u\rangle - \omega\langle u|j_x|u\rangle, \tag{1.36}$$

and

$$e' = e - \omega j_x, \tag{1.37}$$

where u represents the eigenstates of the cranking Hamiltonian and e is the single-particle energy in the laboratory frame. The total energy in the rotating frame is represented by the sum of the energies of all occupied orbits in addition to the centrifugal and Coriolis contributions represented by the $-\omega j_x$ terms.

$$E = \sum_u e'_u + \omega \sum_u \langle u|j_x|u\rangle, \tag{1.38}$$

$$I_x = \sum_u \langle u|j_x|u\rangle \approx I, \tag{1.39}$$

since for high spin, $I_x \rightarrow I$. The slope of the routhians are directly related to the single-particle alignment, i_x such that,

$$\frac{de'}{d\omega} = -\langle u|j_x|u\rangle \approx = i_x. \tag{1.40}$$

1.7.1 Comparison with Experimental Data

In classical mechanics the energy of rotation is proportional to the angular frequency squared

$$E = \frac{1}{2}\left(\sum_i m_i r_i^2\right)\omega^2. \tag{1.41}$$

The quantity in parentheses is the rotational inertia $J^{(0)}$, where m_i are point masses at a distance r_i from the rotation axis. Classical observables in have analogous quantum definitions. For example, the analogous quantum expression for the rotational energy can be calculated from

$$E = \frac{\hbar^2}{2J^{(0)}} I(I+1). \tag{1.42}$$

The static rotational moment of inertia $J^{(0)}$ for nuclei is lower than that expected assuming a rigid body. Therefore it is useful to define two other quantities to express changes in the rotational moment of inertia as the nucleus undergoes rotation. The kinematic moment of inertia [BM81] is defined as

$$\frac{\hbar I}{\omega} = J^{(1)} = I\hbar^2 \left(\frac{dE}{dI}\right)^{-1} \tag{1.43}$$

The kinematic moment of inertia is particularly useful where the spins of all the states involved are known. In cases where the spin is unknown a more useful quantity is that of the dynamic moment of inertia [BM81],

$$J^{(2)} = I\hbar^2 \left(\frac{d^2E}{d^2I}\right)^{-1} = \hbar\frac{dI}{d\omega}. \tag{1.44}$$

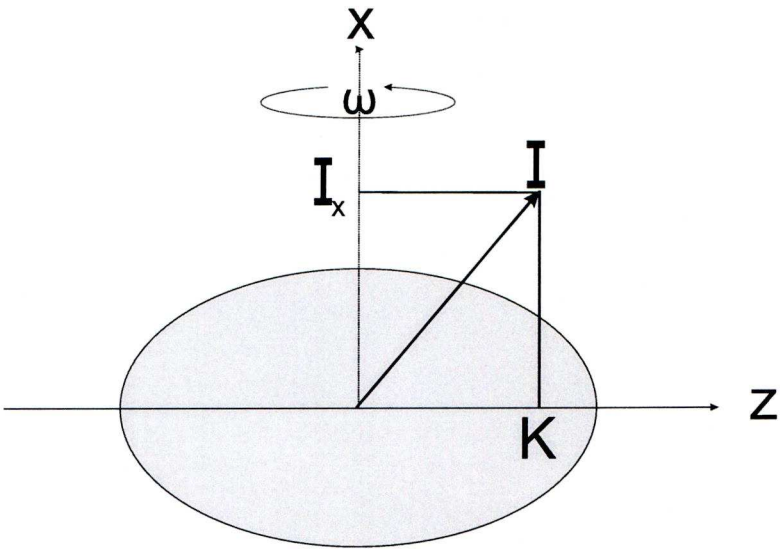

Figure 1.4: The projection of the total spin on the symmetry axis is labelled K in the diagram. The projection of the total spin of the rotation axis is labelled I_x in the diagram.

To aid configuration assignments for collective structures, it is useful to plot parameters extracted from the level schemes as a function of rotational frequency e.g. the Routhians, e' versus the rotational frequency, $\hbar\omega$. The rotational frequency about the x-axis can be obtained via

$$\hbar\omega = \frac{dE(I)}{dI_x}, \tag{1.45}$$

and can be calculated from the γ-ray transition energies using

$$\hbar\omega = \frac{E(I_{x_2}) - E(I_{x_1})}{I_{x_2} - I_{x_1}}. \tag{1.46}$$

In the case of a transition within a rotational band (cascade of E2 transitions) this can be simplified to

$$\hbar\omega = \frac{E_\gamma}{2}. \tag{1.47}$$

The experimental aligned angular momentum I_x, is defined as the projection of the total angular momentum onto the rotation axis and is given by

$$I_x = \sqrt{I(I+1) - K^2}, \tag{1.48}$$

as shown in Fig 1.4. The K quantum number is the projection of the total angular momentum on the symmetry axis. Sometimes it is helpful to compare experimental alignment gains with the predictions of the cranked shell model. In this scenario it may be helpful to subtract a rotational reference. For example, if the yrast states of the ground state band are to be used as a reference an extrapolation to higher ω values is required. The low-spin members of the ground state band are fitted using the formula which approximates the relationship between energy and spin detailed by Harris [Har65] where the reference alignment I_{ref} is defined as

$$I_{ref} = \left(J_0 + \omega^2 J_1\right)\omega \tag{1.49}$$

The constants J_0 and J_1 are known as the Harris parameters. The reference Routhian is the negative integral, with respect to rotational angular frequency ω,

$$e'_{ref}(\omega) = -\frac{1}{2}\omega^2 J_0 - \frac{1}{4}\omega^4 J_1 + \frac{1}{8J_0} \tag{1.50}$$

The use of this relationship can be justified for 'good' rotors. Typically, a 'good' rotor is well deformed with a high moment of inertia. Transitional nuclei are located between the mid-shell and closed shell regions and may be triaxial. In these instances, Eq. 1.50 should be applied with caution since higher-order terms in the expansion [Har65] may increase in significance as the moment of inertia increases. Furthermore, K is no longer a good quantum number for triaxial shapes.

1.7.2 Symmetries of the Rotating Nucleus

There are symmetries in a rotating system described by $\hat{H}_{rot}$. The intrinsic wavefunctions of reflection symmetric systems are invariant with respect to space inversion, denoted by the operator $\hat{P}$. This defines parity as a good quantum number, where the total parity of a quasiparticle configuration is given by,

$$\pi_{tot} = \prod_i \pi_i. \tag{1.51}$$

The cranking Hamiltonian is invariant with respect to rotation by 180° (π radians), denoted by the operator $\hat{R}_x$. The rotational invariance is represented by

$$\hat{R}_x \psi_i = exp(-i\pi j_x)\psi_i, \tag{1.52}$$

where ψ_i represent the single-particle wavefunctions. The eigenvalues of $\hat{R}_x$ are $\exp(-i\pi j_x)$, where α is the signature exponent quantum number. The signature quantum number is defined as,

$$r = exp(-i\pi\alpha) \tag{1.53}$$

The eigenvalues restrict the spin sequences to the following values,

$\alpha = +1/2$	$r = -i$	I = 1/2, 5/2, 9/2, ...
$\alpha = -1/2$	$r = +i$	I = 3/2, 7/2, 11/2, ...
$\alpha = 0$	$r = +1$	I = 0, 2, 4, ...
$\alpha = 1$	$r = -1$	I = 1, 3, 5, ...

The total signature of a configuration is given by,

$$\alpha_{tot} = \sum_i \alpha_i. \tag{1.54}$$

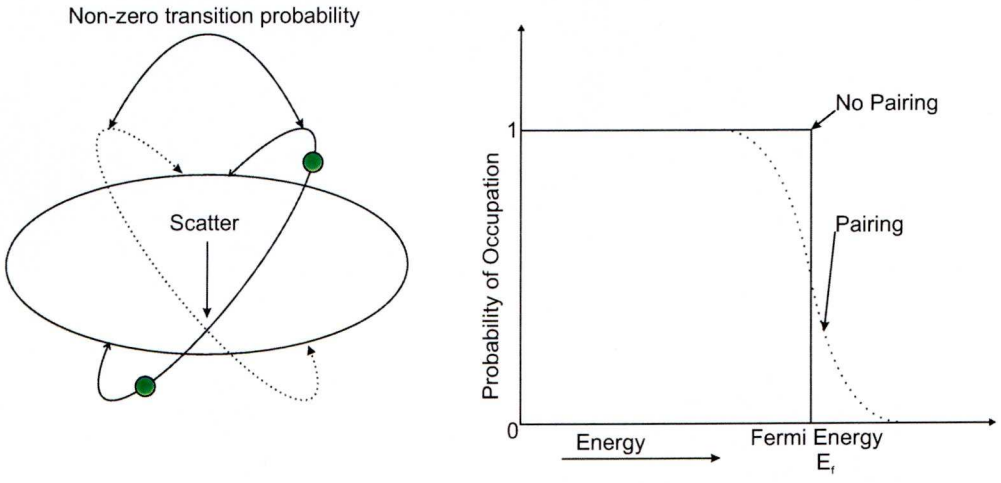

Figure 1.5: The occupation of time-reversed orbits has the consequence that pairs of nucleons will interact twice per orbit and scatter into other time-reversed orbitals. The probability of occupation becomes smeared around the Fermi surface.

The staggering parameter $S(I)$ is a method of comparing the experimental differences in energy between the signature partners in odd-A nuclei. For axially symmetric nuclei, the staggering parameter should be zero i.e. the excited states of one band lie at the mid-point of the those in the signature partner. Deviations from zero signature splitting are represented by oscillations in the values of the staggering parameter about zero. These are usually interpreted as being indicative of nuclear shapes where the primary axes are all of different lengths (triaxial).

1.7.3 Pairing and rotation

There is experimental evidence that suggests the existence of an attractive residual interactions between pairs of nucleons. Evidence for pairing has been inferred from physical osbervations such as the odd-even mass differences and the 0^+ ground states of even-even nuclei. Due to the fermion nature of nucleons, the orbits through which nucleon wavefunctions can achieve the greatest overlap are

those that maintain time reversal symmetry. Time reversal symmetry describes the existence of simultaneously occupied angular momentum states $|j_{\nu 1}, \Omega_{\nu 1}\rangle$, and the time reversed symmetric partner $|j_{\nu 1}, \Omega_{\bar{\nu 1}}\rangle$. A consequence of time reversal symmetry is that the paired nucleons couple to $I = 0\hbar$, which is consistent with the $0\hbar$ ground states observed in even-even nuclei.

Far below the Fermi surface the occupation probability is unity and the 'scattering' of states is forbidden due to the Pauli-exclusion principle. This is the main justification for mean-field treatments where the nucleons are considered to be non-interacting. A further consequence of time reversed state occupation is that the states scatter twice in each orbit into different pairs of time-reversed orbits. The only vacant states exist above the Fermi surface. This leads to the occupation probability around the Fermi surface becoming smeared Fig 1.5.

Pairing correlations obscure the clear definition of particle-hole states and it becomes appropriate to discuss excitations in terms of particle-hole occupation probabilities. The Hartree-Fock-Bogoliubov formalism allows the effects of pairing to be incorporated in the cranked shell model and is detailed in the following section.

1.7.4 HFB formalism and Quasiparticles

The Hartree-Fock-Bogoliubuv (HFB) formalism originates from an analogy drawn between the motion and dynamics of Cooper pairs in superconducting metals and nucleonic motion [BMP58]. Bohr, Mottelson and Pines argued that the monopole pairing force which couples nucleons into pairs with zero angular momentum were similar in nature to the Cooper effect [BMP58].

The HFB formalism includes a two-body monopole pairing interaction in the nuclear Hamiltonian. The Hamiltonian including a two-body monopole (i.e. $I =$

0) can be written as,

$$\widehat{H} = \widehat{H}_{DWS} + \widehat{H}_{Res}, \tag{1.55}$$

$$\widehat{H} = \sum_{\nu>0} \epsilon_\nu [a_\nu{}^\dagger a_\nu + a_{\bar{\nu}}{}^\dagger a_{\bar{\nu}}] - G \sum_{\nu 1,\nu 2} a_{\nu 1}{}^\dagger a_{\bar{\nu} 1}{}^\dagger a_{\nu 2} a_{\bar{\nu} 2}, \tag{1.56}$$

where $a_{\bar{\nu}}$ and a_ν are the creation and annihilation operators and G is the two-body interaction strength. The first term in Eq. 1.56 is the sum of single-particle energies ϵ_ν and describes the motion of of nucleons up to the Fermi surface in a deformed Woods-Saxon potential. The second term in Eq. 1.56 describes the pairing interaction that annihilates a pair of nucleons in the state $\mid \nu_2\rangle$ and time reversed partner $\mid \bar{\nu}_2\rangle$ and creates a pair of nucleons in different time reversed states $\mid \nu_1\rangle$ and $\mid \bar{\nu}_1\rangle$. The two-body monopole pairing interaction can be rewritten as,

$$\widehat{H}_{Res} = -GP^\dagger P, \tag{1.57}$$

where $P^\dagger$ and P are the pair creation and annihilation operators are defined as

$$P^\dagger = \sum_\nu a_\nu^\dagger a_{\bar{\nu}}^\dagger, \tag{1.58}$$

$$P = \sum_\nu a_{\bar{\nu}} a_\nu. \tag{1.59}$$

For analytical simplicity, the pairing interaction is defined in terms of the energy increase of the condensate per particle added by defining the chemical potential λ such that,

$$\widehat{H}_{Res} = -\frac{1}{2}\Delta[P^\dagger + P] - \lambda \hat{N}, \tag{1.60}$$

where $\hat{N}$ is the particle number operator and Δ is the pair-gap parameter that quantifies the magnitude of the pairing interaction. The form of Eq. 1.60 allows the pair creation and annihilation operators to be treated separately rather than simultaneously as in Eq. 1.57. To conserve the number of particles the chemical

potential λ must be used as a Lagrange multiplier. Another simplification of the pairing interaction is achieved by treating the nucleus as a non-interacting gas of quasiparticles. Quasiparticles are mathematical constructions that describe excitations in terms of linear combinations of particle and hole occupation probabilities. Using the quasiparticle construct the particles can be replaced by non-interacting quasiparticles whose energies are additive. The transformation between the particle $(a^\dagger, a)$ and quasiparticle $(\alpha^\dagger, \alpha)$ basis is accessible via the Bogoliubov-Valatin transformation,

$$\alpha_\nu{}^\dagger = U_\nu a_\nu^\dagger + V_\nu a_{\bar{\nu}}, \tag{1.61}$$

$$\alpha_{\bar{\nu}} = U_\nu a_{\bar{\nu}}^\dagger - V_\nu a_\nu. \tag{1.62}$$

The coefficients U_ν and V_ν are defined in terms of by the minimisation of expectation values of $\hat{H}$ according to the Hartree-Fock method and applying the constraint,

$$|U_j|^2 + |V_j|^2 = 1. \tag{1.63}$$

.

The energy eigenvalues in the quasiparticle basis are defined as,

$$E_\nu = \pm\sqrt{(\varepsilon_\nu - \lambda)^2 + \Delta^2}, \tag{1.64}$$

where ε_ν is the quasiparticle energy, Eq. 1.64 suggests that for each single-particle level there are two quasiparticle levels, one positive and the other negative. These levels are reflections of each other about the Fermi surface. The HFB formalism can be applied to the cranking Hamilitonian to give quasiparticle excitations in the rotating frame. In a cranking context, the Hamiltonian is modified such that,

$$\hat{H}_{quasi} = \hat{H}_{Lab} - \hbar\omega j_x - \Delta(P^\dagger + P) - \lambda\hat{N}. \tag{1.65}$$

The eigenvalues of $\hat{H}_{quasi}$ are the quasiparticle Routhians.

1.8 Electromagnetic Transitions

Electromagnetic transitions in atomic nuclei can occur by the emission of γ rays and internal conversion electrons. Since the nucleus contains discrete charged particles all transitions take place in an associated electromagnetic field. The inclusion of electromagnetic fields into the nuclear Hamiltonian gives,

$$\hat{H} = \hat{H}_{Model} + \hat{H}_{Field} + \hat{H}', \tag{1.66}$$

where $\hat{H}_{Model}$ is the shell model Hamiltonian, $\hat{H}_{Field}$ is the Hamiltonian of the electromagnetic field and $\hat{H}'$ is a time dependent perturbation describing the interaction between the field and the nucleus. If two states (ψ_1 and ψ_2) are connected by a transition then there will be a non-zero matrix element,

$$< \psi_1 | H' | \psi_2 > \neq 0. \tag{1.67}$$

The transition probability per unit time, assuming the interaction relating the states is small, is given by Fermi's Golden Rule [Di27],

$$T_{1\rightarrow 2} = \frac{2\pi}{\hbar} | < \psi_1 | H' | \psi_2 > |^2 \rho_E, \tag{1.68}$$

where ρ_E is the density of final states.

1.8.1 Gamma-ray emission

The observation of excited states and the transitions between them are of fundamental importance in the quest to understand nuclear structure. Gamma-ray emission is an electromagnetic perturbation and can be defined as an infinite series or multipole expansion. The terms in the multipole expansion represent the multipole moments, which have either electric or magnetic character leading to the definition,

$$\hat{H}' = \sum_{\lambda,\mu} a_{\lambda,\mu} Q_{\lambda\mu} + b_{\lambda,\mu} M_{\lambda,\mu}, \tag{1.69}$$

where $Q_{\lambda\mu}$ and $M_{\lambda,\mu}$ are the electric and magnetic operators, respectively. The electromagnetic moments originate from charge distributions and current densities in the nucleus. Hence deviations from sphericity will impact dramatically on the underlying nuclear structure as indicated by changes in Eqs. 1.66, 1.67, 1.68, 1.69. The application of appropriate gamma-ray spectroscopy techniques permits the measurement of experimental observables such as the parity, spin and lifetime of an excited state.

1.8.2 Selection Rules and Transition Strengths

The conservation of angular momentum restricts the possible multipolarities of γ-ray transitions connecting excited states such that,

$$|I_i - I_f| \leq L \leq |I_i + I_f| (L \neq 0), \tag{1.70}$$

where L denotes the transition multipolarity and I_i and I_f denote the spins of the initial and final states, respectively. The electromagnetic interaction is parity conserving. Thus transitions are constrained by an additional selection rule,

$$\pi_i \pi_f = \pi_L, \tag{1.71}$$

where π_i and π_f are the respective parities of the initial and final states. The parity is intimately related to the multipole operators yielding the relations,

$$\pi(EL) = (-1)^L \tag{1.72}$$

$$\pi(ML) = (-1)^{(L+1)} \tag{1.73}$$

Often there are several 'allowed' γ-ray transitions between states. Thus the transitions are not always characterised by a single polarisation and multipolarity but have a 'mixed' nature instead. Electric and magnetic transition rates have been calculated in terms of rotating multipoles [BM75]. The possibility of electric

Table 1.1: Transition strengths expressed in terms of the reduced transition strengths B($\sigma\lambda$) where σ represents the polarisation and λ represents the transition multipolarity. The units of B($E\lambda$) are expressed in $e^{\lambda}fm^{2\lambda}$, B($M\lambda$) are expressed in $\mu_N^2 fm^{2\lambda-2}$ and E in MeV.

Transitions Strengths (s^{-1})	
$T(E1) = 1.59 \times 10^{15} B(E1) E^3$	$T(M1) = 1.76 \times 10^{13} B(M1) E^3$
$T(E2) = 1.22 \times 10^{9} B(E2) E^5$	$T(M2) = 1.35 \times 10^{7} B(M2) E^5$
$T(E3) = 5.67 \times 10^{2} B(E3) E^7$	$T(M3) = 6.28 \times 10^{0} B(M3) E^7$
$T(E4) = 1.69 \times 10^{-4} B(E4) E^9$	$T(M4) = 1.87 \times 10^{-6} B(M4) E^9$

transitions of higher multipolarity competing with magnetic transitions of a lower multipolarity (resulting in mixing) is reflected by the transition strengths shown in Table 1.1. The transition strengths $T(\sigma\lambda)$ express the γ-ray emission probability per unit time and can be related to nuclear matrix elements (see Eq. 1.68). Transition rates are sensitive to changes in nuclear structure. For example, $T(E2)$ is dependent on the reduced transition probability B(E2), which is sensitive to the electric charge distribution (or quadrupole moment Q_0). The B(E2) within the rotational model is defined as

$$B(E2) = \frac{5}{16\pi} e^2 {Q_0}^2 |\langle I_i K_i 20 | I_f K_f \rangle|^2. \tag{1.74}$$

Conversely, the reduced transition ratio $B(M1)$ is sensitive to single-particle structure and within the collective model is defined as,

$$B(M1) = \frac{3}{4\pi} (g_K - g_R)^2 K^2 |\langle I_i K_i 10 | I_f K_f \rangle|^2, \tag{1.75}$$

where $(g_K - g_R)$ is the difference between the single-particle and collective g-factors and the term in the angled brackets is a Clebsch-Gordan coupling coefficient. Often it is more appropriate to consider the single-particle nature of the nucleus. Using the Weisskopf estimates for the reduced transition probabilities

Table 1.2: Weisskopf estimates for single particle transition rates. $\lambda(\sigma L)$ values are in s^{-1} and E is in MeV.

Weisskopf Transitions Strengths (s^{-1})	
$\lambda(E1)_W = 1.0 \times 10^{14} A^{\frac{2}{3}} E^3$	$\lambda(M1)_W = 5.6 \times 10^{13} E^3$
$\lambda(E2)_W = 7.3 \times 10^{7} A^{\frac{4}{3}} E^5$	$\lambda(M2)_W = 3.5 \times 10^{7} A^{\frac{2}{3}} E^5$
$\lambda(E3)_W = 3.4 \times 10^{1} A^{2} E^7$	$\lambda(M3)_W = 1.6 \times 10^{1} A^{\frac{4}{3}} E^7$
$\lambda(E4)_W = 1.1 \times 10^{-5} A^{\frac{8}{3}} E^9$	$\lambda(M4)_W = 4.5 \times 10^{-6} A^{2} E^9$

results in the single-particle transition strengths shown in Table 1.2. These theoretical calculations can sometimes provide a method for discriminating between γ rays of different multipolarities. e.g. γ-ray decays with high multipolarity depopulating long-lived isomeric states. The transition strength $T(E2)$ can be deduced from lifetime measurements and are related to the charge distribution using the expression,

$$\lambda(E2) = \frac{1}{\tau} = 7.3 \times 10^{7} E_\gamma^5 e^2 {Q_0}^2 |\langle I_i K_i 20 | I_f K_f \rangle|^2. \tag{1.76}$$

1.8.3 Internal Conversion

Decay from an excited state can also occur via internal conversion. The internal conversion process occurs via an interaction of the nucleus and atomic electrons which subsequently causes an atomic electron to be emitted from the atom. The detected energy is discrete but lower in energy than the γ decay due to the electron binding energy (B_e),

$$E_{ce} = E_{trans} - B_e \tag{1.77}$$

where E_{trans} and E_{ce} are the transition energy and the conversion electron kinetic energy upon emitting. Inclusion of the conversion electron process increases the

decay rate from the excited state that one would expect from γ emission alone as,

$$\lambda_t = \lambda_\gamma + \lambda_e. \tag{1.78}$$

Where λ_t is the decay probability of the state and λ_γ and λ_e are the decay probabilities due to γ decay and electron conversion. The degree of electron conversion is measured respective to the γ decay via the conversion coefficient α where,

$$\alpha = \frac{\lambda_e}{\lambda\gamma}. \tag{1.79}$$

Conversion coefficients are higher for magnetic than electric transitions, increase with multipolarity and the Z of the nucleus. The ratio of the conversion electron and γ-ray intensities gives direct experimental access to the conversion coefficient. The multipolarity of a transition can be established by comparing the experimentally deduced value to theoretical values. Thus if the parity of one state is known determining α will reveal the parity of the unknown state.

Chapter 2

Experimental Methodology

This thesis is concerned with the structure of the neutron-deficient tungsten and tantalum isotopes, which exist in close proximity to the N=82 shell closure and the proton drip line. This chapter concerns the reaction mechanisms used for the synthesis of these exotic nuclei and the apparatus used for the detection of radiation emitted from the excited residual nucleus. The techniques for sorting and analysing the experimental data are also discussed.

2.1 Heavy-Ion Fusion Evaporation Reactions

The lightest stable isotopes of Ta and W have 107 and 106 neutrons, respectively. The A = 163 Ta and W isobars investigated in this thesis have 17 fewer neutrons than their respective lightest stable isotope. The most efficient method for synthesizing very neutron-deficient isotopes is via the fusion of two lighter stable nuclear species [New69]. Fusion evaporation is the process where a beam of isotopically pure nuclei are accelerated and collided with a nuclear target. The beam is accelerated so that it has enough energy to overcome the Coulomb barrier

of the nuclei $E_{Coloumb}$,

$$E_{Coloumb} = \frac{e^2}{4\pi\epsilon_0}\frac{Z_t Z_p}{r_t + r_p}, \tag{2.1}$$

where e is the charge of the electron, Z_t and Z_p are the atomic numbers of the target and projectile, respectively and r_t and r_p are the radii of the target and projectile, respectively. The combination of beam and target is chosen such that the nuclei of interest can be populated strongly and cleanly via the reaction. The fusion-evaporation process can be separated into discrete stages and is described in the context of the reaction used for the experimental results reported in this thesis.

1. Preformation. The ^{60}Ni beam is accelerated to an energy that is of sufficient energy to allow the beam to penetrate the Coulomb barrier presented to it by the ^{106}Cd target. The threshold energy E_{th} in the centre of mass frame for fusion can be calculated using the masses of the atoms,

$$E_{th} = -Q = -931.49(M_t + M_p - M_c)[MeV], \tag{2.2}$$

$$E_{lab} = -Q\frac{M_t}{M_t + M_p}, \tag{2.3}$$

where M_c is the mass of the compound nucleus, M_t is the mass of the target nucleus, M_p is the mass of the projectile nucleus and Q is the energy released in the reaction.

2. Formation of the compound nucleus. At beam energies greater than the Coulomb barrier fusion reactions can take place. Energy and angular momentum are carried into the compound nucleus. The compound nucleus forms 10^{-22} seconds later. The excitation energy E^* can be expressed as,

$$E^* = Q + E_{th} = \frac{M_t}{M_t + M_p}E_p[MeV], \tag{2.4}$$

where E_p is the beam or projectile energy. For reactions where (M_p+M_t >100) the fusion reaction is endothermic.

3. Particle Emission. Within 10^{-19} seconds the compound nucleus emits nucleons which carry away at least their binding energy (8-10 MeV). Following particle emission, evaporation residues are generally left in an excited state.

4. Statistical γ-ray emission. As the excitation energy falls below the particle emission energy threshold, the de-excitation process continues via the emission of statistical dipole γ rays. This process occurs around 10^{-15} seconds after formation. Like particle evaporation, the statistical γ-ray emission removes energy but not much angular momentum.

5. Gamma-ray emission along the yrast line. The evaporation residue now exists in a state of high angular momentum. The nucleus loses angular momentum in discrete cascades along the yrast line. The yrast line denotes the maximum permitted angular momentum for a given excitation energy.

6. Ground state. After de-exciting through the yrast structures the nucleus reaches the ground state. If the nucleus is not stable then radioactive decay can proceed from the ground state.

2.2 Gamma-ray spectroscopy

2.2.1 Germanium detectors

Fusion-evaporation reactions populate nuclei at high angular momentum. The decay of these nuclei to their ground state is usually characterised by the emission of a cascade of γ rays. These γ-ray decay sequences can provide much information about the underlying nuclear structure. High resolution γ-ray spectroscopy is performed using arrays of hyperpure germanium (HPGe) detectors. These detectors operate as large reverse biased p-n junctions. Electrons from the n-type material migrate into the p-type material and holes migrate in the op-

posite direction leaving a depleted region with zero net charge. An electric field gradient exists across the depletion zone as a result of this migration. The depletion region constitutes the active volume in which γ-ray interactions are detected. Gamma-ray interactions in the depleted volume generate electron-hole pairs that are swept towards electrical contacts located at the edges of the detector. This electric current constitutes the 'signal', which is used to extract the γ-ray energy. The depth of the depletion region is given by

$$d = \left[\frac{2\epsilon V}{eN}\right]^{1/2}, \tag{2.5}$$

where ϵ is the relative permittivity, V is the reverse bias voltage, e is the electronic charge and N is the impurity concentration in the material [Knoll]. It can be seen from Eq. 2.5 that the active detection volume can be increased by setting a large reverse bias voltage across the crystal. Germanium can tolerate a depletion depth of 2-3 mm before electrical breakdown occurs. Thus, the only method for increasing the active detection volume for a given reverse bias voltage is to lower the impurity concentration in the material. For hyperpure germanium detectors impurity concentrations of 1 in 10^{12} atoms can be achieved resulting in depletion depths of a few centimetres.

The HPGe detectors used in this experiment are manufactured in a bulletized coaxial configuration. In the coaxial configuration, the detector has a cylindrical geometry and is fabricated so that one electrical contact (p^+ contact) covers outer surface. The other contact is formed by removing a section of material from the core and lining the inner cylindrical cavity with n^+ contact material. The crystal is bulletized i.e. rounded at the edges, to remove low-field regions and improve charge collection. The band gap in germanium is small (0.67eV) and the crystal must be cooled to liquid nitrogen temperatures in order to remove thermal noise.

The average ionisation energy ϵ is approximately 3eV and the number of charge carriers per γ ray is large. For example, a 1MeV γ ray will generate around

300000 electron-hole pairs. Therefore since large numbers of charge carriers are produced for each γ-ray interaction, statistical fluctuations are low compared to other detectors (for example inorganic scintillators such as CsI). This has a positive impact on the overall energy resolution since the signal-to-noise ratio is excellent.

2.2.2 Compton Suppression

Gamma rays that interact with the detector medium by the photoelectric effect deposit their full energy and provide a true measure of the incident γ-ray energy. However, for most γ-ray energies measured in this work ($E_\gamma > 200$ keV) Compton scattering is the dominant interaction process. In Compton scattering, the incident γ ray is scattered by an outer atomic electron according to the relation,

$$E'_\gamma = \frac{E_\gamma}{1 + \frac{E_\gamma}{m_0 c^2} cos\theta}, \tag{2.6}$$

where E'_γ is the energy of the scattered photon, E_γ is the energy of the incident photon, m_0 is the rest mass of the electron and C is the speed of light. Gamma rays that undergo Compton scattering and subsequently escape the detector volume do not deposit their full energy and contribute to an undesirable continuum background. The Compton background can be suppressed by surrounding the HPGe crystal by an inorganic scintillator used in anti-coincidence. Bismuth germanate (BGO) is the most commonly used inorganic scintillator for Compton suppression shields [WM73]. BGO is a desirable material for escape suppression shields due to its fast timing propoerties, large density (7.3 gcm^{-3}) and high efficiency for stopping γ rays (Bi atomic number $Z = 83$). Hence small amounts of material can be used effectively for escape suppression. Also, the scintillation light produced following a γ-ray interaction is transparent to the BGO crystal. Although, the light yield of BGO is lower than some materials, this is offset by these other advantages outlined previously. The use of a Compton suppression

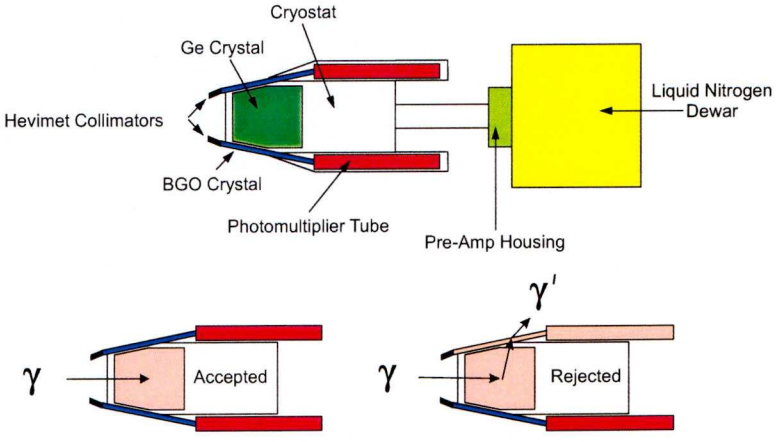

Figure 2.1: A schematic illustration of a EUROGAM phase 1 HPGe escape suppressed spectrometer.

shield in anticoincidence with a HPGe detectors improves the peak-to-total (PT) ratio from an unsuppressed $PT = 0.2$ to a suppressed $PT = 0.6$ around 1300keV for the JUROGAM array [Beau96].

2.2.3 Large γ-ray spectrometer arrays

The total photopeak detection efficiency is a measure of the ability of an array to detect incident γ rays. The efficiency of a single detector or array can be measured by using a known γ-ray source at the focus of the spectrometer. The efficiency has dependence on geometrical constraints such as the total solid angle subtended by the detector. For example, increasing the distance between the source and detector will act to decrease the solid angle thereby lowering the efficiency. Thus, large spectrometer arrays are designed to cover a sizeable fraction of the 4π solid angle.

The resolving power of an array, R, gives an indication of the spectrum quality and is defined as

$$R = \frac{SE_\gamma}{\Delta E} PT, \tag{2.7}$$

where ΔE is the resolution of γ rays in the spectrum, SE_γ is the average separation of γ rays in a cascade and PT is the peak-to-total ratio [NBF94]. Since SE_γ is dependent on the structure of the nucleus, the resolving power can only be improved by improving the detector resolution (lowering ΔE) or increasing the peak-to-total ratio. The intrinsic resolution of a HPGe detector is ~ 2 keV at 1.332 MeV, but it is much worse for in-beam experiments. In reality the following factors affect the resolution.

- The intrinsic detector resolution, ΔE_{Int}.
- Doppler broadening due to the opening angle of the detectors, ΔE_{Open}.
- Doppler broadening due to the angular spread of recoiling nuclei, ΔE_{Rec}.
- Doppler broadening due to the velocity (energy) spread of recoiling nuclei, ΔE_{Vel}.

Thus, the final resolution is a combination of these factors such that,

$$\Delta E^2 = \Delta E_{Int}^2 + \Delta E_{Open}^2 + \Delta E_{Rec}^2 + \Delta E_{Vel}^2. \tag{2.8}$$

In principle, the detector resolution can be improved by increasing the granularity of the detectors (lowering opening angle of detectors) or by performing kinematic corrections facilitated by using a suitable ancillary detector.

The array resolution can be improved by applying a correction for the Doppler effect. The Doppler effect arises as the recoiling nucleus is moving with respect to the Ge detectors. The recoiling nucleus emits electromagnetic radiation (γ rays), the γ-ray energy observed has an angular dependance. The Doppler-shift can be removed in the sorting algorithm by compensating for the recoil velocity. In the present experiment, a recoil velocity of 3.17% of the speed of light was deduced by using the known γ-ray energies and detector angles with respect to the beam

axis according to

$$E_\gamma = E_0 \left(1 + \frac{v}{c} cos\theta\right). \tag{2.9}$$

It is difficult to improve the peak-to-total ratio for a Compton suppressed detector. However some improvement in observation sensitivity can be achieved by collecting high-fold coincidences[1]. This is indicated by the relation,

$$\left[\frac{N_p}{N_b}\right]_F = \alpha_0 (0.76R)^F, \tag{2.10}$$

where $\left[\frac{N_p}{N_b}\right]_F$ is the peak-to-total ratio when a fold criterion has been applied to the data and α_0 is the observational limit of the array [NBF94]. Further improvements can be made if the background is suppressed by using an ancillary device such as a recoil separator. Thus, Eq. 2.10 is modified to include an enhancement factor R_0,

$$\left[\frac{N_p}{N_b}\right]_F = \alpha_0 (0.76R)^F R_0. \tag{2.11}$$

2.2.4 The JUROGAM γ-ray spectrometer

The JUROGAM spectrometer comprises 43 Compton suppressed coaxial detectors. The array is a composite device comprising EUROGAM and GASP detectors. The hyperpure germanium crystals are n-type material and have a diameter of $\sim$ 70 mm and length $\sim$ 75mm. The total geometric coverage is $\sim$ 23% yielding a photopeak efficiency of 4.2% for 1.332 MeV γ rays. The JUROGAM spectrometer array is almost identical to the EUROGAM I spectrometer and so has similar resolving power (R=5.6), limit of observation ($\alpha_0 = 5 \times 10^{-4}$) and optimal fold ($n = 3$). The JUROGAM spectrometer has 5 detectors at 158°, 10 at 134°, 10 at 107°, 5 at 94°, 5 at 86° and 8 at 72°. The JUROGAM spectrometer is ideal for measuring high-fold coincidences.

[1]Cascades of γ rays can have high multiplicities M_γ. The M_γ represents the total number of γ rays emitted at the target position. The fold, F, is the number of γ rays detected simultaneously.

2.2.5 High-fold coincidence analysis

A major aim of using γ-ray spectroscopy to unravel the underlying nuclear structure is to establish a detailed excitation level scheme for the nucleus of interest. The benefits of using high-fold coincidences to improve the limit of observation was outlined in Section 2.2.3. The increased photopeak efficiency for γ-ray detection brought about by the advent of large spectrometer arrays has increased the probability of measuring high-fold coincidence events. Although, the number of high-fold events $n > 3$ is relatively small, unpacking high-fold events into lower fold coincidences can make a significant contribution to the number of low-fold events. An n-fold event can be unpacked into m-fold subevents according to the relation,

$$ {}^{n}C_{m} = \frac{n!}{m!(n-m)!}. \tag{2.12} $$

For example, the unpacking of a single five-fold event generates ten fold three events. The unpacking of folds of $\geq$5 must be handled carefully [Beau95]. If the unpacking of data is handled incorrectly spikes can be introduced into multiple-gated spectra. The most convenient method for visualising high-fold data is to use a multidimensional spectrum. For example, if all high-fold coincidences are unpacked into two-fold events the data can be represented in a two-dimensional spectrum or matrix. Each two-fold event $(E_{\gamma A} - E_{\gamma B})$ is incremented in the matrix with the symmetric pair $(E_{\gamma B} - E_{\gamma A})$, see Fig. 2.2(a). This ensures that the matrix is symmetric about the main diagonal with each energy defined on x and y axes. The total projection of the matrix is shown in Fig. 2.2(a) and corresponds to a spectrum containing one count at energies A and B.

Coincidence spectra can be obtained by selecting a narrow range of energies (or gate) on one axis and projecting the number of counts on the remaining axis. Figure 2.2(b) shows the resulting one-dimensional spectrum formed by gating on γ ray A. The resulting coincidence spectrum shows that γ ray B is in coincidence

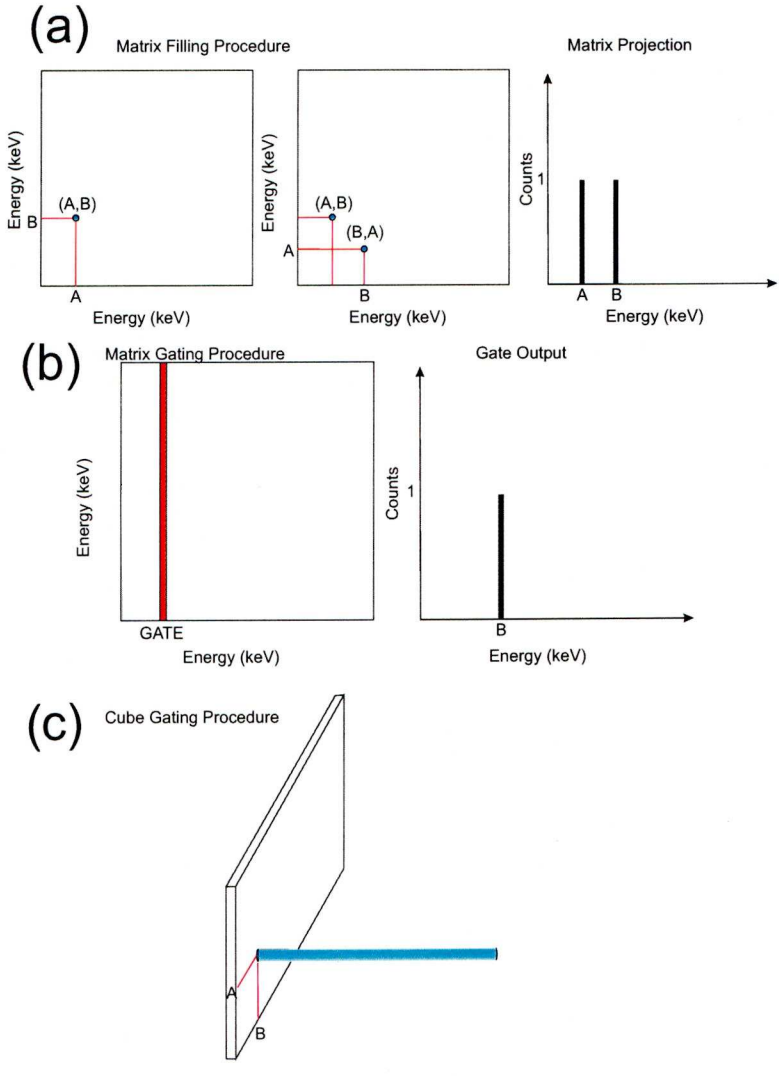

Figure 2.2: An illustration of (a)the matrix filling procedure (b)the matrix gating procedure and (c)the cube gating procedure.

with γ ray A. Similarly summed coincidences can be formed by adding gates.

High-fold events can be unpacked into the three-fold (triple) coincidences and stored in a three-dimensional array or cube. One-dimensional spectra are produced by demanding coincidences with gates on two of the cube axes and projecting the number of counts on the remaining axis. Figure 2.2(c) shows how a γ-ray spectrum in coincidence with A and B is generated from a cube. Cubes are useful for placing self-coincident γ-ray doublets in a level scheme. Self co-

incidence occurs when there are two or γ rays in a level scheme whose energy difference cannot be resolved by the spectrometer. Such placements cannot be resolved with a two dimensional matrix.

2.2.6 Angular Correlations

Angular correlations have been deduced where possible for experimentally deduced transitions. The analysis involves the detection of two gamma rays emitted sequentially in the same cascade [KSW72]. The measurements were carried out on recoil-tagged data due to the significantly enhanced statistics. Contamination from competing channels made such a measurement impossible without the use of fold-three data. In the analysis fold-three events were sorted for the purpose of directional correlations of γ radiation emitted from oriented states (DCO). Strictly speaking the orientation axis is defined by the initial transition detected in the cascade and the function is dependent on the angle between the gamma rays $\Delta\phi$. This measurement was taken over all $\Delta\phi$ and therefore the dependency was neglected. An experimental DCO is given by,

$$R_{DCO} = \frac{I^{\gamma 2}_{\theta_1}(Gate^{\gamma 1}_{\theta_2})}{I^{\gamma 2}_{\theta_2}(Gate^{\gamma 1}_{\theta_1})} \tag{2.13}$$

2.3 Recoil Decay Tagging

The spectroscopic study of heavy neuton-deficient nuclei approaching the proton drip line is challenging from an experimental perspective. The production cross sections for neutron-deficient nuclei diminish rapidly with the removal of neutrons near the proton drip line. Fusion evaporation reactions producing a compound nucleus in the $A \sim 165$ region lead to many open reaction channels, including fission, with different production cross sections. It is likely that γ rays from the nucleus of interest will obscured by a huge background arising from other reaction

channels. However, the heavy neutron-deficient ($Z > 50$) nuclei occupy a region of the nuclear chart where nuclei can decay by α or proton radioactivity. These decay modes have distinct decay energies and can be used as a selective 'tag' on γ rays emitted by specific nuclides. This is the essence of the recoil-decay tagging (RDT) technique that was developed at GSI by Simon *et al.* [Sim86] and exploited with large γ-ray spectrometers at the Daresbury Laboratory by Paul *et al.* [Paul95]. Recoil-decay tagging experiments use a large γ-ray spectrometer array in conjunction with a recoil separator and focal plane detection system.

In an RDT experiment, a fusion evaporation reaction produces several residual exotic nuclei in an excited state. These nuclei decay as outlined in section 2.1 and the prompt yrast decays are detected within the γ-ray spectrometer located at the target position. The fusion evaporation residues exit the target in a forward-focused cone in to a recoil separator. In the separator, the fusion products are electromagnetically separated from the unreacted beam, fission fragments and each other and implanted into a position sensitive silicon detector at the focal plane of the separator. The time, energy and position of each event are recorded using an appropriate data acquisition system. At some time after implantation, the exotic nuclei decay in the same region of the implantation detector and the time and energy are recorded. Using the time stamped information allows temporal correlations to be made between the implanted nucleus and its subsequent radioactive decay. Since the nuclear implants are recorded in coincidence with the γ rays detected promptly at the target position (allowing for the flight time through the separator), an unambiguous identification of excited states in a specific nuclide can be made. Similar correlations can be made by using γ rays depopulating isomeric states at the focal plane as a selective tag on γ rays detected at the target position. The apparatus used in this experiment is outlined in the following subsections.

2.3.1 Gas-filled recoil separators

Recoiling fusion evaporation residues have a broad distribution of charge states due to scattering in the target. A vacuum mode separator would usually be optimised for a particular charge state. This leads to poor transmission efficiency as other states in the charge state distribution are lost. This can be overcome by using a gas-filled separator.

In a gas-filled separator, the electronic charge state of a heavy ion fluctuates due to charge exchange collisions as it passes through a dilute gas. If the number of collisions is sufficient the trajectory of the ion through a magnetic field can be expressed in terms of an average charge state q_{av}. The multiple collisions focus the charge distribution about q_{av}. This has the benefit of increasing the transmission efficiency at the separation stage albeit at the expense of mass resolution [Gh88, Coh58]. For example, a gas-filled separator like RITU can have a transmission efficiencies in the range 20-50% compared to vacuum-mode separators such as the fragment mass analyser (FMA), which typically has $< 10\%$ transmission efficiency.

The fusion products that emerge from the target are separated from the scattered beam due to the difference in their respective magnetic rigidities. The magnetic rigidity, $B\rho$, of ions with momentum p traversing a magnetic dipole field with flux density B can be written as

$$B\rho = \frac{p}{q_{av}}. \tag{2.14}$$

The magnetic rigidity is determined by the average charge state q_{av}. This can be approximated by making a simple assumption as proposed by Bohr [Bo40]. The assumption states that all orbital electrons whose velocities are less than the ions velocity are stripped. Using the Thomas-Fermi model of the atom the average

charge state of the ion is

$$q_{av} = \left(\frac{v}{v_0}\right) eZ^{1/3}, \tag{2.15}$$

which is valid in the region $1 < v/v_0 < Z^{2/3}$ where $v_0 = 2.19 \times 10^6$ m/s, v is the ion velocity. In heavy-ion fusion evaporation reactions the ratio v/v_0has values in the range 1-4. The magnetic rigidity can now be written

$$B\rho = 0.0277\frac{A}{Z^{1/3}}\text{Tm}, \tag{2.16}$$

where Z and A are the atomic and mass numbers of the recoiling ion, respectively. This shows that the magnetic rigidity is independent of the original charge state of the recoiling ions. Equation 2.16 shows indicates that mass separation of the primary beam and fusion products can be achieved most efficiently where the masses, and the magnetic rigidities, are significantly different i.e. light projectile and heavy fusion product.

2.3.2 The RITU gas-filled separator

The RITU gas-filled separator [Le03] was designed for the study of heavy elements and proton-rich nuclei and is located at the University of Jyväskylä Accelerator Laboratory. The separator is filled with He gas that is circulated so that the whole chamber gas volume is refreshed every 30 minutes. The gas pressure is $\sim$ 1 mbar but can be varied in order to achieve an optimal image size at the focal plane. The gas volume is separated from the high-vacuum beam line by a differential pumping system. This system replaces the thin carbon or nickel foil windows used in earlier systems, thereby removing a source of γ-ray background at the target position.

The separator comprises dipole (D) and quadrupole (Q) magnets arranged in a $QDQQ$ configuration. The first magnet is a vertically focusing quadrupole that is used to match the forward-focused recoil cone to the angular acceptance

of the dipole magnet. This lowers transmission losses associated with coupling RITU to the JUROGAM spectrometer. This configuration has the added benefit of providing a natural fission veto since few fission fragments are accepted into the separator.

The primary scattered beam is separated from the fusion reaction products by the dipole magnet according to their magnetic rigidities. The unreacted beam is suppressed in the dipole magnet and dumped into a tantalum ski located in the dipole chamber. As the magnetic rigidity varies linearly with mass, separation is aided by large mass differences between the beam and recoiling nuclei. The optimum beam suppression is achieved in asymmetric reactions performed using a light beam with a heavy target.

The remaining quadrupole magnets provide horizontal and vertical focusing of the fusion products and can be used to optimise the coverage of the recoil distribution on the focal plane implantation detector.

2.4 The GREAT Spectrometer

The GREAT spectrometer [Page03] was designed to measure the decay properties of fusion evaporation residues transported to the focal plane of a recoil separator. The spectrometer comprises highly segmented silicon and germanium detectors used in conjunction with a multiwire proportional counter. The GREAT spectrometer was designed and built in the UK and has been deployed at the RITU focal plane since 2003. Although, GREAT can be used as a stand-alone device for radioactive decay measurements, it is used in this work as a tagging spectrometer correlating γ rays detected at the target position in JUROGAM with decays measured at the RITU focal plane. The total data readout (TDR) data acquisition system [Laz01] has also been developed as part of the GREAT project to eliminate the problem of common dead time that is encountered in conventional

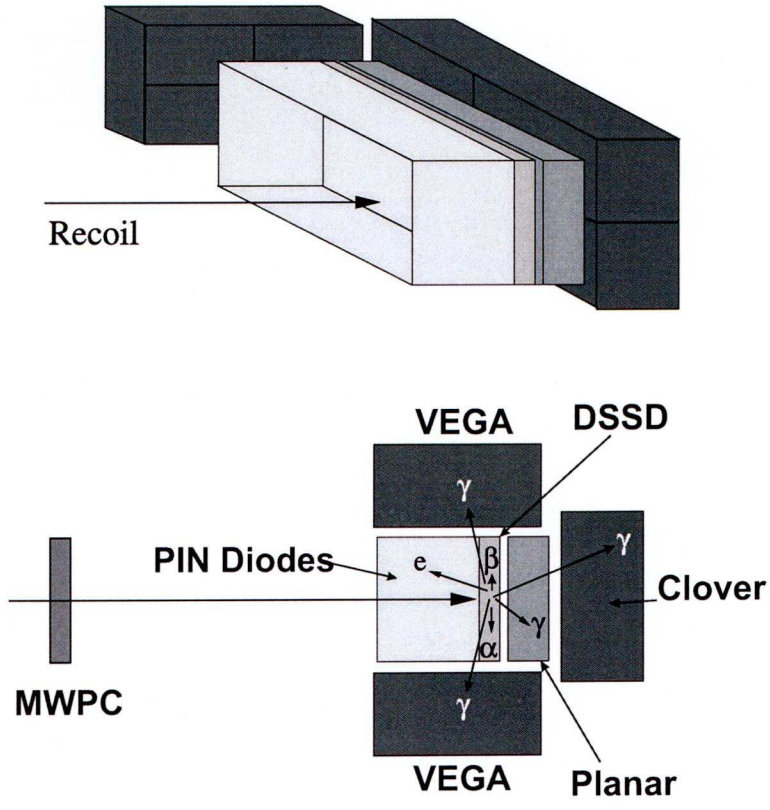

Figure 2.3: A schematic illustration of the GREAT spectrometer. In the current work two additional VEGA clover Ge detectors were used in conjunction with the GREAT spectrometer

data acquisition systems. A schematic of the GREAT spectrometer is shown in Fig. 2.3. The GREAT spectrometer comprises a transmission multi-wire proportional counter (MWPC), silicon PIN-diode detectors, Double-sided-Silicon-Strip Detector (DSSD). A planar germaniun detector is located immediately behind the DSSD and a clover detector can either sit vertically above or to the sides of the DSSD or behind the planar detector.

Multiwire proportional counter (MWPC)

The transmission multi-wire proportional counter (MWPC) is used to measure separated reaction products and scattered beam as they exit the RITU separator.

The isobutane gas volume is contained by Mylar foil windows that provide separation from the He filling gas of RITU and the vacuum in which other GREAT detectors are operated. The MWPC has an aperture of 131 mm $\times$50 mm giving an angular acceptance that is greater than that of the implantation detector (DSSD). The MWPC can therefore detect separated beam that lie outside the acceptance of the DSSD. This leads to higher count rates being measured in the MWPC relative to the DSSD. The MWPC can be used to distinguish recoiling fusion products from scattered beam through energy loss and, in conjunction with the implantation detector, time-of-flight measurements, see Section 2.6.4. The timing information is extracted by comparison with a fast signal from a central contact in both the horizontal and vertical wire planes. Similarly, the absence of a signal within the MWPC in coincidence with the triggering event in the DSSD indicates a radioactive decay.

The DSSD implantation detectors

The GREAT implantation detector comprises a pair of highly segmented double-sided silicon strip detectors (DSSDs). The DSSDs are used to measure the energies of implanted ions and any subsequent radioactive decays. Each detector has an active area of 60mm$\times$40 mm and a thickness of 300 μm. The strip pitch is 1 mm in both directions segmenting the active area of the two silicon detectors into a combined total of 4800 independent pixels. This granularity allows higher implantation rates without compromising decay correlations. The DSSDs are mounted side by side on a hollow block through which coolant is circulated, to reduce their temperature to -20°C. It is estimated that up to 85% of the recoil distribution can be collected by the DSSDs.

The PIN diode detectors

An array of 28 silicon PIN diodes is located in a box arrangement perpendicular to the outer edges of the DSSD. The PIN diodes can be used to detect conversion electrons or escaping α particles. The PIN diode gain range has to be selected before the experiment for successful detection of the energy region of interest i.e. electrons or escaping α-particles. Each PIN diode has an active area of 28 mm$\times$28 mm and a thickness of 500 μm. The PIN diodes are mounted in pairs on a motherboard. The 14 motherboards are mounted around the inside surface of the cooling block forming two rows of detectors perpendicular to the perimeter of the DSSDs.

The implantation depth of recoils in the DSSD ($1 - 10\mu$m) is not sufficiently deep to prevent conversion electrons escaping in the upstream direction. Coincidences between conversion electrons detected in the PIN diodes and the γ rays detected in the GREAT germanium detectors can be determined from the detector timestamp information.

The planar Ge detector

The planar detector is used primarily for the detection of low-energy γ rays and X rays. The rectangular crystal has an active area of 120 mm$\times$60 mm and a thickness of 15 mm. The strip pitch on both faces is 5 mm providing 288 pixels. The detector is housed in its own cryostat and mounted directly behind the DSSDs ($\sim$10 mm downstream). A thin Be window (0.5 mm thick) is mounted inside the vacuum chamber and allows the penetration of low-energy γ rays and X rays. The efficiency of the detector has a maximium value of around 15% at 100 keV but decreases sharply to a few % above 350 keV [An04]. The close proximity of the planar and DSSD allows for a large angular coverage. The planar Ge detector can also be used to detect high-energy β particles ($\geq$ 2 MeV) that penetrate

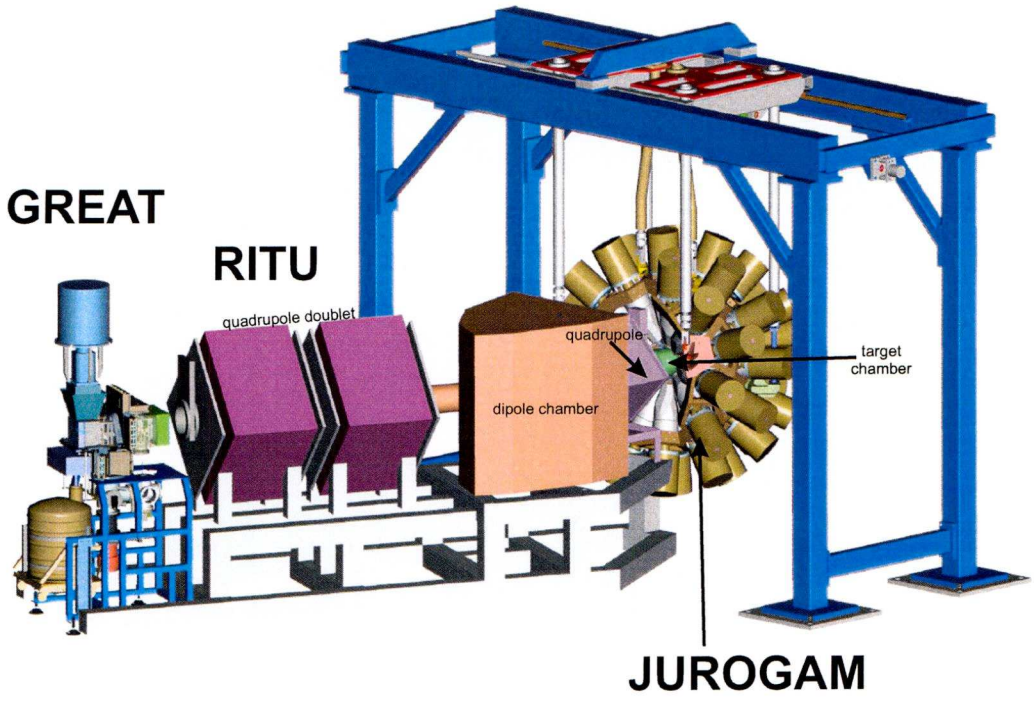

Figure 2.4: A schematic diagram of the JUROGAM, RITU and GREAT apparatus. The two VEGA Clover detectors that were used in conjunction with the GREAT clover are not illustrated.

through the DSSD. The experimental planar energy resolution was measured to be ±1.5keV at 100keV and ±2.5keV at 450keV.

The clover Ge detectors

The GREAT clover detector is a segmented Compton-suppressed HPGe detector used to measure γ ray energies in the 100 - 2500 keV range. The detector consists of four externally tapered crystals, each crystal has four-fold electrical segmentation. Each crystal has a diameter of 70 mm before shaping and is 105 mm long. The first 30 mm of their length is tapered at an angle of 15° on the outside surfaces. The clover is mounted outside the vacuum chamber and positioned vertically above the DSSD to achieve maximum efficiency by covering the maximum

possible solid angle. The total photopeak efficiency at the focal plane is augmented by the inclusion of two VEGA clover Ge detectors. GEANT simulations performed by Andreyev *et al.* indicate that this clover arrangement has an efficiency of $\sim 8\%$ at 100 keV and $\sim 5\%$ at 1 MeV [An04]. A schematic illustration of the apparatus is shown Fig. 2.4. The experimental clover energy resolution was measured to be $\pm$3keV at 100keV and 450keV.

2.5 Total Data Readout

Total Data Readout (TDR) [Laz01] is a novel data acquisition concept. Conventional data acquisition systems rely upon a common master trigger (e.g. a signal recorded in the implantation detector). Under these conditions signals from all other detectors are delayed and read out as part of the same event. This presents a problem for RDT experiments.

In a typical RDT experiment, the trigger is provided by a pre-designated focal plane detector. This method relies upon delaying the signals detected at the target position so that they can be measured in coincidence with the focal plane trigger. The signals are delayed to account for the times of flight of recoiling nuclei. The recoiling nuclei may also have some isomeric states that can be detected post-separation at the focal plane. The trigger width must be sufficiently wide for the detection of such isomeric states. Typically widths of 5 μs are used. A conventional data acquisition system has the significant disadvantage of introducing a 'blind period' where the focal plane detectors are not responding to prompt radioactive decays inside the trigger width. Another problem stems from the loss of signals outside the master trigger. The TDR concept has been developed for GREAT in order to overcome this limitation and eliminate common dead time.

In TDR, the energy and timing signals from shaping amplifiers and constant

fraction discriminators (CFDs) are sent to the inputs of VXI cards having 32 independent 14-bit ADC channels. A gate is generated individually for each detector, either by the associated external CFD or by a software controlled trigger. Each ADC conversion is timestamped within the ADC card and passed on to the event collator, which then assembles the fragments using spatial and temporal correlations required by the experiment. The Metronome is a VME module that synchronizes each ADC timestamp to a 100 MHz clock. The data is subsequently merged into a time ordered stream and routed into the event builder, see Fig. 2.5. The event builder will pre-filter the data according to any preset software trigger condition. A schematic diagram of the TDR data acquisition system is shown in Fig. 2.5.

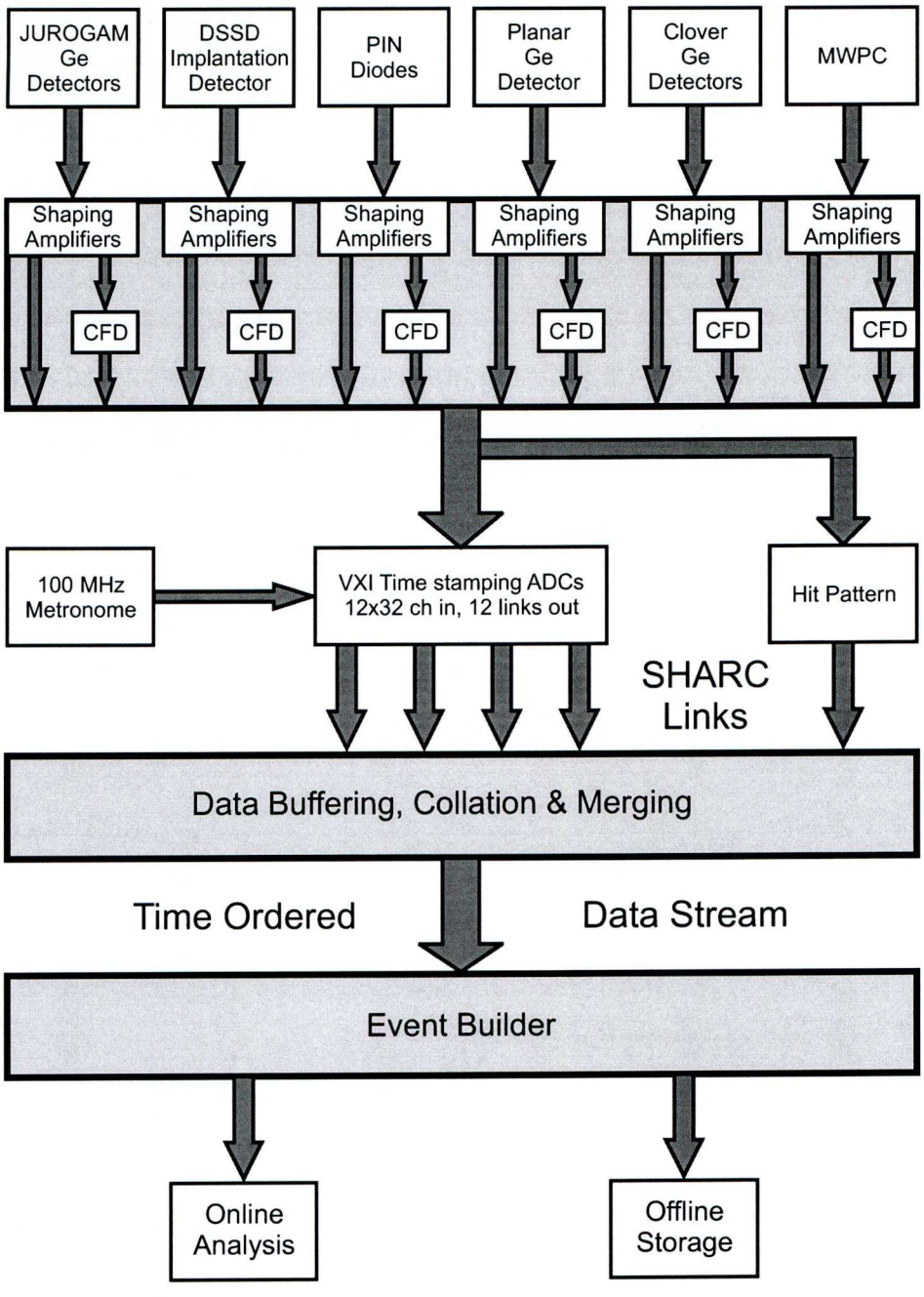

Figure 2.5: A schematic diagram of the TDR triggerless data acquisition system.

2.6 Data Sorting

2.6.1 Introduction to GRAIN

The novel TDR readout implemented at JYFL required a novel software package for online/offline data sorting. The software package invented for this purpose is called GRAIN [Rah08]. The GRAIN package is a Java based cross-platform framework to analyse the raw TDR data stream, sort time-stamped data and perform the RDT analysis.

2.6.2 GRAIN event parser

In TDR acquisition system each detector collects and reads out information asynchronously in singles mode independently of a hardware trigger [Laz01]. The temporally ordered data stream that emerges from the event builder is subsequently parsed by the GRAIN software. Thus functional components are selected from the data stream and grouped together. For example all channels corresponding to the JUROGAM array will be brought together as a class. Other parsing of the data is required. Unlike conventional data acquisition systems, GRAIN filters pile-up events in the TDR data stream and performs the Compton suppression of the JUROGAM array. The grouping of these events is carried out using the spatial and temporal correlations of channels originating from the same detector.

2.6.3 Software Trigger

The GRAIN interface utilises the flexibility of the TDR triggerless data acquisition system. A major advantage of GRAIN over conventional systems is that it can generate a software trigger. Thus the trigger conditions and the trigger width can be varied from one sorting procedure to another using the same data set. For example, one can trigger on signals in either the DSSD or the GREAT

germanium detectors in different sorts on the same data to perform and RDT or isomer-decay tagging correlation. The software trigger is flexible enough to allow conditions to be set on any detector or group of detectors.

In the experiment reported in this thesis the trigger condition was set to read out all signals within a set width and delay of an X-face DSSD signal. The delay is used to collect spectroscopic information from the JUROGAM array as well as any other detectors which trigger prior to the recoil implant in the DSSD. The width of the DSSD-event window will be adjusted to allow the study of any isomeric states within the recoiling nucleus.

In conventional systems increasing the width of the trigger would lead to increased common system dead time yet longer gate widths are desirable for the study of long-lived isomers. Only events that occur within the specified width of the software trigger are included in the sort algorithm, unless they originate from the trigger detector itself. If correlations over larger time-scales are attempted there is an increased probability of retrieving signals belonging to different DSSD events. Therefore any correlations occurring outside the trigger width and with no associated prompt trigger signal in the DSSD must be ignored.

2.6.4 Event Identification

The determination of the character of DSSD events is a crucial part of the sorting algorithms. There are two types of events that are of interest, namely implanted fusion evaporation residues (hereafter called recoils) and their subsequent radioactive decays. Temporal correlations between events in the DSSD and the MWPC are used to distinguish recoil events implanting into the DSSD and their radioactive decays. Recoils can be distinguished from scattered beam by generating an energy loss versus time-of-flight matrix. Energy loss signals in the MWPC are correlated with the appropriate recoil implantation by selecting events pass-

ing a gate on an MWPC-DSSD time-to-amplitude conversion (TAC) condition generated from the relevent timestamps. Similarly time-of-flight information is obtained from the specific time differences between events satifying this condition. The time-of-flight through the separator will be faster for the energetic scattered beam nuclei. The recoiling reaction products are are transmitted at lower velocities and are usually are much heavier with higher atomic numbers than the beam particles. Thus, the recoils experience a greater degree of stopping in the MWPC gas volume. The appropriate matrix for this experiment is pictured in Fig. 2.6 Two-dimensional gates on the recoil distribution in Fig. 2.6 can be better defined by selecting only those events for which prompt γ rays detected in JUROGAM are observed. Decay particle identification is determined by using the MWPC in anti-coincidence with the DSSD implantation detector i.e. a DSSD event without a recoil time-of-flight constitutes a radioactive decay.

2.6.5 DSSD Tagger

Recoil-tagging can be investigated simply by concentrating on the designated recoil DSSD events. The DSSD tagger must be used for RDT or longer decay chain correlations. The tagger is simply an array with dimensions defining location in two-dimensions (x and y) and time on the third dimension (t), see Fig. 2.7 for a pictorial representation. When a recoil or decay event is identified in the sorting algorithm it is placed into the appropriate pixel within the tagger. There is a maximum temporal depth, which is set by the user. The sort algorithm searches through the tagger upon the insertion of each new event. In this experiment the implantation rate was relatively high and searches through the tagger were confined to the same pixel as the latest decay event being processed. The pre-determined correlation conditions were applied to the tagger events by the sort algorithm. If the algorithm identified the previous tagger event as a

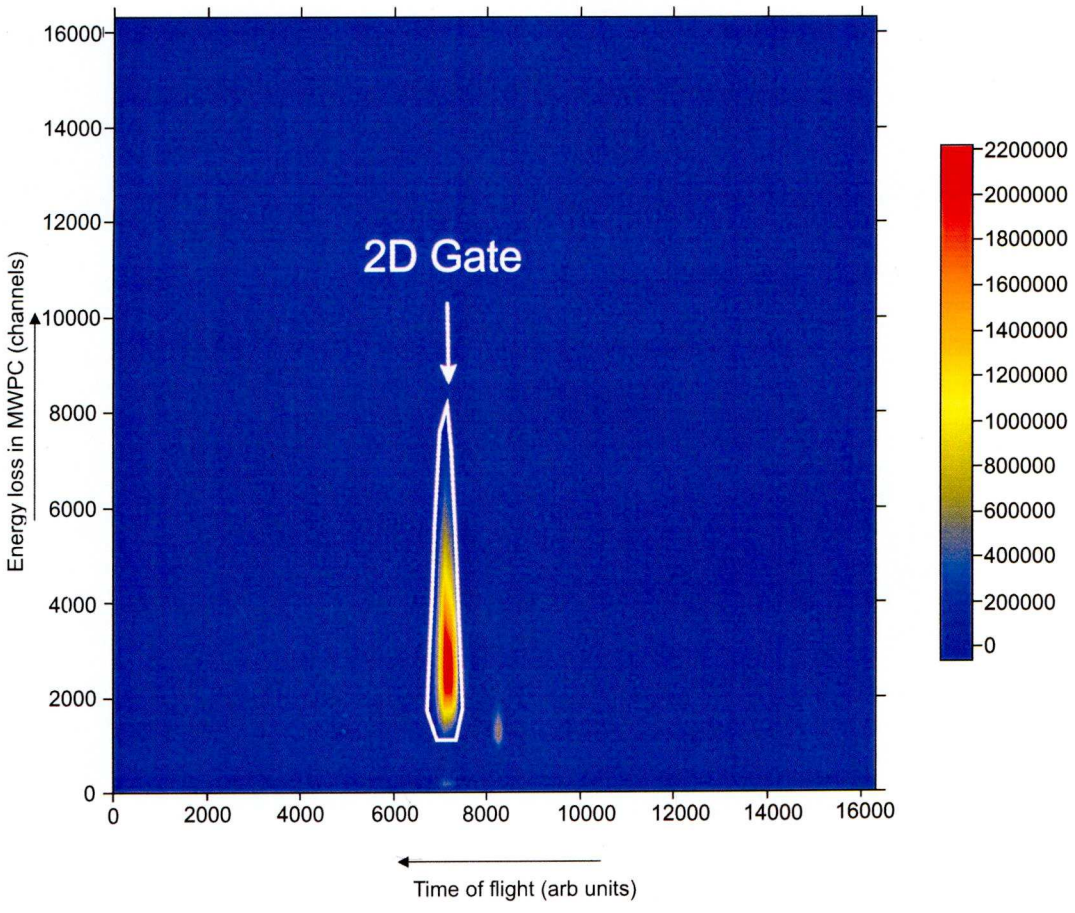

Figure 2.6: Two-dimensional spectrum obtained from the current analysis showing energy loss in the MWPC versus ion time-of-flight. The time-of-flight is determined from time differences between the MWPC and a DSSD implantation detector. The two-dimensional gate used to identify and select recoil implantations is indicated. The matrix also shows a small amount of scattered beam to the right of the recoil distribution. The excellent beam suppression and clear separation between the fusion evaporation residues and the scattered beam is apparent.

recoil, a secondary check on the event which precedes the recoil was initiated. The purpose of this secondary check was to remove contamination resulting from erroneous recoil-decay chain identifications. If the time between the subsequent recoil implantations was less than $5 \times t_{1/2}$ of the tagged radioactive decay then

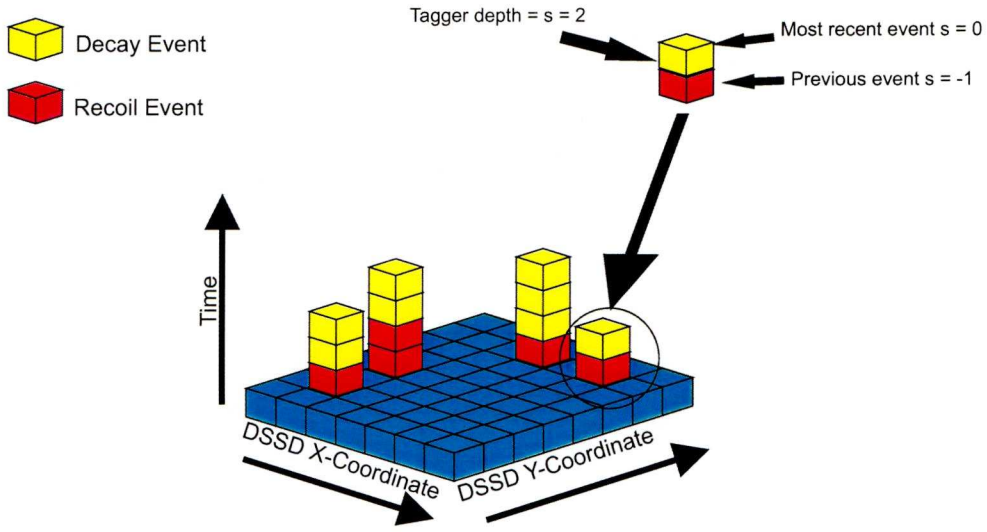

Figure 2.7: Schematic illustration of the GRAIN tagger.

the entire correlation was vetoed. If there was no preceding recoil implantation the γ signals associated with the recoil were then correlated with the radioactive decay. The same check is carried out when demanding correlations involving longer decay chains allowing for the condition that there is an extra decay event observed before the recoil.

2.7 Detector Calibrations

2.7.1 DSSD ans PIN Diode Calibrations

The present data set had a significant number of α decays from several nuclei permitting an internal calibration. An internal calibration using known decays from implanted fusion evaporation products is preferable to a calibration using an external source. Alpha particles emitted externally to the DSSD have to pass through a 'dead' layer on the surface of the detector and deposit less energy rendering the calibration inaccurate. Calibrations utilising external sources do not account for the recoil 'kick' of the α-emitting nucleus. Figure 2.8 shows a

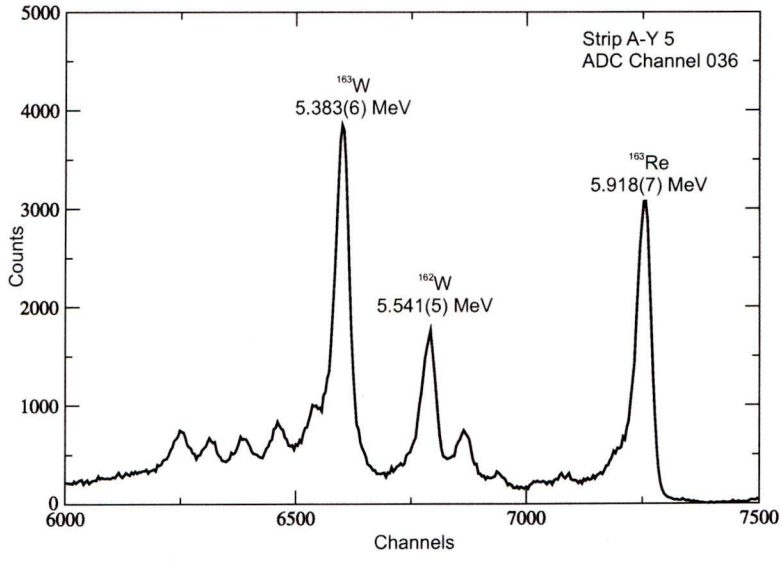

Figure 2.8: Spectrum showing all radioactive decays detected in a single DSSD strip within 600ms of detecting a recoil implantation. The α-decay peaks used in the internal calibration are labelled by their decay energies [Page96].

typical spectrum for a single DSSD strip and indicates the α-decay peaks used in the calibration. The calibration took the form of a linear fit to the ^{163}W and ^{163}Re peaks. The calibration was checked by measuring the energy of the ^{162}W peak and comparing values with the published measurements [Page96]. The resultant energy versus strip matrix for the x-axis strips indicates the quality of the calibration and gainmatching and is shown in Fig. 2.9. The GREAT PIN diode detectors were calibrated using a external ^{133}Ba conversion electron source.

2.7.2 JUROGAM calibrations

The JUROGAM detectors were calibrated individually using a mixed ^{133}Ba and ^{152}Eu source. A gain range up to 1.5 MeV was set for the JUROGAM detectors. The Analogue to Digital Converters are non-linear for channel numbers $\leq$1400. This behaviour was corrected using a damped-sine method used previously in

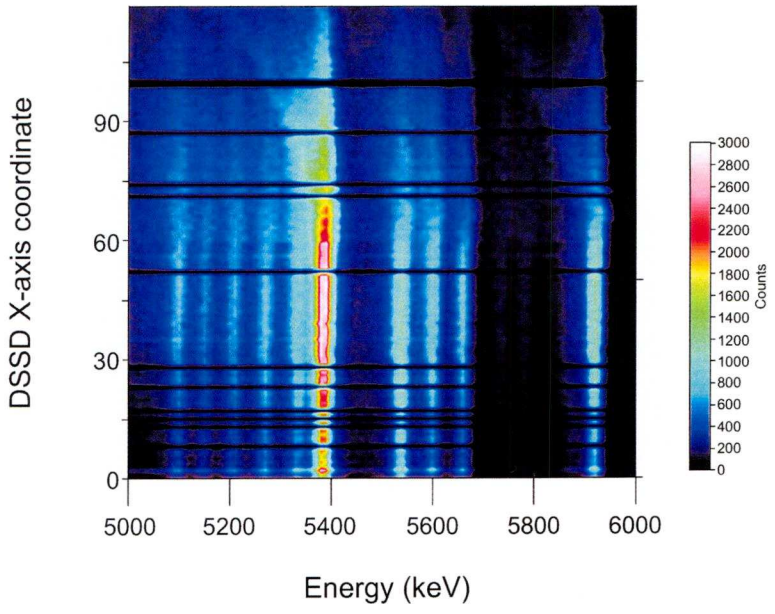

Figure 2.9: Typical decay particle energy spectrum for across the whole DSSD (x-side strips).

analysis of JUROGAM data [Ee06]. A cubic fit to the data for the peaks observed in channels $\geq$2000 is implemented. The difference in energy between the calibrated peaks and those obtained from reference material is then plotted against channel number. A secondary function is fitted that corrects for the non-linearity. Good correspondence between channel number and photon energy was found down to $\approx$80 keV. Each individual JUROGAM detector was analysed for gain shifts throughout the experiment. Specifically detectors numbers 44, 37 and 11 showed significant gain shifts and were subsequently removed from the analysis. An example of the shift seen in time or in this case against file number is shown in Fig. 2.10. The in-beam energy resolution was $\pm$2keV at 200keV and $\pm$3.5keV at 800keV.

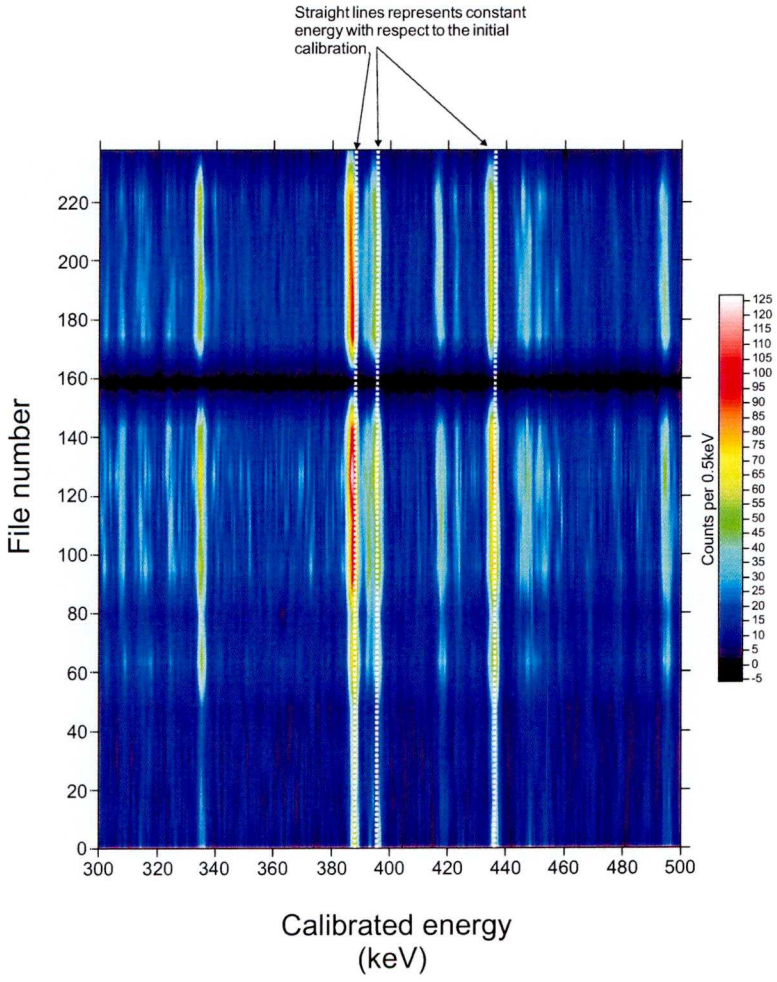

Figure 2.10: A typical matrix used to highlight energy variations due to gain shifts as a function of time (run number). This matrix highlights the gain shift experienced by JUROGAM detector number 11.

2.7.3 Planar, VEGA and Clover Calibrations

The planar, VEGA and clover detectors were calibrated using a mixed ^{152}Eu and ^{133}Ba source. The gain ranges of the VEGA and clover were set up to 1.5 MeV and a non-linear calibration was again applied in the form of a damped-sine correction. The gain range of the planar was set up to 750 keV such that the non-linear correction was not necessary.

Chapter 3

The yrast structure of ^{163}W and neighbouring isotopes

Excited states in the neutron-deficient nuclide ^{163}W were investigated using the ^{106}Cd(^{60}Ni,2pn)^{163}W reaction (E_{beam} = 270 MeV) in an experiment performed at the University of Jyväskylä Accelerator Laboratory. The excitation level scheme for ^{163}W has been extended significantly with the observation of several new bands. Configuration assignments for the new bands have been made on the basis of comparisons of the deduced aligned angular momentum, as a function of rotational frequency, with the predictions of the cranked shell model. These results suggest that the $\nu h_{9/2}$ states assume a greater role in the rotationally aligned configurations along the yrast line. Furthermore, the decay path from the $13/2^+$ isomer to the $7/2^-$ ground state has been determined and the multipolarities of the depopulating transitions deduced using γ-ray and conversion electron spectroscopy. Th observation of the isomer decay path has allowed the relative excitation energies of single-particle $\nu f_{7/2}$, $\nu h_{9/2}$ and $\nu i_{13/2}$ band heads to be fixed. In addition, the yrast band in ^{162}W has been confirmed by recoil-decay tagging and the level scheme of ^{164}W has been augmented.

3.1 Motivation and previous work

Understanding the evolution of nuclear structure towards closed shells is a long-standing goal of nuclear physics. Excitation level schemes of nuclei over long chains of isotopes allow changes to be elucidated in the delicate interplay between the constituent single-particle structure and the collective behaviour that arises from interactions between these constituents. However, measuring the properties of heavy neutron-deficient nuclei with neutron numbers approaching both the $N = 82$ closed shell and the proton drip line is challenging from an experimental viewpoint. Low production cross sections for the most neutron-deficient nuclei in this region, together with high backgrounds arising from other reaction products, limit the viability of measurement techniques that can be easily applied closer to the line of stability. Recently, the application of selective tagging techniques [Sc86, Sim86, Paul95] has allowed excited states in the most neutron-deficient W-Os-Pt-Hg nuclei to be observed, in many cases, for the first time [Keen01, Joss04, King98, O'Don09]. Even for the most weakly populated excited states, rudimentary information from the low-spin excitation level schemes can be revealing. Figure 1(a) shows the variation of the $E(4^+)/E(2^+)$ state energy ratios, as a function of neutron number, for the ground-state bands of the even-even Hf-W-Os nuclei. Figure 1(b) indicates that this trend can be interpreted in terms of diminishing quadrupole deformation with decreasing neutron number. Figure 1 shows that both the $E(4^+)/E(2^+)$ ratio and the deformation change smoothly, but distinctly, over a small range of neutron numbers approaching $N = 82$ from deformed rotors, through gamma-soft shapes towards the $N = 82$ shell closure. As such nuclei between the deformed and spherical regimes are often labelled 'transitional'.

In gamma-soft nuclei, the overall properties of the nucleus are sensitive to the occupation of core-polarising orbitals near the Fermi surface. This is particularly

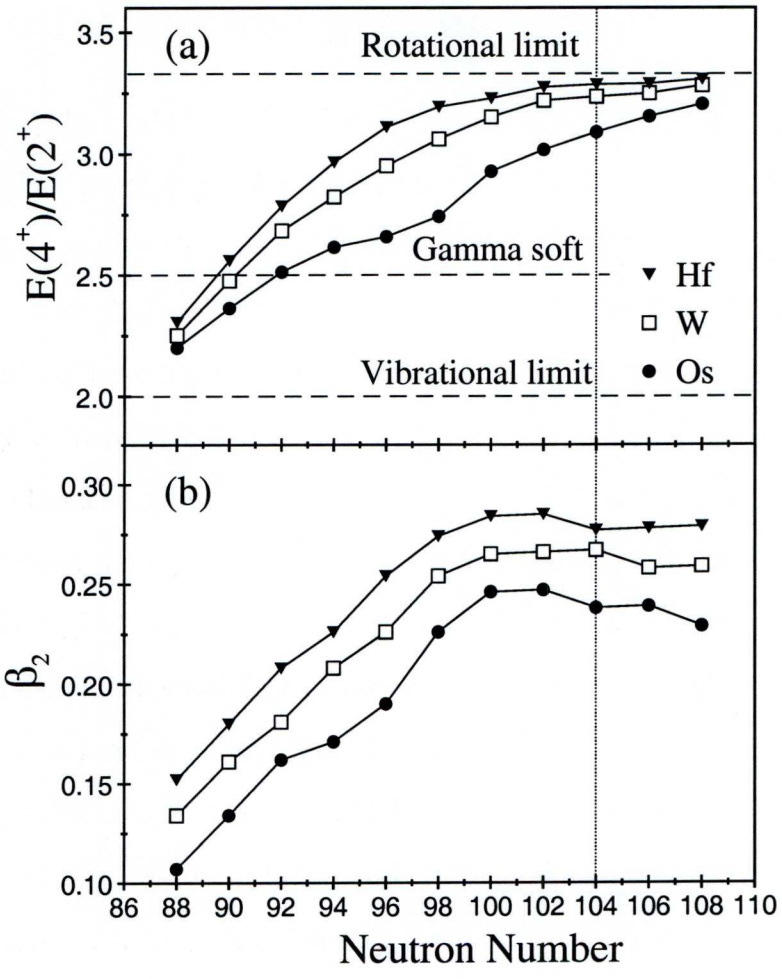

Figure 3.1: (a) $E(4^+)/E(2^+)$ ratios for Hf, W and Os isotopes as a function of neutron number. The rotational and vibrational limits are indicated as dashed lines. The neutron midshell at N=104 is indicated by a dotted line. (b) Variation of calculated ground-state quadrupole deformation parameters as a function of neutron number [MNK95]

important for nuclei such as ^{164}W, which has an $E(4^+)/E(2^+)$ ratio of 2.47, close to the O(6) limit for a gamma-soft shape (2.50). Indeed, in ^{164}W the proton and neutron Fermi surfaces lie at the top and bottom of their respective subshells presenting the ideal conditions for gamma-softness [Lean83]. Figure 3.2 shows representative proton and neutron Nilsson diagrams for the $A \sim 160$ mass region. At the predicted deformation parameters for ^{164}W (ε_2=0.15), the proton Fermi

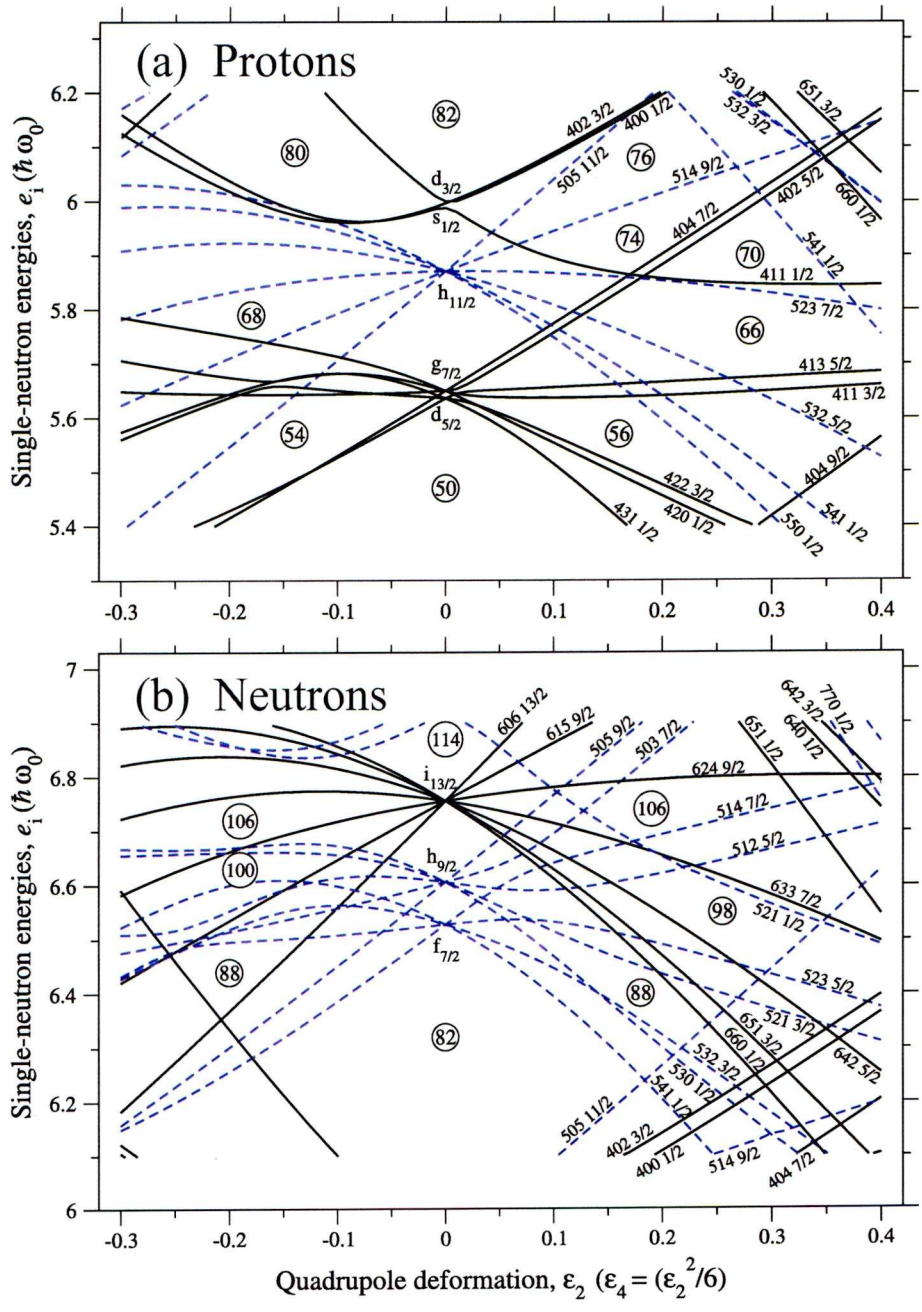

Figure 3.2: Theoretical single-neutron (a) and single proton (b) energies, calculated with the A=150 parameters [Beng90], shown as a function of quadrupole deformation. Positive-parity levels are denoted by solid (black) lines and negative-parity levels by dashed (blue) lines, respectively. The levels are labelled by asymptotic quantum numbers [$Nn_3\Lambda$]. This figure has been adapted from reference [Paul09]

surface lies in a region of low level density near the high-Ω $h_{11/2}$ states.

The neutron Fermi surface lies close to the high-j, lowest-Ω $i_{13/2}$ orbital and negative-parity orbitals originating from both the $f_{7/2}$ and $h_{9/2}$ subshells. The $i_{13/2}$ neutron orbital dominates the yrast spectra of the $N > 90$ W isotopes and the lowest energy multi-quasiparticle configurations involve one (odd-A) or two (even-A) $i_{13/2}$ neutrons [Simp91, Simp92, Th92b]. Figure 3.2(b) shows that with decreasing deformation towards the closed $N = 82$ shell, the $i_{13/2}$ neutron states achieve increasingly higher excitation energies relative to the Fermi surface allowing the negative parity $f_{7/2}$ and $h_{9/2}$ states to form the yrast configurations.

This scenario was confirmed experimentally in γ-ray spectroscopy experiments probing the neutron-deficient W isotopes. Simpson *et al.* observed the yrast band in ^{164}W up to moderately high spin ($I^{\pi} = 28^{+}$) and deduced a gain in aligned angular momentum ($\Delta I_x = 11\hbar$) consistent with the rotational alignment of a pair of $i_{13/2}$ neutrons [Simp91]. Dracoulis *et al.* made the first measurements of the lighter even-even neighbour, ^{162}W and measured a comparatively lower alignment gain at the first backbend ($\Delta I_x = 6\hbar$) [Drac92]. The first rotational alignment in the yrast band ^{162}W was attributed to an $\nu(h_{9/2})^2$ configuration on the basis of the measured alignment [Drac92]. These results indicate that the influence of the $i_{13/2}$ orbital wanes for isotopes with $N < 90$. Thus, the nucleus ^{163}W ($N = 89$) occupies a pivotal location in the transitional W isotopes in which the competition between the $h_{9/2}$ and $i_{13/2}$ orbitals to form the yrast configurations is most pronounced. Nuclear spectroscopy of the odd-neutron nucleus ^{163}W provides an ideal opportunity to identify configurations based upon these orbitals and probe the delicate interplay between single-particle and collective effects.

The first observation of excited states in ^{163}W was made by Dracoulis *et al.*, who observed a collective band based upon the $i_{13/2}$ state [Drac92]. This Chapter reports a significant extension to the excitation level scheme for ^{163}W, including the decay path from the $i_{13/2}$ isomer to the ground state. In addition, analysis

of the neighbouring even-N isotopes has extended the level scheme of ^{164}W and confirmed the assignment of γ rays in yrast band ^{162}W using the RDT technique.

3.2 Experimental Details

The experiment was performed at the Accelerator Laboratory of the University of Jyväsklä, Finland. Excited states in $^{164-x}$W isotopes were populated using the ^{106}Cd(^{60}Ni,2pxn) reactions at a beam energy of 270 MeV. The target was a 1.0 mg/cm^2 thick, self-supporting ^{106}Cd foil of 96.5% isotopic enrichment. An average beam current of 4 pnA was used for 121 hours. Prompt γ rays were detected at the target position by the JUROGAM γ-ray spectrometer [Beau96] consisting of 43 EUROGAM-type escape-suppressed germanium spectrometers [Beau92]. The recoiling fusion-evaporation residues were separated from fission products and scattered beam by the RITU gas-filled recoil separator [Le95] and deposited into the double-sided silicon strip detectors of the GREAT spectrometer [Page03] at the focal plane. Recoiling nuclei were distinguished from the residual scattered beam and radioactive decays by energy loss and (in conjunction with the DSSDs) time of flight methods using the GREAT multiwire proportional counter.

In addition to the planar and clover Ge detectors of GREAT spectrometer, two VEGA clover detectors [Gerl00] were positioned perpendicular to the plane of implantation outside the GREAT vacuum chamber. All detector signals from JUROGAM and GREAT were passed to the total data readout (TDR) acquisition system [Laz01] where they were time stamped with a precision of 10ns to allow accurate temporal correlations between γ rays detected at the target position, recoil implants at the focal plane and their subsequent radioactive decays. These triggerless data were sorted into γ-γ matrices and γ-γ-γ cubes using GRAIN [Rah08] and analysed with the RADWARE software packages [Rad95].

Table 3.1: Measured α decay properties of the light tungsten isotopes from previous measurements. The values are error weighted averages determined from the published values found in the final column.

Isotope	E_α (keV)	$t_{1/2}$ (ms)	b_α (%)	References
^{162}W	5536(3)	1364(37)	49.4(18)	[Hof79, Hof81, Page96, Rytz91]
^{163}W	5384(2)	2803(169)	18.2(18)	[Cab78, East73, Hof79, Page96, Rytz91]
^{164}W	5150(2)	6020(320)	4.4(9)	[East73, Hof79, Page96, Rytz91, Toth75]

3.2.1 Gamma-ray coincidence analysis

In ideal circumstances, the RDT technique provides high-confidence correlations between γ rays and subsequent radioactive decays. The optimal conditions for such studies are short half-lives, high α-decay branching ratios and a distinctive decay energy. Ideally, the implantation rate should be low in comparison to the half-life of the 'tagging' decay, i.e. no greater than one implantation every 3-5 half-lives. If two ions impinge on a pixel in a time comparable to the half-life, a random correlation will occur rendering an unreliable identification. The half-lives of ^{163}W and ^{164}W are long in comparison to the average recoil rate 1.37 kHz (or $\sim$ 1 per pixel per second), see Table 3.1. If a search time of $5 \times t_{1/2}$ is used to collect 96% of the available α decays, a correlation time of $\sim$ 15s would be required. Thus the effectiveness of recoil-decay tagging, in this case, is limited. The cross sections have been estimated from the measured α decay yields, see Fig. 3.3. Assuming a RITU separator transmission efficiency of 30%, a geometric coverage of 80% and a detection efficiency of 55% and using the branching ratios in Table 3.1, cross sections for ^{164}W and ^{163}W have been estimated as $\sim$2mb and

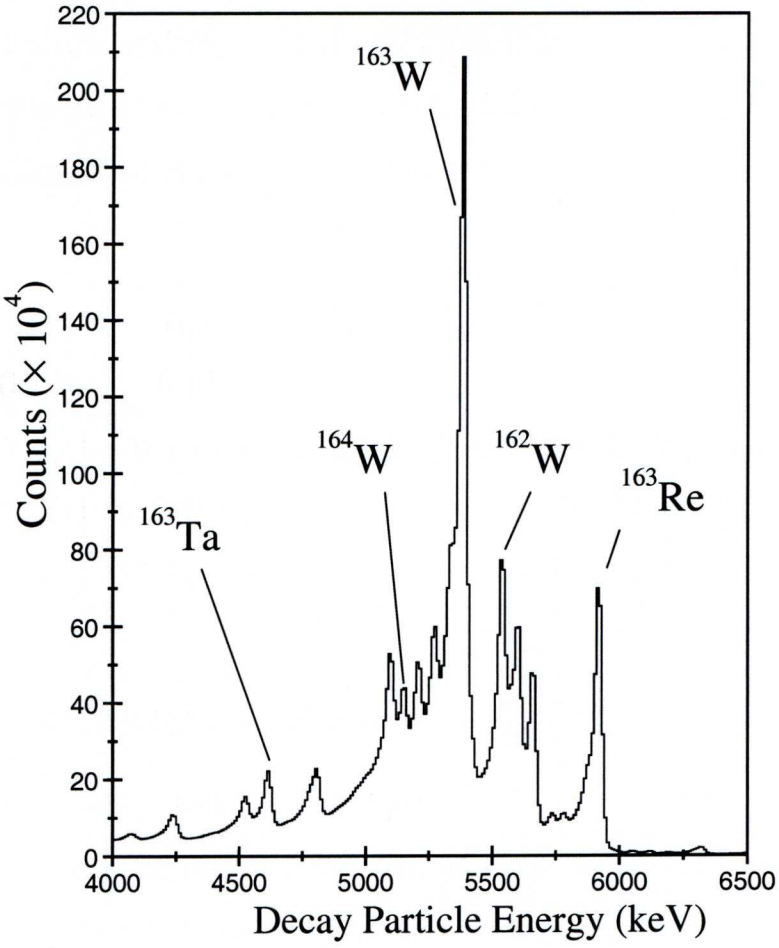

Figure 3.3: Energy spectrum of all decays occurring within 600 ms of an ion implantation into the same DSSD pixel.

~4mb, respectively. Since the cross sections for these W isotopes are substantial, high-fold γ-ray coincidences were employed in order to select γ-ray decay paths in the light W isotopes from the background of γ rays arising from other intense channels.

A total of 1.18×10^8 three-fold events, detected in coincidence with a recoil implantation at the focal plane, were sorted offline into an $E_{\gamma 1}$-$E_{\gamma 2}$-$E_{\gamma 3}$ cube. The cube used fold 3 events exclusively; fold > 3 events were discarded in order to prevent double counting when summing high-fold coincidences [Beau95]. The cube was analysed with the LEVIT8R graphical analysis software package [Rad95].

Level schemes for the light tungsten isotopes were constructed using relative γ-ray intensities and coincidence relationships from spectra generated from the cube.

3.2.2 Multipolarity assignments

Multipolarity assignments for the strongest γ-ray transitions were obtained from measurements of angular intensity ratios using the the directional correlations from oriented states (DCO) method [KSW72]. DCO measurements were made exclusively using fold three events. These data were sorted such that γ-ray coincidences were demanded with one or more γ-ray 'gating' transitions to select the band. A further condition was demanded to ensure that the remaining two coincident γ rays were observed in detectors at extreme ($\theta = 157.6°$) and normal ($\theta = 85.84°$ or $94.16°$) angles relative to the beam direction. Gamma-ray coincidences satisfying these conditions were incremented into a $\theta_{extreme}$ versus θ_{normal} DCO matrix. No angular criteria were applied in the selection of the gating transitions.

In the resulting DCO matrix, further coincidences with γ-ray transitions in the tungsten isotopes were made. The relevant peak areas in the two summed projections were then extracted and the ratio of the areas in the extreme region $\theta = 157.6°$ (gated on $\theta \approx 90°$ axis) to the region around the normal $\theta \approx 90°$ (gated on $\theta = 157.6$ axis) were obtained according to the relation,

$$R_{DCO} = \frac{I(157.6°, gated\ 90°)}{I(90°, gated\ 157.6°)}. \tag{3.1}$$

In order to obtain typical values for stretched quadrupole and stretched dipole transitions, the R_{DCO} value was measured for known stretched E2 and E1 transition in ^{164}W that were previously measured using the POLYTESSA spectrometer by Hanna [Han93]. The method employed clearly discriminated between stretched

quadrupole and stretched dipole transitions, yielding DCO ratios of 0.94(9) and 0.67(14) for the 490 keV and the 752 keV transitions, respectively.

3.3 The even-N isotopes

3.3.1 ^{164}W (N=90)

The ground state band was first observed by Simpson *et al.* [Simp91] in an experiment using the POLYTESSA γ-ray spectrometer in conjunction with the Daresbury recoil separator [Jam88]. The yrast band was tentatively established beyond the first backbend to spin and parity $I^{\pi}=28^{+}$. A second band was observed in studies by Hanna [Han93] using the ^{104}Pd(^{63}Cu,p2n)^{164}W* reaction (E_{beam} = 285 MeV), also with the POLYTESSA γ-ray spectrometer and the Daresbury recoil separator. A negative-parity structure was observed with odd spins extending to $I^{\pi}=(23^{-})$. This structure was linked to the ground state band by three linking transitions at 936, 753 and 518 keV for which DCO measurements established two of these transitions as stretched (ΔI = 1) dipoles. In a parallel study, Dracoulis *et al.* used the ^{109}Ag(^{58}Ni,p2n)^{164}W* reaction (E_{beam} = 285 MeV) to populate excited states in ^{164}W [Drac92]. This reaction was employed in experiments using the GAMMASPHERE [Lee92] and CAESAR γ-ray spectrometers. The ground state band was observed to a tentative spin (28) state. In this experiment, the side band observed by Hanna was confirmed at the same excitation energy and an additional negative-partity band was observed to a tentative (23^{-}) state.

Figure 3.5 shows typical spectra from the present work obtained from a recoil-$\gamma\gamma\gamma$ cube. In this work the ground state band is established up to an excitation energy of 9301 keV and spin (30^{+}), see Fig. 3.4. An additional decay path from the known S band to the low-spin states of the ground state band has been observed. This decay branch comprising γ-ray transitions at 532 and 791 keV

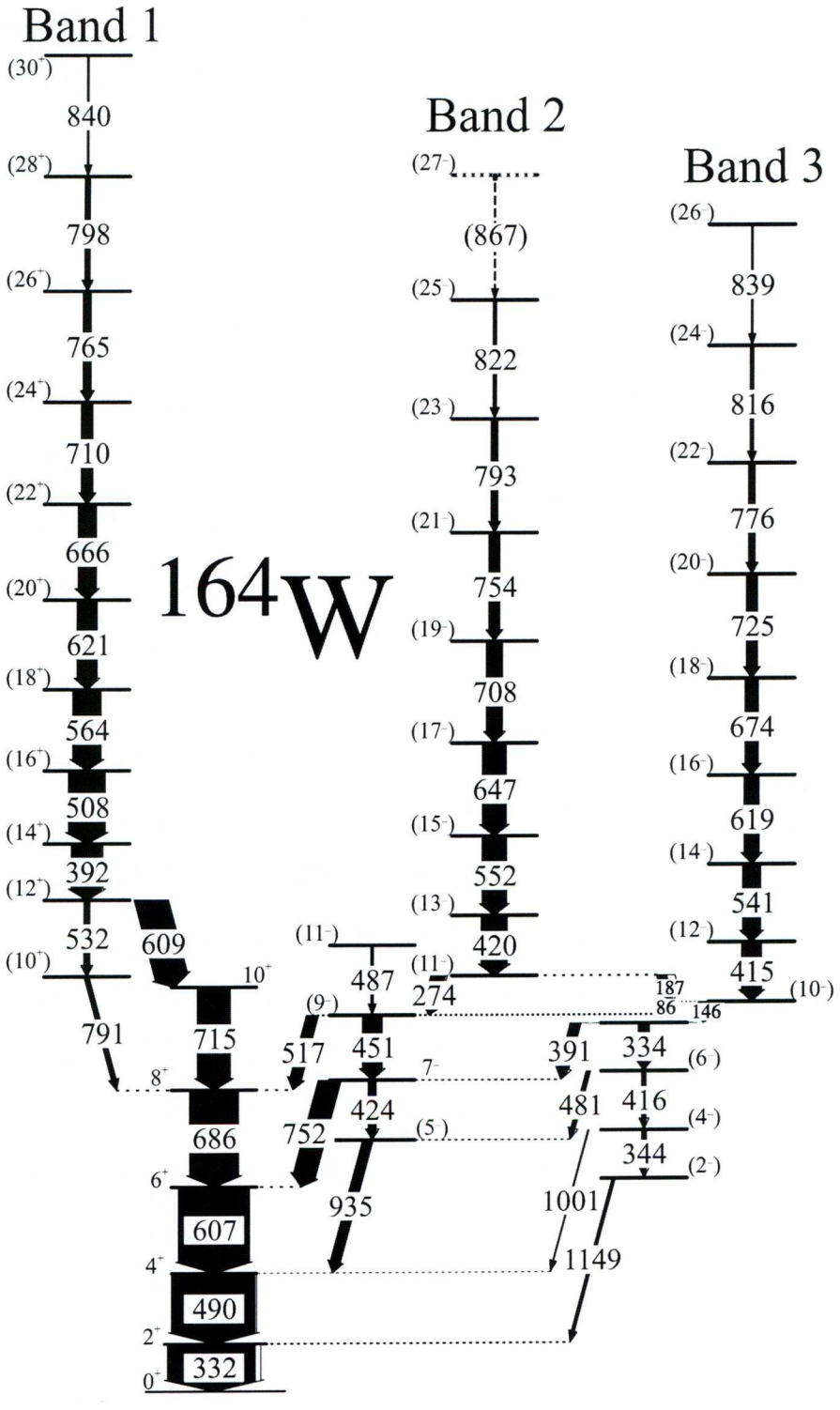

Figure 3.4: Level scheme deduced for ^{164}W. The transition energies are given in keV and their relative intensities are proportional to the widths of the arrows.

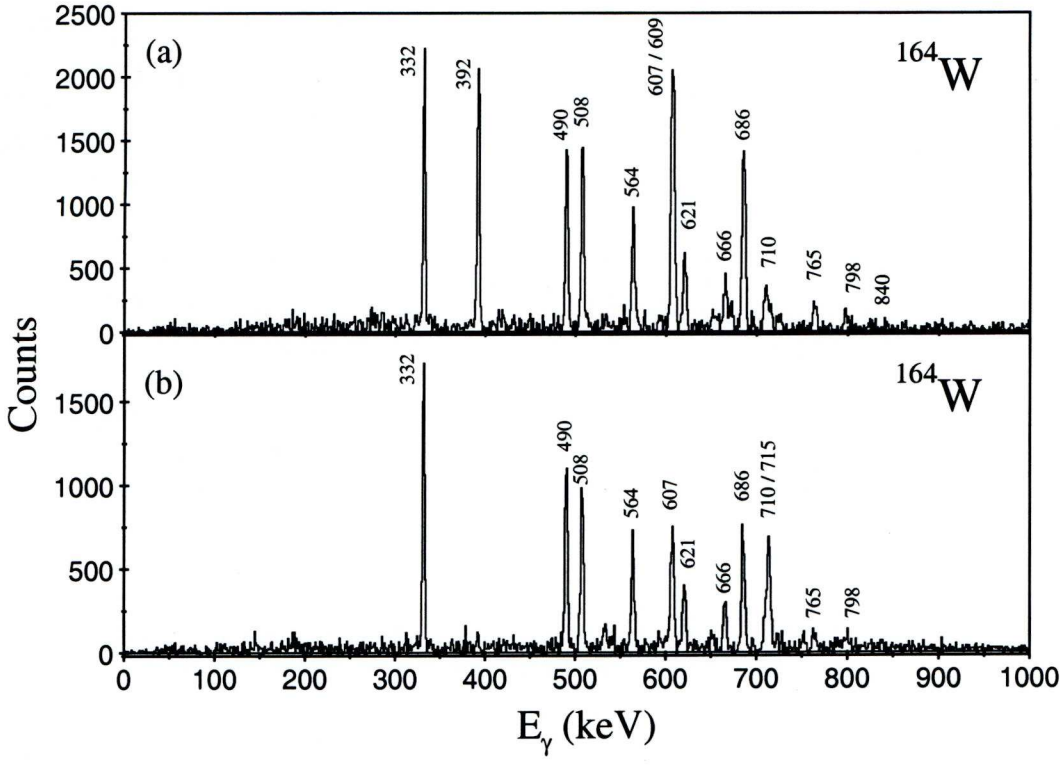

Figure 3.5: (a) Summed triple-gated γ-ray spectrum generated by demanding triple gates between the 715 keV transition and a list of Band 1 transitions comprising the 332, 490 and 607 keV transitions. (b) Spectrum showing γ rays in coincidence with the 392 keV and 609 keV transitions showing γ rays in Band 1.

is, in part, assumed to be the non-yrast continuation of the paired ground-state band.

Figure 3.6 shows typical spectra obtained from a recoil-$\gamma\gamma\gamma$ cube highlighting transitions in Band 2. Angular correlations confirm the 752 keV transition as a stretched dipole transition. Thus, Band 2 is assigned as an odd-spin structure on the basis of current and previous measurements. These three-fold coincidence measurements confirm the ordering of γ rays in the cascade and extend the band to a tentative spin and parity (27^-).

The additional cascade observed by Dracoulis *et al.*, labelled as Band 3 in Fig. 3.4, has been reproduced and extended to a tentative spin and parity of

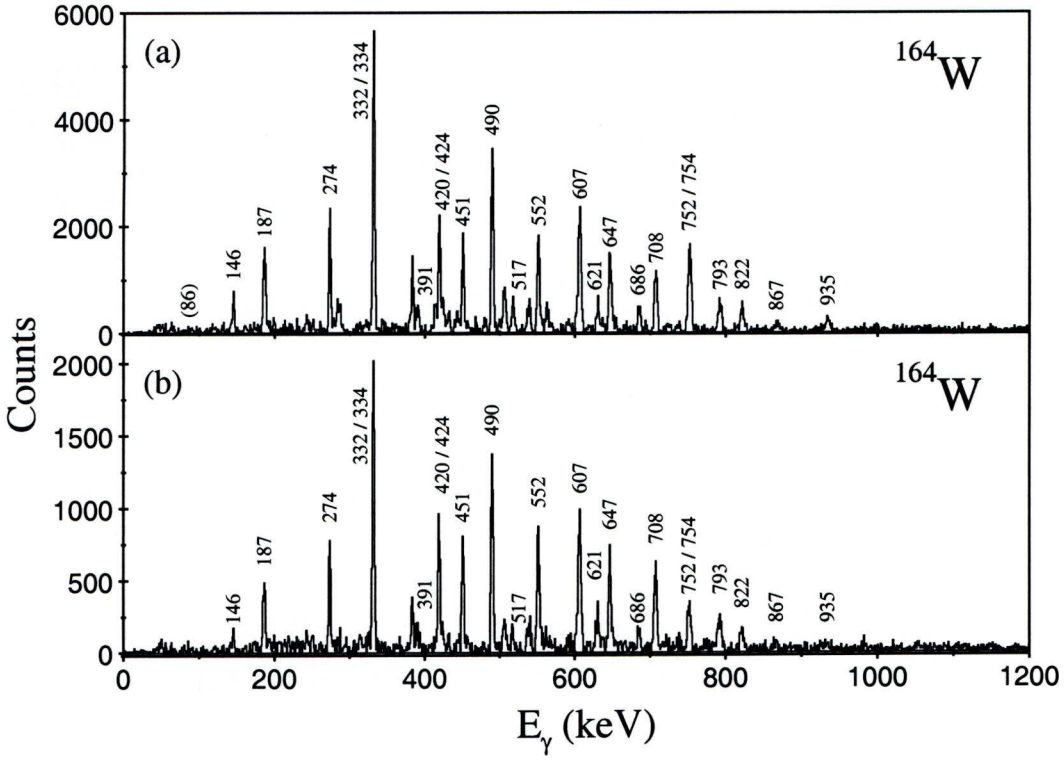

Figure 3.6: (a) Summed triple-gated γ-ray spectrum generated using a list of Band 2 transitions comprising the 420, 552, 647, 708, 754 and 793 keV transitions. (b) Summed triple-gated γ-ray spectrum generated by demanding triple gates between the 752 keV linking transition and the list described above.

(26^-). Typical coincidence spectra showing γ rays in Band 3 are shown in Fig. 3.7. The most significant extension to the ^{164}W level scheme is represented by the decay path from Band 3 to the low-lying states of the ground state band. A new cascade of γ-ray transitions at 344, 416 and 334 keV has been observed continuing Band 3 to lower spin. In addition, linking transitions at 391 and 481 keV have been observed connecting the (8^-) and (6^-) states in Band 3 to the ground state band via the (7^-) and (5^-) states in Band 2. In addition, two further γ rays were observed to feed the ground state band directly. Two weak γ rays at 1101 and 1149 keV were observed to feed the 4^+ and 2^+ states, respectively. Assuming that the linking transitions between the side bands and the ground

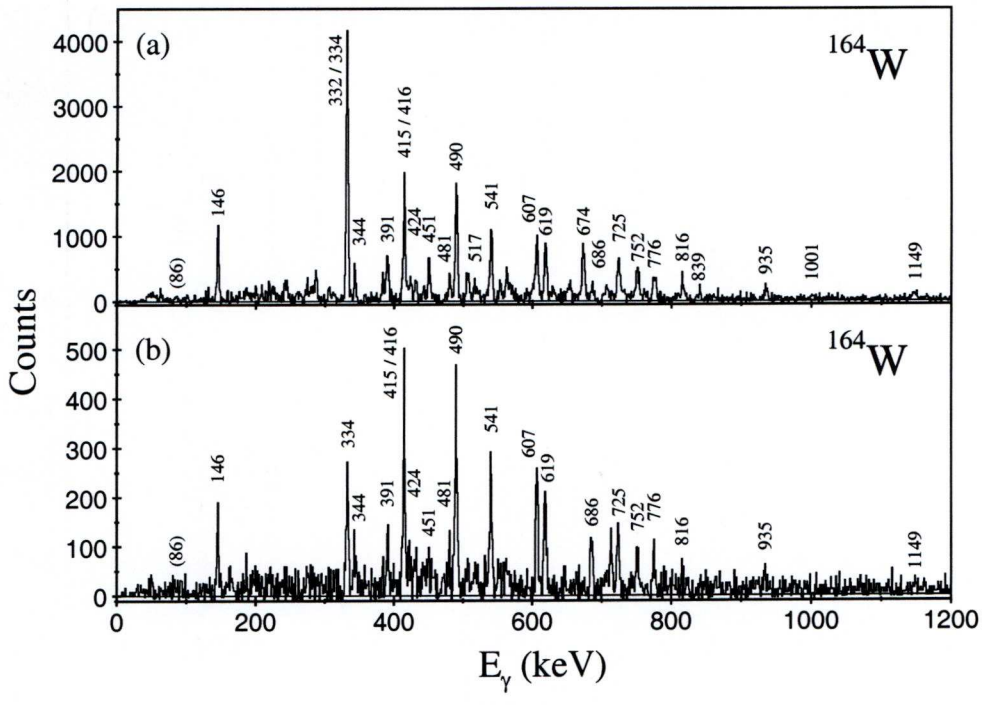

Figure 3.7: (a) Summed triple-gated γ-ray spectrum generated using a list of Band 3 transitions comprising the 415, 541, 619, 674, 725 and 776 keV transitions. (b) Spectrum showing γ rays in coincidence with the 332 keV and 674 keV transitions showing γ rays in Band 3.

state band are electric dipoles, it has been possible to determine ratios of reduced transition probabilities by measuring the branching ratio of the interband to in-band transitions $\lambda_{out/in}$, and substituting in to the equation [BM75],

$$\frac{B(E1; I \rightarrow I-1)}{B(E2; I \rightarrow I-2)} = \frac{\lambda_{out/in}}{1.3 \times 10^6} \frac{[E_\gamma(\Delta I = 2)]^5}{[E_\gamma(\Delta I = 1)]^3} (\mathrm{fm}^{-2}), \tag{3.2}$$

where γ-ray energies are in MeV. Measured $B(E1; I \rightarrow I-1)/B(E2; I \rightarrow I-2)$ ratios are listed in Table 3.2, together with estimated $B(E1)$ strengths. The deduced $B(E1)$ values are all greater than 10^{-5} Wu. The observation of such high $B(E1)$ strength is often cited as evidence for octupole correlations in nuclei [But96].

Table 3.2: Experimental $B(E1)/B(E2)$ reduced transition probability ratios and deduced $B(E1)$ strengths in ^{164}W.

I	E_{Ex} (keV)	$\frac{I_\gamma(E1)}{I_\gamma(E2)}$	$\frac{B(E1)}{B(E2)}$ (10^{-7} fm^{-2})	$B(E1)$ (10^{-3} e^{2}fm^2)	$B(E1)$ (10^{-3} W.u.)[a]
(9)	2632(9)	0.55(10)	0.57(11)	2.73(96)	1.42(31)
(7)	2181(6)	3.37(12)	0.83(30)	3.81(14)	1.99(74)
(6)	2239(10)	0.83(49)	0.68(40)	3.07(19)	1.60(96)
(4)	1824(5)	0.23(10)	0.008(4)	0.034(16)	0.02(1)

[a] 1 W.u. = 1.92 e^{2}fm^2.

The observation of low-spin octupole vibrations that connect the two-quasiparticle bands to the ground state are common in $A \sim 160$ even-even nuclei [Simp87, Mo87, Joss01]. Octupole vibrations are to be expected to arise from interactions between orbitals near the Fermi surface that differ in orbital angular momentum by $\Delta l = 3$. In this region, octupole correlations are expected to arise from the $h_{11/2}$ and $d_{5/2}$ proton and $i_{13/2}$ and $f_{7/2}$ neutron orbitals. The deduced level scheme for ^{164}W is displayed in Fig. 3.4 and the measured properties of γ rays in ^{164}W are listed in Table 3.3.

Table 3.3: Measured properties of γ ray transitions assigned to ^{164}W. Energies are accurate to $\pm$0.5 keV for the strong transitions (I_γ >10%) rising to $\pm$2.0 keV for the weaker transitions. Newly observed transitions are labelled by a †.

E_γ (keV)	I_γ (%)	DCO	J_i^π	$\rightarrow$	J_f^π	Multipolarity	Band
331.9	100.0(6)	0.79(10)	2^+	$\rightarrow$	0^+	E2	1
490.4	95(6)	0.94(9)	4^+	$\rightarrow$	2^+	E2	1
606.6	80(5)	0.84(13)	6^+	$\rightarrow$	4^+	E2	1
686.0	55(4)	1.69(40)	8^+	$\rightarrow$	6^+	E2	1
714.7	37(3)	1.23(19)	10^+	$\rightarrow$	8^+	E2	1
608.9	37(3)		(12^+)	$\rightarrow$	(10^+)		1
391.9	34.6(23)		(14^+)	$\rightarrow$	(12^+)		1
508.0	41(3)		(16^+)	$\rightarrow$	(14^+)		1
564.1	31.7(21)		(18^+)	$\rightarrow$	(16^+)		1
621.4	22.5(16)		(20^+)	$\rightarrow$	(18^+)		1
666.3	20.5(15)		(22^+)	$\rightarrow$	(20^+)		1
710.4	13.1(10)		(24^+)	$\rightarrow$	(22^+)		1
764.6	9.2(8)		(26^+)	$\rightarrow$	(24^+)		1
798.3	6.1(6)		(28^+)	$\rightarrow$	(26^+)		1
840.1†	2.1(4)		(30^+)	$\rightarrow$	(28^+)		1
531.6†	6.8(7)		(12^+)	$\rightarrow$	(10^+)		1
791.0†	5.6(11)		(10^+)	$\rightarrow$	(8^+)		1
935.3	11.9(15)		(5^-)	$\rightarrow$	(4^+)		2$\rightarrow$1
751.9	25.6(21)	0.67(14)	7^-	$\rightarrow$	6^+	E1	2$\rightarrow$1
517.4	13.5(10)		(9^-)	$\rightarrow$	(8^+)		2$\rightarrow$1
424.4	9.0(8)		(7^-)	$\rightarrow$	(5^-)		1
451.0	22.1(16)		(9^-)	$\rightarrow$	(7^-)		1
487.3	2.9(8)		(11^-)	$\rightarrow$	(9^-)		1

E_γ (keV)	I_γ (%)	DCO	J_i^π	$\rightarrow$	J_f^π	Multipolarity	Band
273.7	16.3(11)	1.26(26)	(11^-)	$\rightarrow$	(9^-)	E2	2
419.7	28.9(19)		(13^-)	$\rightarrow$	(11^-)		2
551.7	27.5(19)		(15^-)	$\rightarrow$	(13^-)		2
647.2	26.9(18)		(17^-)	$\rightarrow$	(15^-)		2
707.6	18.0(13)		(19^-)	$\rightarrow$	(17^-)		2
753.7	12.5(11)		(21^-)	$\rightarrow$	(19^-)		2
792.6	7.5(7)		(23^-)	$\rightarrow$	(21^-)		2
822.5†	4.1(5)		(25^-)	$\rightarrow$	(23^-)		2
867.1†	1.7(4)		(27^-)	$\rightarrow$	(25^-)		2
1148.5	3.6(15)		(2^-)	$\rightarrow$	2^+		3$\rightarrow$1
1001.2†	1.3(4)		(4^-)	$\rightarrow$	4^+		3$\rightarrow$1
480.9†	4.7(7)		(6^-)	$\rightarrow$	(5^-)		3$\rightarrow$2
391.0	10.7(11)		(8^-)	$\rightarrow$	7^-		3$\rightarrow$2
343.6†	5.0(8)		(4^-)	$\rightarrow$	(2^-)		3
415.5†	4.9(7)		(6^-)	$\rightarrow$	(4^-)		3
334.0†	11.7(10)		(8^-)	$\rightarrow$	(6^-)		3
145.7	11.2(9)	1.34(59)	(10^-)	$\rightarrow$	(8^-)	E2	3
85.8	< 2.00		(10^-)	$\rightarrow$	(9^-)		3$\rightarrow$2
187.4	11.2(8)		(11^-)	$\rightarrow$	(10^-)		2$\rightarrow$3
414.6	22.0(16)		(12^-)	$\rightarrow$	(10^-)		3
540.5	20.1(14)		(14^-)	$\rightarrow$	(12^-)		3
619.1	17.0(13)		(16^-)	$\rightarrow$	(14^-)		3
673.8	15.1(11)		(18^-)	$\rightarrow$	(16^-)		3
724.6	12.5(10)		(20^-)	$\rightarrow$	(18^-)		3
775.5	7.0(7)		(22^-)	$\rightarrow$	(20^-)		3
816.4	3.7(5)		(24^-)	$\rightarrow$	(22^-)		3
839.3†	1.8(4)		(26^-)	$\rightarrow$	(24^-)		3

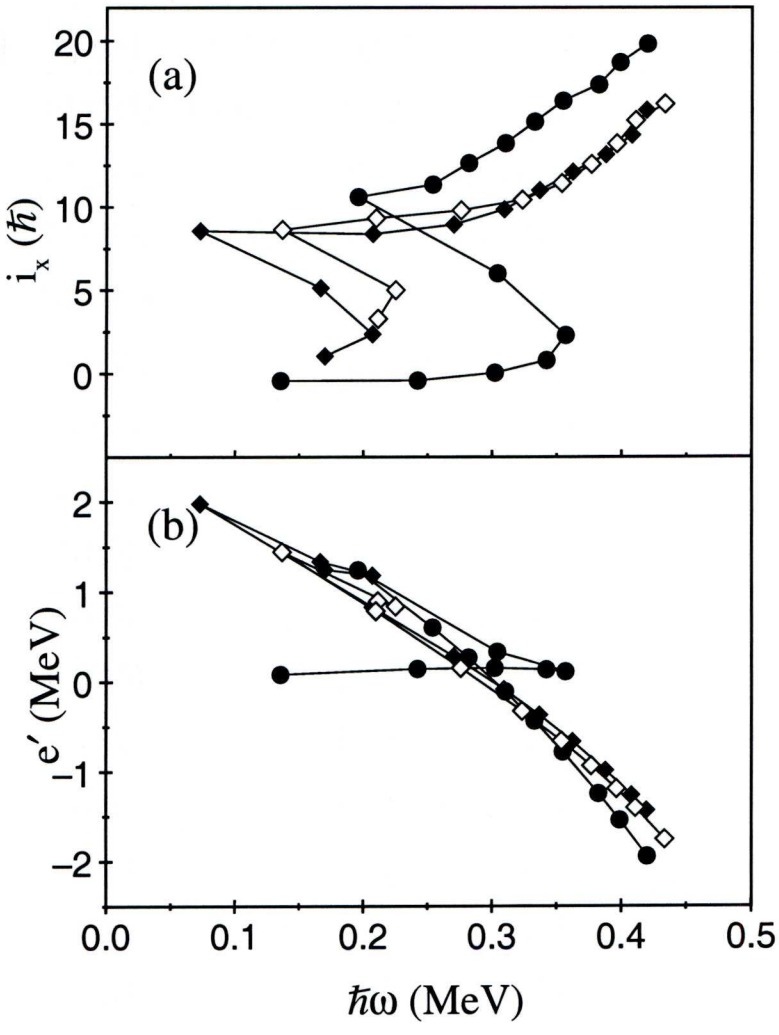

Figure 3.8: The alignment, i_x as a function of rotational frequency for the bands in ^{164}W. A rotational reference, based on a configuration with a variable moment of inertia defined by the Harris parameters J_0= 12.5 $\hbar^2$MeV^{-1} and J_1=60 $\hbar^4$MeV^{-3}, has been subtracted from each band. (b) Experimental routhians e' as a function of rotational frequency for the bands in ^{164}W. Band 1 is represented by filled circles, Band 2 by open diamonds and Band 3 by filled diamonds.

Figure 3.8(a) shows the alignment, i_x, as a function of rotational frequency for the bands in ^{164}W extracted from the level scheme in Fig. 3.4. The ground state band shows an alignment gain of $\Delta I_x = 11\hbar$ at $\hbar\omega$=0.2 MeV. A crossing frequency $\hbar\omega_c$=0.29 MeV is extracted from the experimental Routhians as a function of

rotational frequency plotted in Fig. 3.8(b). The alignments extracted for Bands 2 and 3 have similar behaviour as a function as rotational frequency. At low frequency, the alignments for both bands are low but quickly achieve an alignment of around $9\hbar$ at 0.2 MeV, which is lower than the alignment measured for Band 1. At rotational frequencies $\hbar\omega$ >0.2 MeV, the alignment of both side bands increases smoothly.

The features in the alignment plots can be used to identify the underlying orbital configurations of the bands within the context of Woods-Saxon cranking calculations [Cwi87]. Quasiparticle Routhians, e', calculated for ^{164}W are displayed in Fig. 3.9. The quasiparticle Routhians are labeled according to the convention of reference [Paul97] as listed in Table 3.4. In these calculations the pairing strength is modelled with a frequency dependent modification, so that the pairing

Table 3.4: Adopted convention for labelling quasiparticle routhians.

Label	Parity & Signature (π,α)	Shell Model State
	Quasineutrons	
A	$(+,+1/2)_1$	$i_{13/2}$
B	$(+,-1/2)_1$	$i_{13/2}$
E	$(-,-1/2)_1$	$h_{9/2}, f_{7/2}$
F	$(-,+1/2)_1$	$h_{9/2}, f_{7/2}$
G	$(-,-1/2)_2$	$h_{9/2}, f_{7/2}$
H	$(-,+1/2)_2$	$h_{9/2}, f_{7/2}$
	Quasiprotons	
e	$(-,-1/2)_1$	$h_{11/2}$
f	$(-,+1/2)_1$	$h_{11/2}$

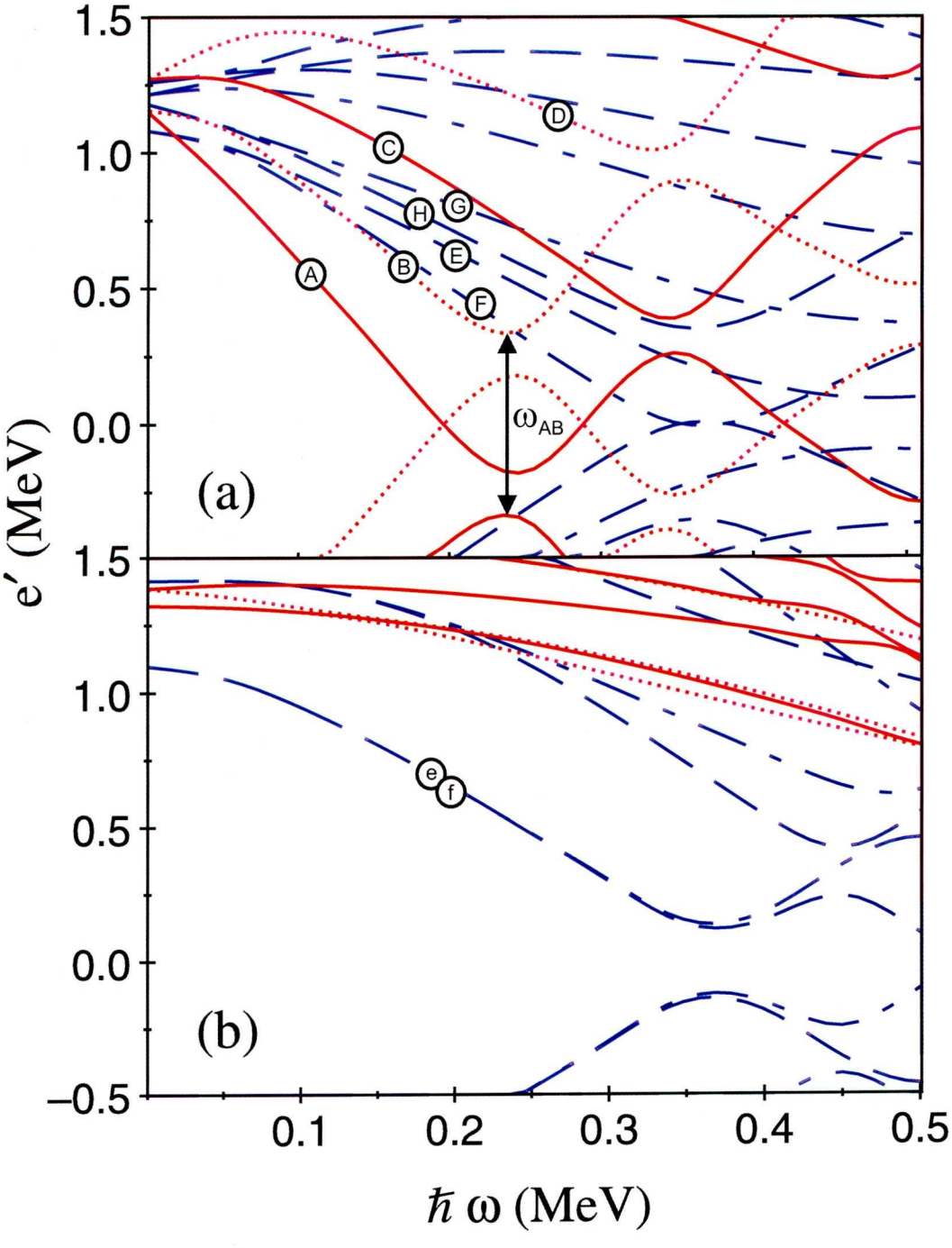

Figure 3.9: Cranked Woods-Saxon routhian diagrams for ^{164}W assuming deformation parameters (β_2=0.161, β_2=0.010,γ=0) from reference [MNK95]. (a) Quasineutrons. (b) Quasiprotons.

is gradually reduced to 50% of the zero frequency value at $\hbar\omega$=0.7 MeV [Wyss88]. The deformation parameters (β_2=0.161, β_4=0.010) used in the cranking calculations are the values predicted by Moller et al [MNK95]. The quasineutron and quasiproton Routhians shown in Fig. 3.9 suggest that the high-j, low-Ω $i_{13/2}$ quasineutron orbitals (A and B) are the first to undergo a rotational alignment at $\hbar\omega$ ~0.24 MeV, which is lower than the experimental value. The value of the crossing frequency is sensitive to the deformation and pairing input parameters and so a minor discrepancy like this is not entirely unexpected. The alignment gain can be estimated from the slopes of the aligning Routhians ($i_x = de'/d\omega$). The predicted alignment gain from the rotational alignment of an $i_{13/2}$ quasineutron pair (AB) is expected to be Δi_x=10.6$\hbar$, which is in excellent agreement with the experimental value measured for Band 1. This interpretation is consistent with previous work [Simp91].

The experimental alignments for Bands 2 and 3 shown in Fig. 3.8(a) have lower alignments than observed for the $\nu(i_{13/2})^2$ (AB) configuration. This indicates that the configuration involves at least one quasiparticle Routhian with a shallower gradient. The next available quasineutron excitations are based on coupling a single $i_{13/2}$ quasineutron to one of the nearby negative-parity orbitals originating from the mixed $f_{7/2}, h_{9/2}$ configurations. The cranking calculations predict an alignment gain of ~9.5$\hbar$ for the AF and AE configurations. Therefore, bands 2 and 3 are likely to be signature partner bands based on the $\nu i_{13/2} \otimes \nu(f_{7/2}, h_{9/2})$ (AF/AE) coupling. The low-spin alignments of the negative-parity side bands are too low to represent a two quasiparticle excitation. These features are interpreted in terms of octupole correlations as indicated by the large $B(E1)$ reduced transition probabilities listed in Table 3.2.

The smooth alignment gain at higher frequencies is similar for all the aligned configurations suggesting a common physical origin. One possibility is the gradual alignment of the a and b quasiprotons originating from the $h_{11/2}$ sub-shell.

3.3.2 ^{162}W (N=88)

The yrast states in ^{162}W were first observed in experiments by Dracoulis *et al.* using the GAMMASPHERE and CAESAR spectrometers [Drac92]. In order to minimise the number of open reaction exit channels that could contribute to the γ-ray background, the ^{104}Pd(^{63}Cu,p2n)^{164}W* reaction was employed with a bombarding energy near the Coulomb barrier. In these experiments, the ground-state band was established to spin and parity 16^+. The level scheme could not be extended in the present work. However, it has been possible to confirm the identification of γ rays in ^{162}W by the application of the RDT technique.

The application of the RDT technique, where prompt γ rays are correlated with the subsequent radioactive decays, can provide an umambiguous identification of excited states to a specific nucleus. Figure 3.10(a) shows γ rays correlated with a recoil implanted in the GREAT spectrometer followed by the characteristic α decays of ^{162}W and its daughter ^{158}Hf detected within the same pixel. The search time for correlations was limited to 600 ms for the first decay and 8 s for the daughter decay. The γ rays of the ground state band in ^{162}W observed by Dracoulis *et al.* are unambiguously confirmed through recoil-decay correlations. An α(^{162}W)-tagged $\gamma\gamma$ matrix was sorted in order to confirm the level scheme established for ^{162}W. The time for recoil-decay correlations was limited to 600ms. The matrix contained 1.6×10^6 α-correlated $\gamma\gamma$ events. Figure 3.10(b) shows γ rays in coincidence with the 630keV transition and represents a typical γ-ray coincidence spectrum. The ground state band was confirmed to spin and parity (16^+). While other γ rays are apparent in Fig. 3.10(a), it has not been possible to establish excited bands with confidence in these data. Furthermore, it has not been possible to determine the multipolarities of the ground state band transitions due to limited statistics. The the level scheme is shown in Fig. 3.10(c) and the properties of γ rays in ^{162}W are listed in Table 3.5.

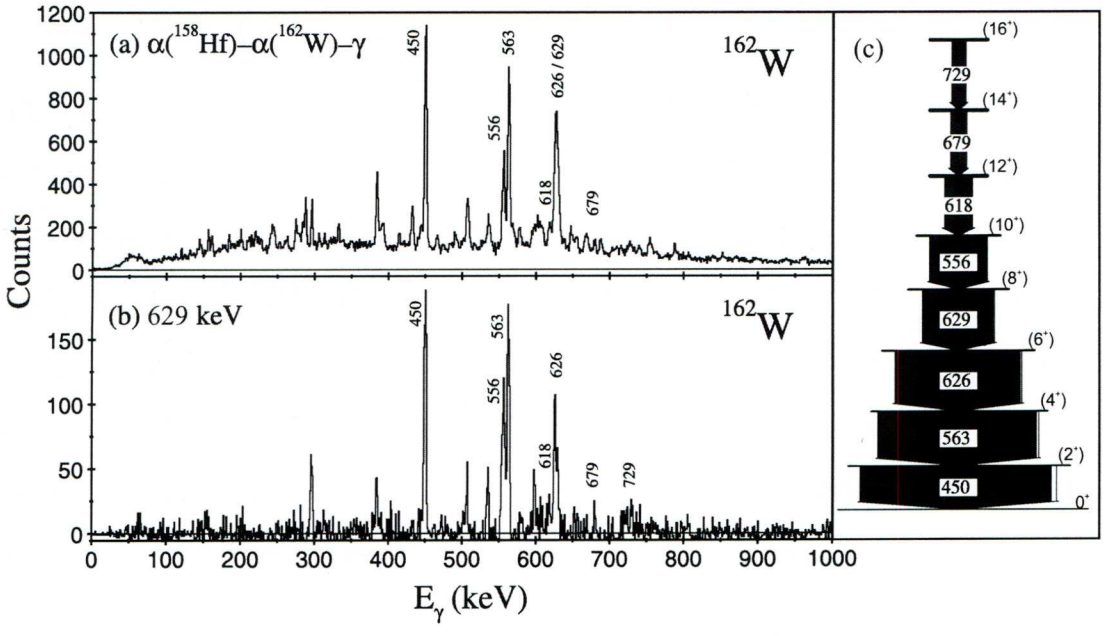

Figure 3.10: Gamma rays correlated with recoil implantations followed by the characteristic decay sequence $\alpha(^{162}\mathrm{W})$-$\alpha(^{158}\mathrm{Hf})$ within the same DSSD pixel of the GREAT spectrometer. The correlation time was limited to 600 ms for the first decay and 8 s for the second decay. (b) Gamma rays in coincidence with the 629 keV transition generated from an $\alpha(^{162}\mathrm{W})$-correlated $\gamma\gamma$ coincidence matrix. The time for recoil-decay correlations was limited to 600 ms. Gamma-ray transitions in the ground state band of ^{162}W are labelled by their energy in keV. (c) Level scheme deduced for ^{162}W. The transition energies are given in keV.

Figure 3.11(a) compares the the variation of aligned angular momentum as a function of rotational frequency for ^{162}W and ^{164}W. A backbending pattern is observed with a crossing frequency of ~0.3 MeV, see Fig. 3.11(b). The alignment gain for ^{162}W is much lower ($\sim 6\hbar$) than the corresponding gain for ^{164}W. This has been interpreted by Dracoulis *et al.* in terms of the rotational alignment of a pair of $h_{9/2}$ neutrons [Drac92]. While the even-N isotopes can reveal a change in the aligning orbitals at the Fermi surface it is by establishing structures in the intervening odd-N isotope that single-particle states can be probed more deeply.

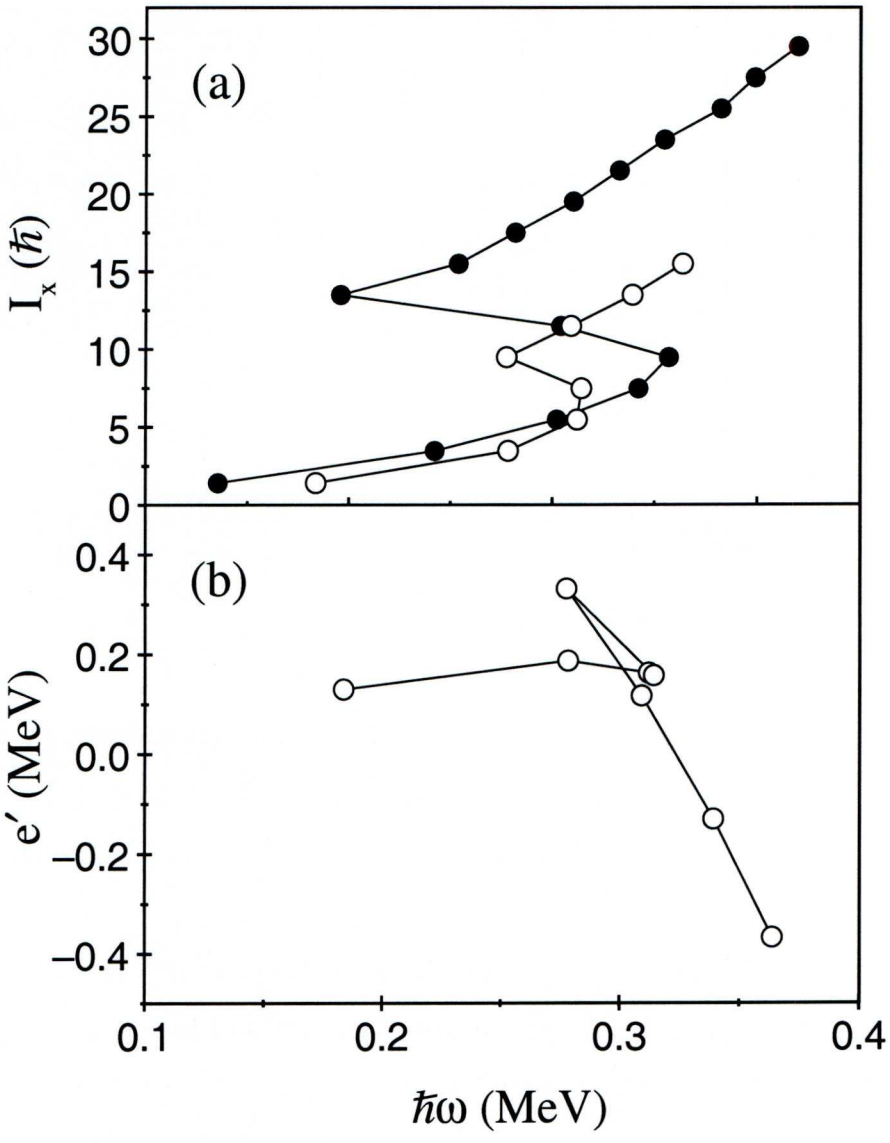

Figure 3.11: The total aligned angular momentum, I_x as a function of rotational frequency for the ground state bands in ^{162}W (open circles) and ^{164}W (filled circles). (b) Experimental Routhians e' as a function of rotational frequency for the ground state band in ^{162}W.

The next section details the observation of new excited states in ^{163}W based upon single neutron configurations and the band structures based upon them.

Table 3.5: Measured properties of γ ray transitions assigned to ^{162}W. Energies are accurate to $\pm$0.5 keV for the strong transitions (I_γ >10%) rising to $\pm$2.0 keV for the weaker transitions.

E_γ (keV)	I_γ (%)	DCO	J_i^π	$\rightarrow$	J_f^π	Band
450.0	100.0(20)		(2^+)	$\rightarrow$	0^+	1
562.6	88.3(17)		(4^+)	$\rightarrow$	(2^+)	1
626.2	59.6(17)		(6^+)	$\rightarrow$	(4^+)	1
628.8	45.3(53)		(8^+)	$\rightarrow$	(6^+)	1
555.7	42.2(18)		(10^+)	$\rightarrow$	(8^+)	1
618.4	12.5(18)		(12^+)	$\rightarrow$	(10^+)	1
679.4	2.2(26)		(14^+)	$\rightarrow$	(12^+)	1
729.3	1.9(34)		(16^+)	$\rightarrow$	(14^+)	1

3.4 The odd-N isotope ^{163}W (N=89)

The first observation of excited states in ^{163}W was made by Dracoulis *et al.*, who observed a collective band assumed to be based upon a $13/2^+$ state [Drac92]. This configuration corresponds to placing the odd neutron into the lowest-energy $i_{13/2}$ state. In the present work, analysis of the recoil-tagged $\gamma\gamma\gamma$ cube (see section 3.2.1) revealed five additional band structures. Furthermore, the decay path from the isomeric $13/2^+$ state has been established for the first time using isomer-decay correlation techniques.

3.4.1 Decay of the $13/2^+$ isomer.

In the work of Dracoulis *et al.*, the yrast band in ^{163}W was assigned to feed an isomeric $13/2^+$ state. In the present analysis it has been possible to search for

isomer-delayed γ-ray transitions that survive the flight time through the RITU separator ($\sim 1\mu$s) using the GREAT focal plane spectrometer. The GREAT planar detector is ideal for searching for low energy ($E_\gamma < 200$ keV) γ rays and X-rays, while higher-energy γ rays could be detected in the focal plane segmented clover array comprising the GREAT and VEGA clover detectors. Figure 3.12 shows γ rays detected in the planar and clover detectors within 1 μs of a recoil implantation in the GREAT DSSD. Figure 3.12(a) shows γ rays detected in the GREAT planar germanium detector. Transitions at 38, 102, 377 and 441 keV are apparent in the spectrum. The latter three transitions are also observed under the same correlation conditions in the focal plane clover array, see Fig. 3.12(b). The 38 keV transition is not observed in Fig. 3.12(b) due to the lower detection efficiency of the clover detectors for low-energy γ rays. In order to determine which, if any, of these γ rays originates from the decay of the $13/2^+$ isomer each γ ray detected at the focal plane was used as a selective 'tag' on γ rays detected in JUROGAM at the target position. Figure 3.13 shows that the yrast band of ^{163}W is selected unambiguously in isomer-decay correlations using the 377 keV and 441 keV transitions detected in the clover array. Similar correlations reveal the 38 keV and 102 keV transitions also form part of the isomer decay path. Therefore all four γ rays are associated with an isomer decay in ^{163}W. The relative ordering of excited states in the decay path from the isomer was fixed by analysing coincidences between isomer delayed γ rays and conversion electrons detected in the GREAT PIN diodes. Figure 3.14 shows typical coincidence spectra from this analysis. Figure 3.14(a) and 3.14(b) provides evidence for two parallel decay paths from the isomeric state: one branch comprises the 38 keV and 441 keV transitions; the other branch is a cascade of the 102 keV and 377 keV transitions. The 102 keV and 441 keV γ-ray transitions are also observed in spectra obtained at the target position. The absence of the 377 keV and 38 keV γ rays detected in the JUROGAM spectrometer indicates that these transitions decay from the $13/2^+$

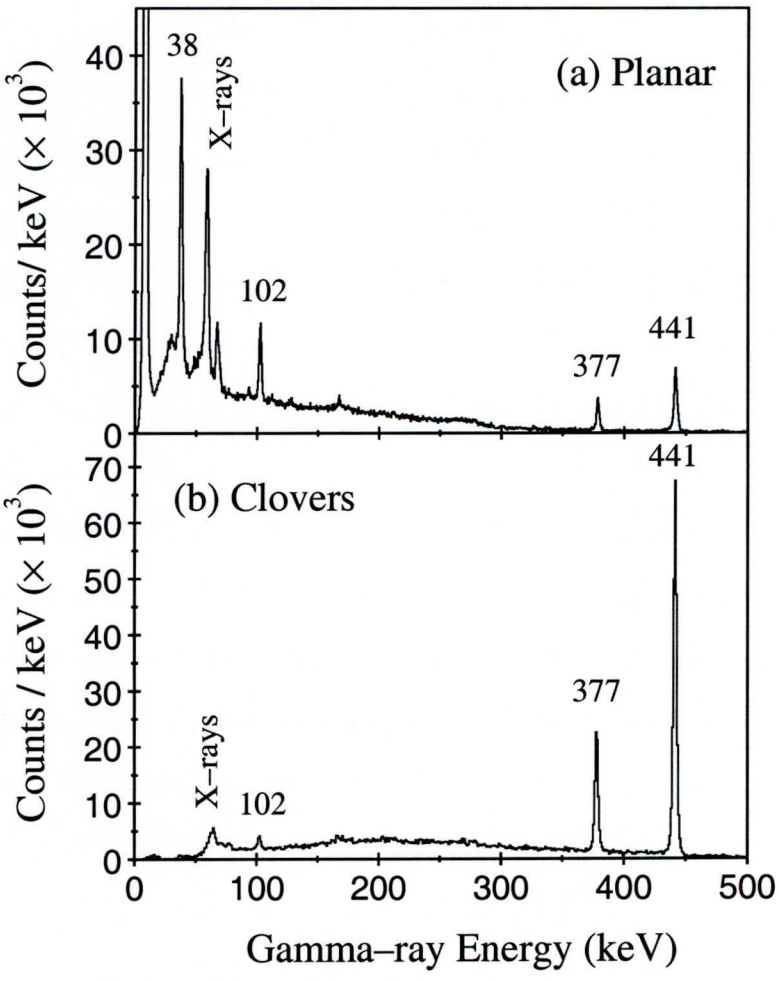

Figure 3.12: Isomer-delayed γ rays detected at the focal plane within 1 μs of detecting a recoil implantation within the GREAT double-sided silicon strip detectors. (a) Gamma rays satisfying this condition in the GREAT planar germanium detector. (b) Gamma rays satisfying this condition in the focal plance clover array.

isomer directly. If these branches constitute the decay path from the isomer to the ground state, the coincidences in Fig. 3.14 fix the excitation energy of the isomer at 479 keV. The multipolarities of γ-ray transitions depopulating the isomer can be extracted from the measured K/L conversion electron intensity ratios using the coincidence spectra displayed in Fig. 3.14(a) and 3.14(b). The ratios are compared with the ratio of internal conversion coefficients (α_K/α_L) calculated

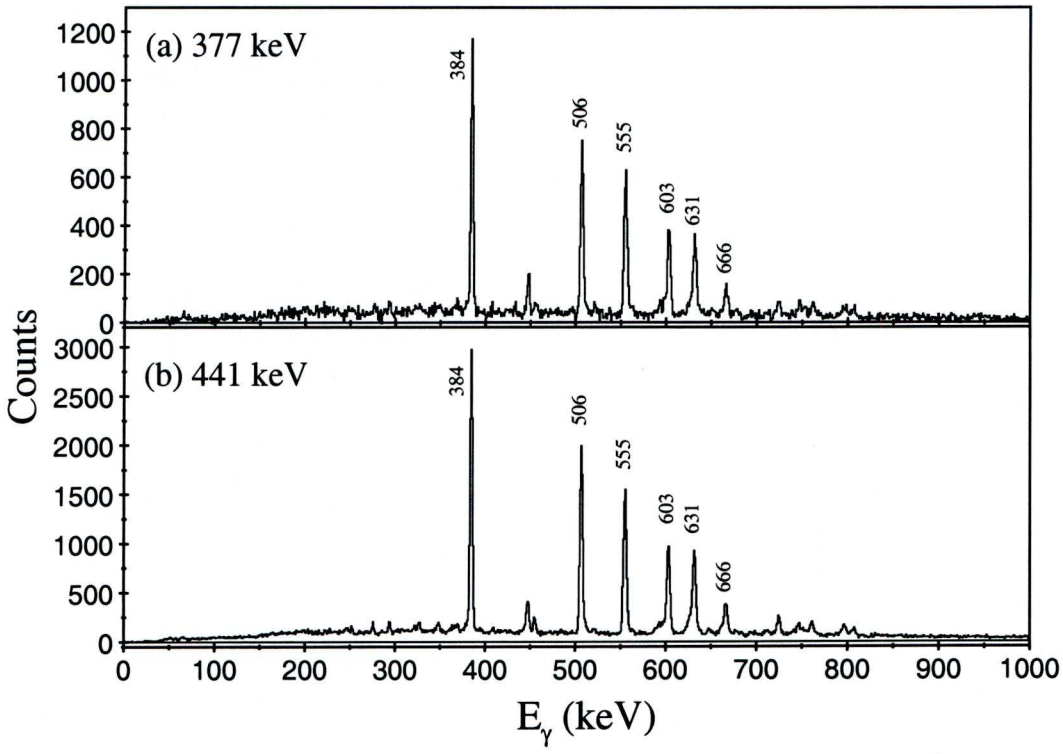

Figure 3.13: Gamma rays detected at the target position with the JUROGAM spectrometer and tagged by specific isomer-delayed γ rays detected in the focal plane clover array. (a) Prompt γ rays correlated with the 377 keV transition at the focal plane. (b) Prompt γ rays correlated with the 441 keV transition at the focal plane. The yrast band in ^{163}W clearly dominates both spectra.

using the BrIcc code [Kib08] in Fig. 3.14(c). The comparison suggest M2 and E2 multipolarities for the 377 keV and 441 keV transitions, respectively.

Decay curves were extracted from the time differences between recoil implantations in the GREAT DSSDs and the 102 keV, 377 keV and 441 keV γ rays detected in the focal plane clover detectors. Figure 3.15 shows the measured decay curves and fitted half-lives for the 377 keV, 442 keV and 102 keV transitions. The decay curves for the 377 keV and 441 keV transitions yield consistent values. From these two decay curves the error weighted average half-life for the isomer was measured to be $t_{1/2}$=149.8(5) ns. The decay curve from time differ-

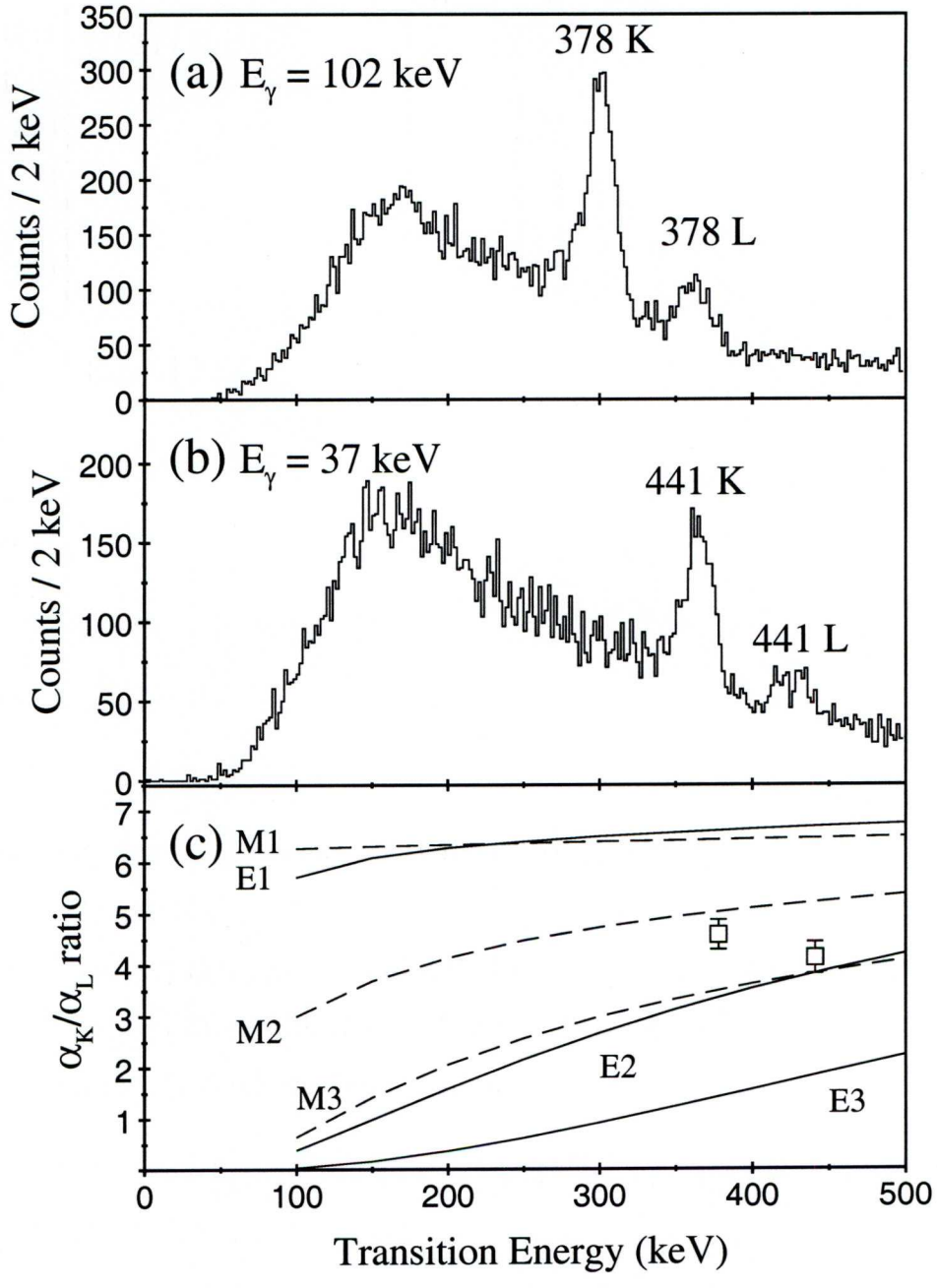

Figure 3.14: (a) Conversion electrons detected at the focal plane in prompt coincidence with (a) the 102 keV and (b) the 37 keV γ-ray transition detected in GREAT planar detector. (c) Comparison of the measured K/L conversion electron intensity ratios using the coincidence spectra displayed in (a) and (b) with α_K/α_L ratios for different multipolarities calculated using the BrIcc code [Kib08].

Table 3.6: Weisskopf estimates for the lifetimes of γ rays observed in the decay of the $13/2^+$ isomer in ^{163}W.

E_γ (keV)	$t_{1/2}$(E1) (ns)	$t_{1/2}$(M1) (ns)	$t_{1/2}$(E2) (ns)	$t_{1/2}$(M2) (ns)	$t_{1/2}$(E3) (ns)	$t_{1/2}$(M3) (ns)
38	6.1×10^{-3}	3.3×10^{-1}	1.9×10^{5}	1.2×10^{7}	9.7×10^{12}	6.1×10^{14}
102	3.2×10^{-4}	1.7×10^{-3}	1.4×10^{3}	8.7×10^{4}	9.6×10^{9}	6.1×10^{11}
377	6.3×10^{-6}	3.3×10^{-4}	2.0	125.7	1.0×10^{6}	6.5×10^{7}
441	3.9×10^{-6}	2.1×10^{-4}	0.9	57.4	3.4×10^{5}	2.2×10^{7}

ences between a recoil implantation and the detection of a 102 keV transition is much longer at $t_{1/2}$=208.7(40) ns. This discrepancy is likely to arise from much slower charge collection times for charge carriers in the clover detectors due to the shallower interaction position for the lower energy γ ray.

Weisskopf estimates for the measured transition energies of γ rays depopulating the isomer, assuming different multipolarities, are displayed in Table 3.6. The Weisskopf estimates yield half-lives of 1.7 ps for 102 keV M1 transitions, 125.7 ns for 377 keV M2 transitions and 0.9 ns for 441 keV E2 transitions. These estimates support an M2 assignment for the 377 keV transition. Weisskopf estimates for the 38 keV transition in the parallel decay path yield 6.1 ps for a E1 transition, 441 ns for an E1 transition (assuming a 10^5 hindrance) and lifetimes orders of magnitude longer for higher order multipolarities. Thus, the 38 keV transition is most likely to have an E1 character and is assigned to decay directly from the isomer parallel to the 378 keV transition.

The branching ratios for the 38 keV and 377 keV transitions were measured to be 29% and 71%, yielding partial half-lives of 516.6ns and 211.0ns respectively.

Assuming that the isomer is based on the $i_{13/2}$ neutron configuration, the measured multipolarities and Weisskopf estimates fix the ordering of transitions

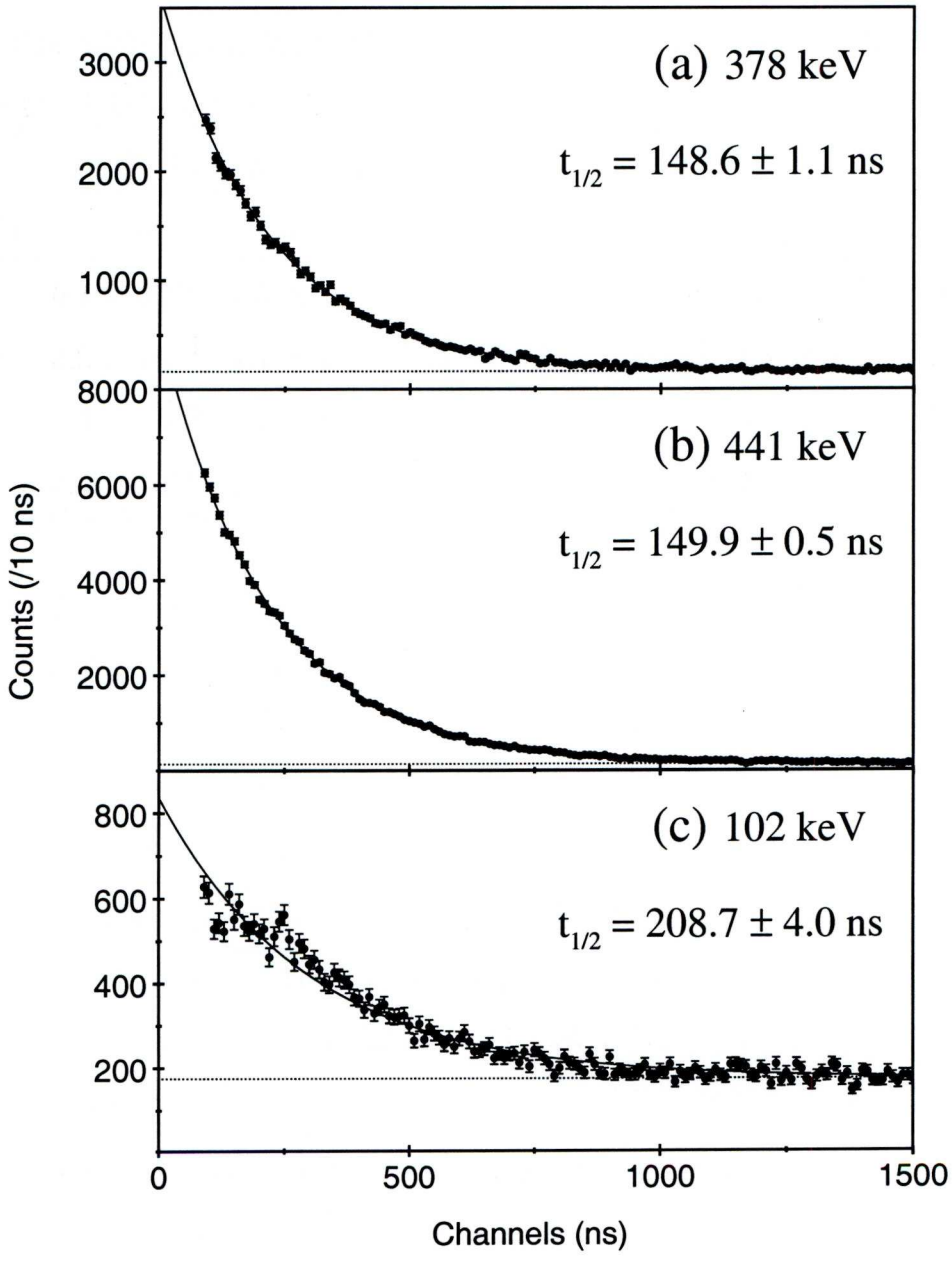

Figure 3.15: Decay curves extracted from the time differences between recoil implantations in the GREAT DSSDs and (a) the 377 keV, (b) 441 keV and (c) 102 keV γ rays in the isomer decay path measured in the focal plane clover detectors. The fitted background and the resulting half-life are indicated in each case.

in the decay paths to ground state. The level scheme for ^{163}W is displayed in Fig. 3.16 and fixes the excitation energy of the $13/2^+$ isomer at 479 keV above

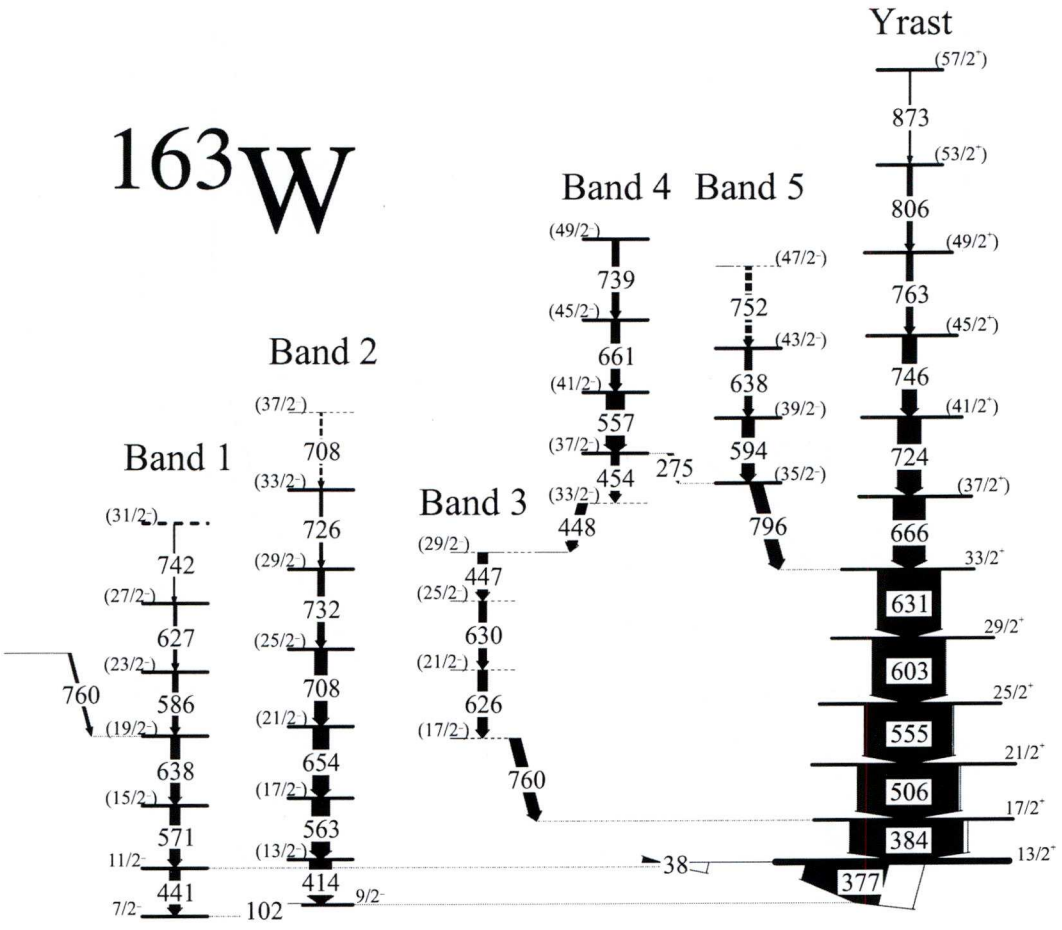

Figure 3.16: Level scheme deduced for ^{163}W. The transition energies are given in keV and their relative intensities are proportional to the widths of the arrows. The yrast bandhead has been assigned as $13/2^+$ from systematics.

the $7/2^-$ ground state in ^{163}W for the first time.

3.4.2 The yrast band and linked structures

The yrast band, first observed by Dracoulis *et al.* was extended by two transitions up to a tentative spin ad parity of $(49/2^+)$ [Drac92]. Figure 3.17(a) shows a sum of triple-gated spectra highlighting transitions in the yrast band. In the present work it has been possible to establish three new bands above the $13/2^+$ isomer. The deduced level scheme for ^{163}W is displayed in Fig. 3.16 and the properties of

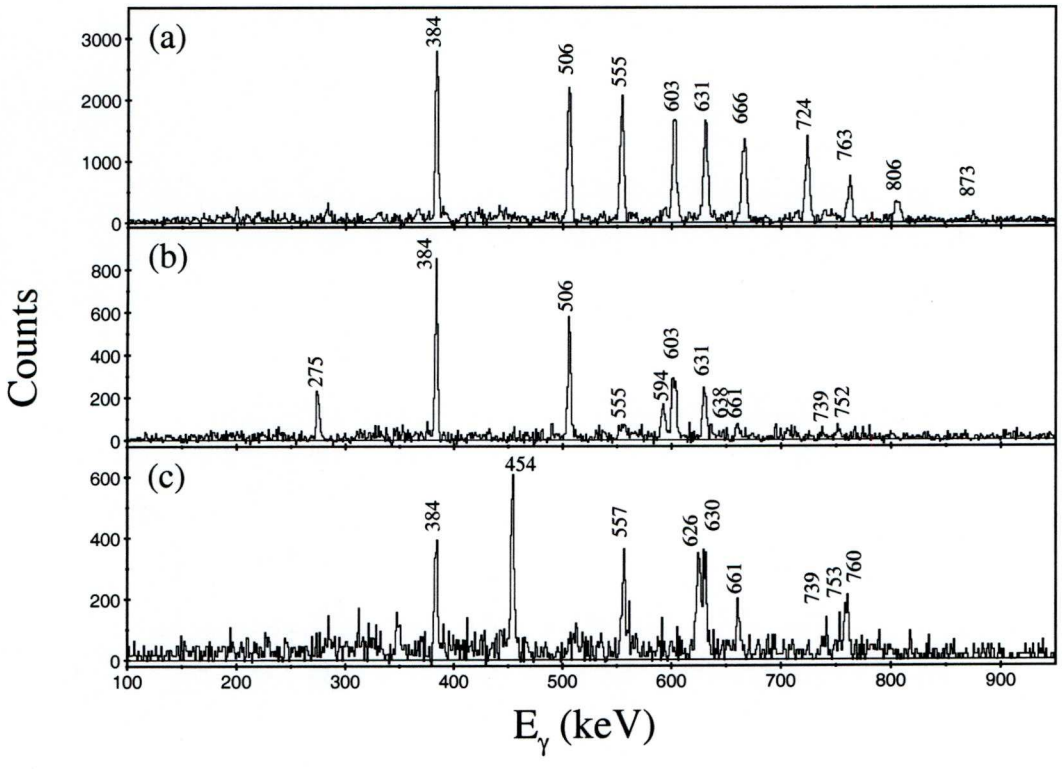

Figure 3.17: (a) Double-gated γ-ray spectrum generated by summing coincidences between the 746 keV transition and a list of transitions comprising the 384, 506, 555, 603, 631, 666 and 724 keV transitions. (b) Spectrum showing γ rays in coincidence with the 555 keV and 796 keV transitions showing transitions in bands feeding the yrast band. (c) Spectrum showing γ rays in coincidence with the self-coincident 447.5 keV doublet showing a parallel decay path from band 4 to the low spin states of the yrast band.

γ rays in the yrast and newly observed bands are recorded later in Table 3.7.

Gamma-ray coincidences reveal the presence of a 796 keV γ ray that feeds the $(33/2^+)$ yrast state. Meaningful DCO ratio could not be extracted for the 796 keV γ ray. It is assumed that this transition is an E1 transition connecting the yrast band to a negative parity structure as observed in the heavier odd-N isotopes [Simp92, Th92b]. Figure 3.17(b) shows γ rays in coincidence with the 796 keV and 555 keV transitions. In addition to the lower yrast transitions,

Table 3.7: Measured properties of γ ray transitions assigned to ^{163}W. Energies are accurate to $\pm$0.5 keV for the strong transitions (I_γ >10%) rising to $\pm$2.0 keV for the weaker transitions.

E_γ (keV)	I_γ (%)	DCO	J_i^π	$\rightarrow$	J_f^π	Multipolarity	Band
38.5	29.0(6)		$13/2^+$	$\rightarrow$	$11/2^-$	E1	Yrast $\rightarrow$ 1
101.9	1.5(6)		$9/2^-$	$\rightarrow$	$7/2^-$	M1	2 $\rightarrow$ 1
275.1	4.0(5)		$(37/2^-)$	$\rightarrow$	$(35/2^-)$		4 $\rightarrow$ 5
377.1	71.0(6)		$13/2^+$	$\rightarrow$	$9/2^-$	M2	Yrast $\rightarrow$ 2
384.1	100.0(6)	0.79(12)	$17/2^+$	$\rightarrow$	$13/2^+$	E2	Yrast
414.2	19(5)		$13/2^-$	$\rightarrow$	$9/2^-$	E2	1
440.5	10(26)		$11/2^-$	$\rightarrow$	$7/2^-$	E2	2
446.5	8.9(12)		$(29/2^-)$	$\rightarrow$	$(25/2^-)$		3
448.4	8.0(10)		$(33/2^-)$	$\rightarrow$	$(29/2^-)$		3
454.3	7.3(8)		$(37/2^-)$	$\rightarrow$	$(33/2^-)$		3
506.2	89(9)	1.00(13)	$21/2^+$	$\rightarrow$	$17/2^+$	E2	Yrast
554.6	77(7)	1.07(12)	$25/2^+$	$\rightarrow$	$21/2^+$	E2	Yrast
556.7	16.3(18)		$(41/2^-)$	$\rightarrow$	$(37/2^-)$		4
563.3	15.9(23)		$(17/2^-)$	$\rightarrow$	$(13/2^-)$		2
571.4	9.2(16)		$(15/2^-)$	$\rightarrow$	$(11/2^-)$		1
585.6	5.2(9)		$(23/2^-)$	$\rightarrow$	$(19/2^-)$		1
594.1	10.8(13)		$(39/2^-)$	$\rightarrow$	$(35/2^-)$		5
602.8	64(6)	1.19(13)	$29/2^+$	$\rightarrow$	$25/2^+$	E2	Yrast
625.6	9.0(17)		$(21/2^-)$	$\rightarrow$	$(17/2^-)$		3
627.1	4.6(14)		$(27/2^-)$	$\rightarrow$	$(23/2^-)$		1

E_γ (keV)	I_γ (%)	DCO	J_i^π	$\rightarrow$	J_f^π	Multipolarity	Band
630.4	7.1(15)		$(25/2^-)$	$\rightarrow$	$(21/2^-)$		3
631.1	55(5)	1.17(17)	$33/2^+$	$\rightarrow$	$29/2^+$	E2	Yrast
637.6	8.2(13)		$(19/2^-)$	$\rightarrow$	$(15/2^-)$		1
637.6	6.3(9)		$(43/2^-)$	$\rightarrow$	$(39/2^-)$		5
654.3	14.4(20)		$(21/2^-)$	$\rightarrow$	$(17/2^-)$		2
661.2	7.8(10)		$(45/2^-)$	$\rightarrow$	$(41/2^-)$		4
666.3	28(3)		$(37/2^+)$	$\rightarrow$	$(33/2^+)$		Yrast
708.0[a]	13.0(15)						2
724.2	20.6(21)		$(41/2^+)$	$\rightarrow$	$(37/2^+)$		Yrast
725.8	2.7(8)		$(33/2^-)$	$\rightarrow$	$(29/2^-)$		2
732.0	6.0(9)		$(29/2^-)$	$\rightarrow$	$(25/2^-)$		2
739.3	6.2(9)		$(49/2^-)$	$\rightarrow$	$(45/2^-)$		4
742.3	0.9(5)		$(31/2^-)$	$\rightarrow$	$(27/2^-)$		1
746.3	12.5(14)		$(45/2^+)$	$\rightarrow$	$(41/2^+)$		Yrast
752.5	5.5(8)		$(47/2^-)$	$\rightarrow$	$(43/2^-)$		5
759.9	10.3(22)		$(19/2^-)$	$\rightarrow$	$(17/2^+)$		3$\rightarrow$ Yrast
760.3	2.6(8)			$\rightarrow$	$(19/2^-)$		
762.8	5.9(9)		$(49/2^+)$	$\rightarrow$	$(45/2^+)$		Yrast
796.0	11.5(14)		$(35/2^-)$	$\rightarrow$	$(33/2^+)$		5 $\rightarrow$ Yrast
806.1	4.8(7)		$(53/2^+)$	$\rightarrow$	$(49/2^+)$		Yrast
872.5	1.1(4)		$(57/2^+)$	$\rightarrow$	$(53/2^+)$		Yrast

[a]Self-coincident doublet.

several new transitions are observed. The 796 keV γ ray appears to link a band structure, Band 5, comprising the 594, 638 and (752) keV transitions to the yrast band. Coincidence relations reveal that the 275 keV γ ray seen in Figure 3.17(b) is a linking transition to a parallel decay sequence labelled as Band 4 in Fig. 3.16. A DCO ratio could not be obtained for this transition. It is assumed that 275 keV γ ray is a dipole transition and and has M1 multipolarity to give Band 4 negative parity.

The isomer-decay tagged γ rays transitions in Fig. 3.13 show that a significant γ-ray peak is apparent at $\sim$447 keV. This peak is a self-coincident doublet and Fig. 3.17(c) shows all γ rays in coincident with both components. The 447.5 keV doublet forms part of an alternative decay path to the $17/2^+$ yrast state, Band 3. Band 3 comprises the 447/448 keV doublet, 454, 626, 630 and 760 keV transitions. Since the 630 keV and 760 keV γ rays have similar energies to the 631 keV and 763 keV yrast transitions it was not possible to order the transitions on the basis of relative intensities with any confidence. Consequently, Band 3 is indicated by tentative (dotted) levels in Fig. 3.16.

3.4.3 The ground state band and first excited band

The γ rays identified in the decay of the $13/2^+$ isomer identified the 441 keV and 102 keV transitions that feed the ground state. The 441 keV γ ray is assigned an E2 multipolarity on the basis of conversion electron measurements reported in section 3.4.1. The 441 keV γ ray is assumed to be the first transition of a band built on the $7/2^-$ ground state. Figure 3.18 shows typical triple coincidence spectra generated from the recoil-gated cube highlighting transitions in Band 1. The coincidence analysis reveals a collective band, labelled Band 1 in Fig. 3.16, extending to a tentative spin and parity $(31/2^-)$. Band 1 is weakly populated compared to the other bands and meaningful angular correlations could not be

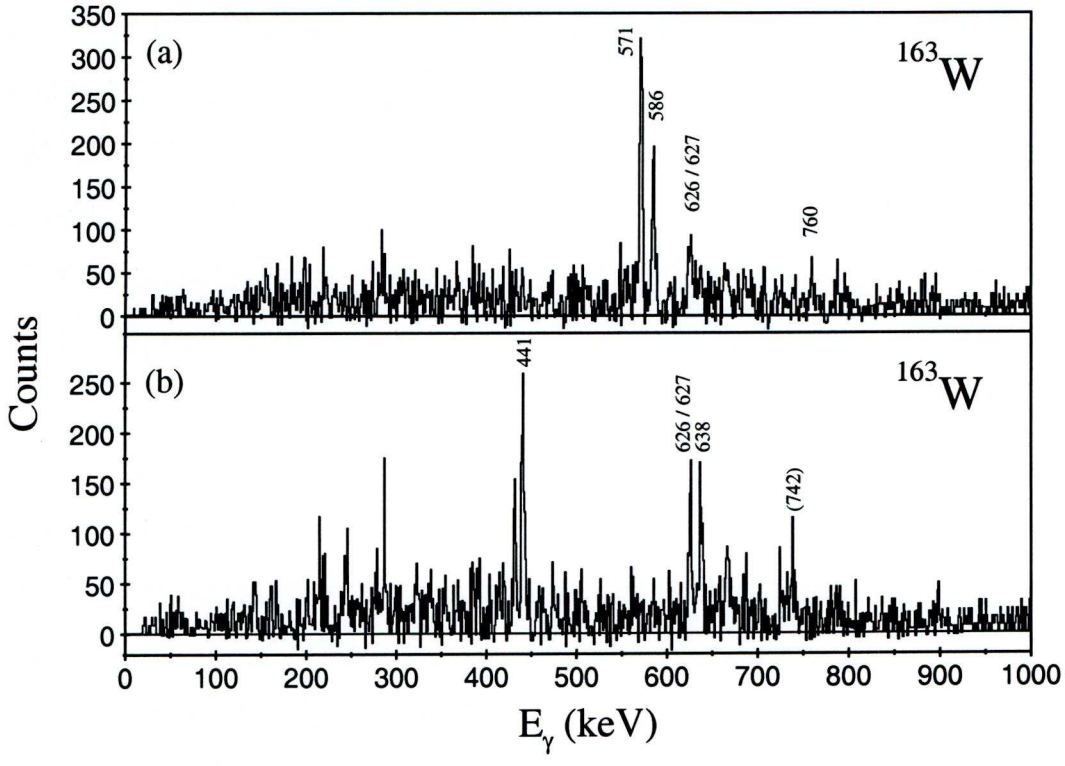

Figure 3.18: (a) Gamma-ray spectrum showing γ rays in coincidence with the 441 keV and 638 keV transitions in Band 1. (b) Spectrum showing γ rays in coincidence with the 571 and 586 keV transitions.

extracted.

The 102 keV transition was identified as part of the decay path from the $13/2^+$ isomer and constitutes the link between the ground and first excited state. The transition multipolarity is limited to M1 by the conversion electron measurements reported in section 3.4.1. Gamma-ray coincidences with the 102 keV γ ray reveal another regular cascade, Band 2 extending to a tentative spin and parity $(37/2^-)$. Figure 3.19 shows typical triple coincidence spectra from the JUROGAM spectrometer generated from the recoil-gated cube. There are no inter-band linking transitions between Bands 1 and 2. Moreover no linking transitions were observed between these bands and the bands feeding the $13/2^+$ isomer.

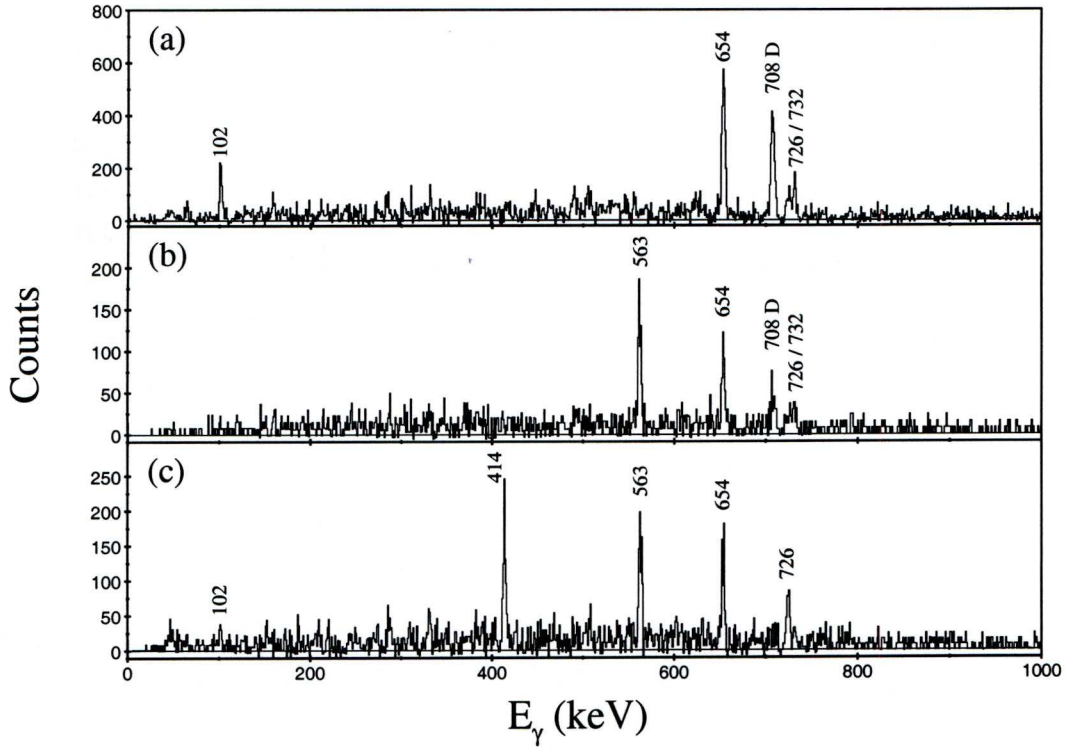

Figure 3.19: (a) Gamma-ray spectrum showing γ rays in coincidence with the 414 keV and 563 keV transitions in Band 2. (b) Spectrum showing γ rays in coincidence with the 102 and 414 keV transitions. (c) Spectrum showing γ rays in coincidence with the 708 keV and 732 keV transitions.

3.5 Discussion

The properties of the γ rays depopulating the $13/2^+$ isomer in ^{163}W outlined in the previous section fix the spins and parities of the ground state and first excited state to be $7/2^-$ and $9/2^-$, respectively. The bands based upon these states are assumed to be formed by placing the odd neutron into the low-lying negative parity states. The negative parity orbitals are strongly mixed, containing sizeable admixtures of $h_{9/2}$ and $f_{7/2}$ states. Consequently, the configuration assignments will be discussed in terms of the labels denoting parity and signature assignments defined in Table 3.4 rather than the underlying shell model labels. The configuration assignments are based on comparisons of the aligned angular momentum as

a function of rotational frequency with the predictions of the cranked shell model and the application of blocking arguments.

The representative cranked shell model calculations shown in Fig. 3.9 indicate that the negative-parity quasineutron states are lowest in energy at zero rotational frequency. The ground state spin and parity fix Band 1 to have parity and signature $(\pi, \alpha)=(-, -1/2)$ and is labelled as the E configuration. Figure. 3.9 shows that the $(-, +1/2)$ F configuration, the basis of Band 2, becomes the lowest energy negative-parity configuration with the onset of rotation. The high-j positive parity $i_{13/2}$ orbitals rapidly become the yrast configuration with increasing rotational frequency with the (+,+1/2), or A, orbital being lowest.

The yrast band in ^{163}W displays an irregular alignment pattern as a function of rotational frequency, see Fig. 3.20. The alignment for the yrast band in ^{163}W appears to show two small alignment gains; the first gain is Δi_x $\sim$6.5$\hbar$ at $\hbar\omega$ $\sim$0.30 MeV and the second is Δi_x $\sim$6$\hbar$ at $\hbar\omega$ $\sim$0.37 MeV. The alignment pattern for ^{163}W shows a marked difference to the yrast bands built on the $13/2^+$ state in the heavier odd-N isotopes ^{165}W [Simp92] and ^{167}W [Th92b].[1] In these heavier isotopes, a single rotational alignment consistent with the BC crossing is observed. Figure 3.20 compares the alignments of Bands 1 and 2 with that of the yrast band. Bands 1 and 2 exhibit alignments at similar rotational frequencies to those observed for the yrast band. This is indicated clearly by the experimental Routhians shown in Fig. 3.21(a). The predicted variation in the crossing frequencies of different quasiparticle alignments as a function of quadrupole deformation provides useful insights into the rotational alignments observed in the yrast and newly observed bands. The crossing frequencies for various quasiparticle alignments extracted from Woods-Saxon cranking calculations of the form

[1]It is interesting to note that there is an excited non-yrast band in ^{167}W with a similar alignment pattern to the yrast band in ^{163}W although its configuration is not assigned in reference [Th92b].

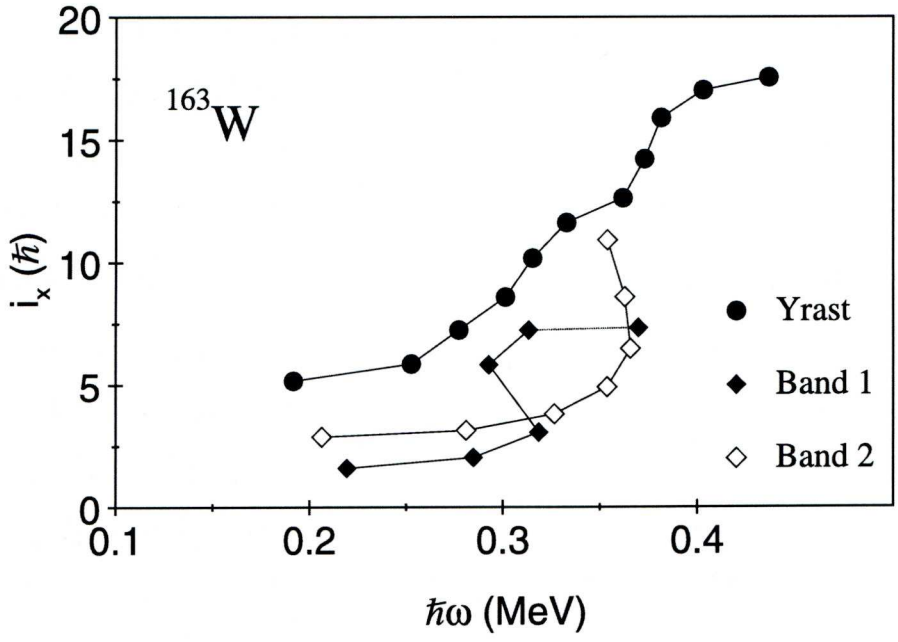

Figure 3.20: The total aligned angular momentum, i_x as a function of rotational frequency for yrast band and Bands 1 and 2 in ^{163}W. A rotational reference, based on a configuration with a variable moment of inertia defined by the Harris parameters J_0= 12.5 $\hbar^2$MeV^{-1} and J_1=60 $\hbar^4$MeV^{-3}, has been subtracted from each band.

described in Section 3.3.1, are shown in Fig. 3.21(b). The crossing frequencies for the AB and BC alignments increase with decreasing quadrupole deformation. The opposite trend occurs for the alignment of negative-parity neutrons (EF) and protons (ef). The first rotational alignment of $i_{13/2}$ neutrons, AB, is blocked for the yrast band in the odd-N isotope ^{163}W. In principle it is possible for the yrast sequence (based on the A orbital) to undergo the BC, EF or ef alignments. At the deformations predicted deformation parameters for ^{163}W it is expected that the BC alignment is much higher in frequency than either the EF or ef alignments. Figure 3.21(b) suggests that alignment gains in the yrast band are caused by the EF quasineutron alignment followed by the ab quasiproton alignment. The cranked shell model predicts alignment gains of Δi_x $\sim 6\hbar$ for the EF alignment and Δi_x $\sim 8\hbar$ for the proton ef alignment. The assignment of the EF crossing

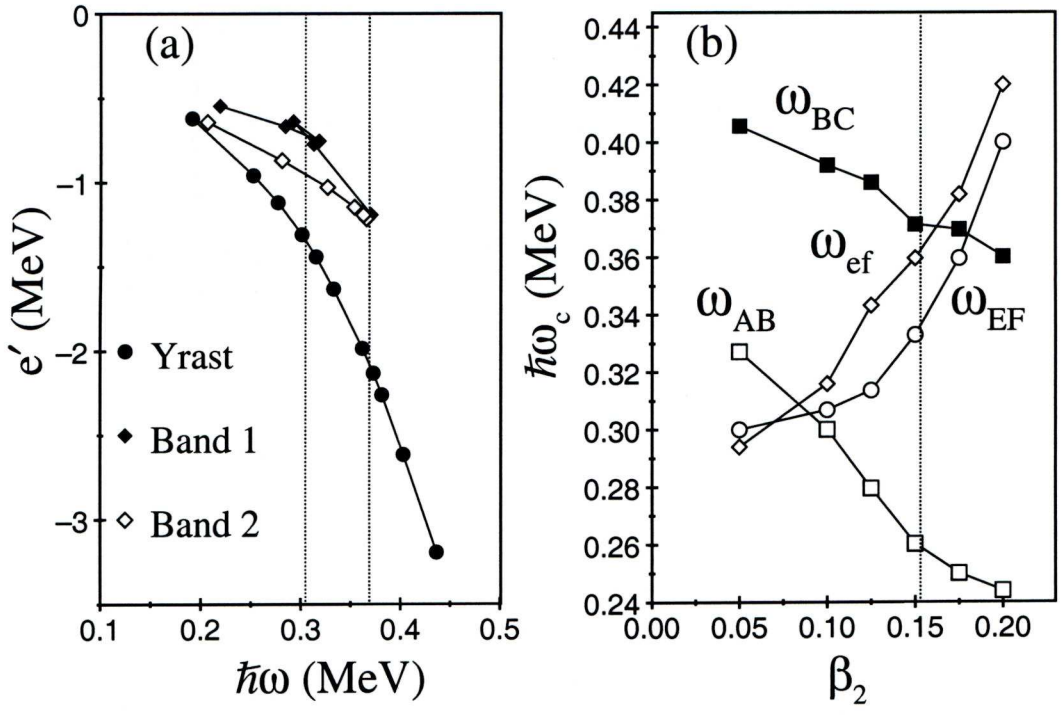

Figure 3.21: (a) Experimental Routhians extracted for the ground-state band, Band 1 and the yrast band. Dotted lines indicate the EF and ef crossing frequencies. (b) Variation of crossing frequencies $\hbar\omega_c$ for different quasiparticle alignments as a function of quadrupole deformation parameter β_2. The $\hbar\omega_c$ values are predicted at fixed deformations using Woods-Saxon cranking calculations. The dotted line indicates the deformation predicted by reference [MNK95].

as the first alignment gain in the yrast sequence of ^{163}W is consistent with the assignment of a $\nu h_{9/2}$ aligned configuration for the yrast band in the neighbouring even-N isotope ^{162}W.

The EF alignment in the yrast band cannot be responsible for the alignment gain observed for Band 1. At low spin, Band 1 is a single quasineutron E configuration implying that the EF crossing is blocked. The experimental alignment gain ($\Delta i_x \sim 5\hbar$) is too low to originate from the rotational alignment of the high-j $i_{13/2}$ orbitals. Cranking calculations indicate that this is consistent with the predicted alignment gain of $\Delta i_x \sim 4\hbar$ for the FG alignment. Figure 3.9 indicates

that the FG alignment occurs at a similar rotational frequency to that observed for the EF alignment. Thus, the aligned configuration in Band 1 is assigned as the EFG three quasineutron configuration.

The EF and FG alignments are not apparent in the alignment pattern for Band 2 indicating that these crossings are blocked. The upbending alignment observed at $\hbar\omega$ ~0.37 MeV does not flatten and prevents the total alignment gain to be measured. However, the alignment gain is greater than that observed for the rotational EF or FG alignments suggesting that the crossing originates from a high-j orbital. The possible candidates for this alignment are the AB neutron and ef proton crossings. A three quasiparticle Fef configuration may be made with the caveat that the experimental Routhians for Band 2 and the yrast band define the crossings at the same rotational frequency. Figure. 3.21(b) indicates that towards lower deformations the proton $h_{11/2}$ alignment is favoured over the neutron $i_{13/2}$ (AB) alignments. Thus, a lower deformation for Band 2 relative to the yrast configuration based on the high-j $i_{13/2}$ orbital would favour the ef quasiproton crossing.

The alignments for Band 3 have not been plotted for comparison since the level ordering could not be established with confidence. Band 3 feeds the $17/2^+$ state in the yrast band and is likely to give a low alignment. As such it is not likely to be based on a three quasiparticle configuration. Instead Band 3 is assumed to be formed by coupling the A quasineutron to an octupole vibrational phonon as observed in the side bands in the neighbouring even-N isotope, ^{164}W. The alignments for the excited sequences, Bands 4 and 5, are compared with the yrast band alignment in Fig. 3.22(a). Both bands carry a higher alignment up to $\hbar\omega$ ~0.38 MeV, leading to the assumption that these bands are based on three-quasiparticle configurations. Figure 3.22(b) compares the alignments of Bands 4 and 5 with those of the low-spin bands. Bands 4 and 5 differ in alignment from the low-spin bands of the same parity and signature by ~13$\hbar$. Assuming that

that the FG alignment occurs at a similar rotational frequency to that observed for the EF alignment. Thus, the aligned configuration in Band 1 is assigned as the EFG three quasineutron configuration.

The EF and FG alignments are not apparent in the alignment pattern for Band 2 indicating that these crossings are blocked. The upbending alignment observed at $\hbar\omega$ ~0.37 MeV does not flatten and prevents the total alignment gain to be measured. However, the alignment gain is greater than that observed for the rotational EF or FG alignments suggesting that the crossing originates from a high-j orbital. The possible candidates for this alignment are the AB neutron and ef proton crossings. A three quasiparticle Fef configuration may be made with the caveat that the experimental Routhians for Band 2 and the yrast band define the crossings at the same rotational frequency. Figure. 3.21(b) indicates that towards lower deformations the proton $h_{11/2}$ alignment is favoured over the neutron $i_{13/2}$ (AB) alignments. Thus, a lower deformation for Band 2 relative to the yrast configuration based on the high-j $i_{13/2}$ orbital would favour the ef quasiproton crossing.

The alignments for Band 3 have not been plotted for comparison since the level ordering could not be established with confidence. Band 3 feeds the $17/2^+$ state in the yrast band and is likely to give a low alignment. As such it is not likely to be based on a three quasiparticle configuration. Instead Band 3 is assumed to be formed by coupling the A quasineutron to an octupole vibrational phonon as observed in the side bands in the neighbouring even-N isotope, ^{164}W. The alignments for the excited sequences, Bands 4 and 5, are compared with the yrast band alignment in Fig. 3.22(a). Both bands carry a higher alignment up to $\hbar\omega$ ~0.38 MeV, leading to the assumption that these bands are based on three-quasiparticle configurations. Figure 3.22(b) compares the alignments of Bands 4 and 5 with those of the low-spin bands. Bands 4 and 5 differ in alignment from the low-spin bands of the same parity and signature by ~13$\hbar$. Assuming that

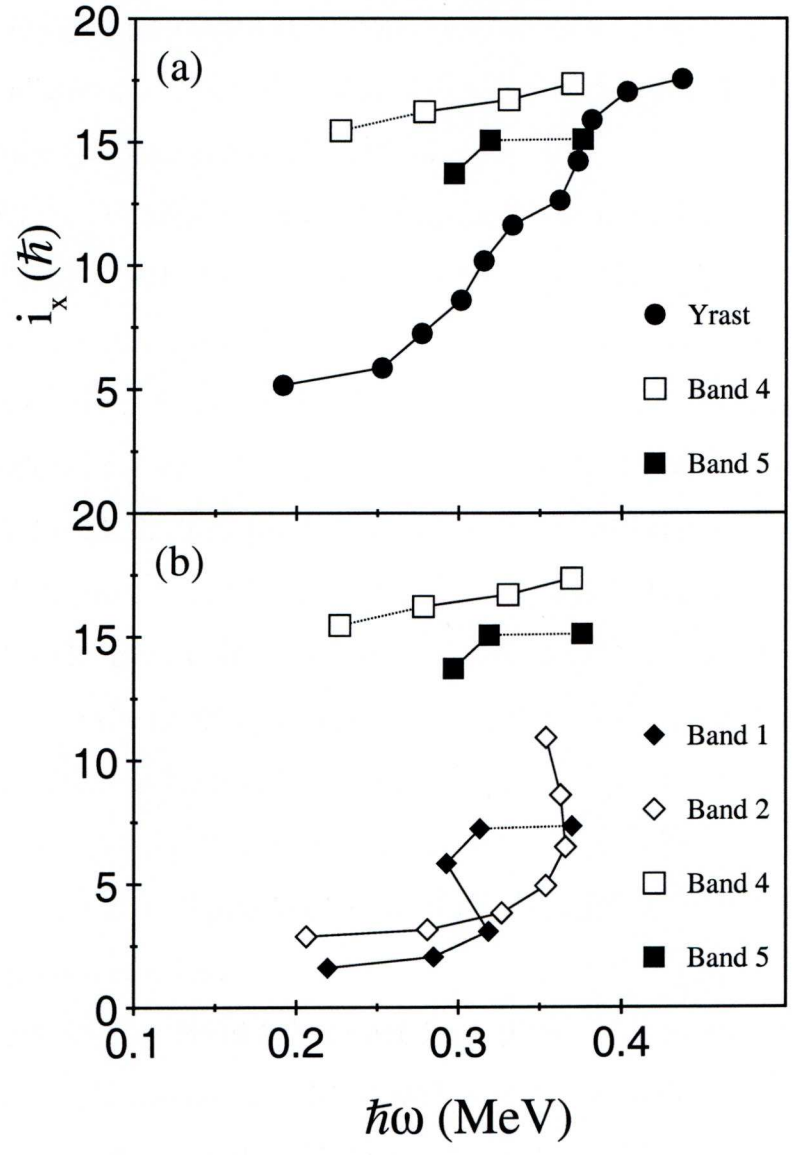

Figure 3.22: The aligned angular momentum, i_x as a function of rotational frequency for the bands in ^{163}W. A rotational reference, based on a configuration with a variable moment of inertia defined by the Harris parameters J_0= 12.5 $\hbar^2$MeV^{-1} and J_1=60 $\hbar^4$MeV^{-3}, has been subtracted from each band. (a) Comparison of i_x plots for the yrast band, Band 4 and Band 5. (b) Comparison of i_x plots for Band 1, Band 2, Band 4 and Band 5.

the 796 keV γ-ray linking transition to the yrast band is a stretched E1 and the 275 keV γ ray connecting Band 5 to Band 4 yields negative parity for Bands 4 and

5. Bands 4 and 5 could be based on the FAB and EAB configurations. However, the predicted gain achieved in the AB quasineutron alignment is predicted by the Woods-Saxon calculations to be $\Delta i_x \sim 11\hbar$. Similar discrepancies have been observed in N=94 isotones [Th92b].

3.6 Summary

The yrast band of ^{163}W, built on a $13/2^+$ isomeric state, has been extended to higher spin $(57/2^+)$. Two parallel decay paths have been determined via conversion electron-γ-ray coincidences fixing the excitation energy of the isomer to be 479 keV above the ground state. Multipolarities determined from measured K/L conversion electron ratios have fixed the ground state spin and parity as $7/2^-$. An error-weighted average value of 149.8(5) ns was measured for the isomer decay half-life.

In addition, five new bands have been observed in ^{163}W for the first time. The ground state band has been determined to a tentative spin and parity of $31/2^-$. The alignment is predicted to be based on the rotational alignment of the FG negative parity quasineutrons. The first excited band is built on the $9/2^-$ state extends to a tentative spin and parity of $37/2^-$. The alignment for this band could not be determined with confidence and could be based on the BC quasineutron or ef quasiproton alignments. Band 3 is assigned as an octupole vibrational structure that forms a decay path from Band 4 to the yrast sequence. The remaining bands, Bands 4 and 5 are assigned to be three-quasiparticle structures based on the FAB and EAB configurations, respectively. The application of blocking arguments and comparisons with cranking calculations indicate that the irregular alignment pattern of the yrast band is due to the alignment of the EF quasineutrons followed by the ef quasiprotons.

The configuration assignments and quasiparticle alignments that characterise

Table 3.7: Summary of configuration assignments for bands in ^{163}W.

Band	(π,α)	Quasiparticle alignments
Yrast	$(+,+1/2)$	A $\rightarrow$ AEF $\rightarrow$ AEFef
Band 1	$(-,-1/2)$	E $\rightarrow$ EFG
Band 2	$(-,+1/2)$	F $\rightarrow$ Fef or FBC
Band 3	$(-,+1/2)$	A $\otimes$ Octupole
Band 4	$(-,+1/2)$	FAB
Band 5	$(-,-1/2)$	EAB

the bands in ^{163}W are summarised in Table 3.7.

In addition, the level scheme for ^{164}W has been extended and the yrast sequence of ^{162}W has been confirmed using the recoil-decay tagging technique. The band structures in these three isotopes indicate a crucial change in the active aligning orbitals as the N=82 shell gap is approached.

Chapter 4

Strongly coupled bands in the odd-Z nucleus, ^{163}Ta

Excited states in the neutron-deficient nuclide ^{163}Ta were observed for the first time using the ^{106}Cd(^{60}Ni,3p)^{163}Ta* reaction in an experiment performed at the University of Jyväskylä Accelerator Laboratory. Three strongly coupled bands were observed, establishing the excitation level scheme to high spin $(61/2^-)$. Configuration assignments have been based on comparisons of the deduced aligned angular momentum as a function of rotational frequency with the predictions of the cranked shell model. The assigned configurations are also supported by the measured B(M1)/B(E2) ratios of reduced transition strengths. The yrast band is assigned to feed the $11/2^-$ state and exhibits large signature splitting at low spin. This is discussed in terms of coupling an odd proton in the [514]$9/2^-$ Nilsson orbital to a γ-soft core. The absence of signature splitting at higher spins is interpreted in terms of aligned neutron configurations. The changing structure of the Ta isotopes approaching N=82 is discussed in terms of the underlying single-particle configurations.

Chapter 4

Strongly coupled bands in the odd-Z nucleus, ^{163}Ta

Excited states in the neutron-deficient nuclide ^{163}Ta were observed for the first time using the ^{106}Cd(^{60}Ni,3p)^{163}Ta* reaction in an experiment performed at the University of Jyväskylä Accelerator Laboratory. Three strongly coupled bands were observed, establishing the excitation level scheme to high spin $(61/2^-)$. Configuration assignments have been based on comparisons of the deduced aligned angular momentum as a function of rotational frequency with the predictions of the cranked shell model. The assigned configurations are also supported by the measured B(M1)/B(E2) ratios of reduced transition strengths. The yrast band is assigned to feed the $11/2^-$ state and exhibits large signature splitting at low spin. This is discussed in terms of coupling an odd proton in the [514]$9/2^-$ Nilsson orbital to a γ-soft core. The absence of signature splitting at higher spins is interpreted in terms of aligned neutron configurations. The changing structure of the Ta isotopes approaching N=82 is discussed in terms of the underlying single-particle configurations.

4.1 Motivation

This work forms part of a wider research programme aimed at understanding the evolution of nuclear structure approaching both the proton drip line and the closed neutron shell at N=82. The recent exploitation of large γ-ray spectrometer arrays using selective techniques has revealed the yrast states in many nuclei in this region for the first time [Lag06, Se05, Joss04, Joss06a, O'Don09]. In recent years, major advances in identifying excited states and understanding the properties of the even-even nuclei from hafnium to lead have been made, yet comparatively little is known about the most neutron-deficient odd-Z nuclei in this region. For example, comprehensive information on the neutron-deficient Ta isotopes below ^{164}Ta [Roux02] is relatively sparse compared to other isotopic chains in the region and most of the available information originates from radioactive (α or proton) decay spectroscopy. However, even these data are incomplete partly due to the unfavourable decay properties for correlating radioactive decay chains.

The neutron-deficient Ta (Z = 73) isotopes occupy a transitional region of the nuclear chart where the neutron number descends from the mid-shell value at N=104 to the closed shell at N=82. Figure 4.1 shows the variation of the predicted quadrupole deformation parameter, β_2, as a function of proton and neutron number for the ground states of the N=90 isotones and Ta isotopes, respectively [MNK95]. The degree of quadrupole deformation β_2 represents the deviation away from sphericity and Fig. 4.1 clearly shows that the quadrupole deformation decreases as the Z = 82 shell closure is approached from the mid-shell at Z = 66 [MNK95] in the N=90 isotones. Furthermore, the degree of deformation for lower even-mass isotopes has also been calculated to diminish as the N = 82 is approached from the maximum value near the N = 104 mid-shell. [MNK95]. The recent measurements of yrast energy levels in the even-even Hf-W-Os-Pt isotopic chains support these predictions. For example, ratios of the

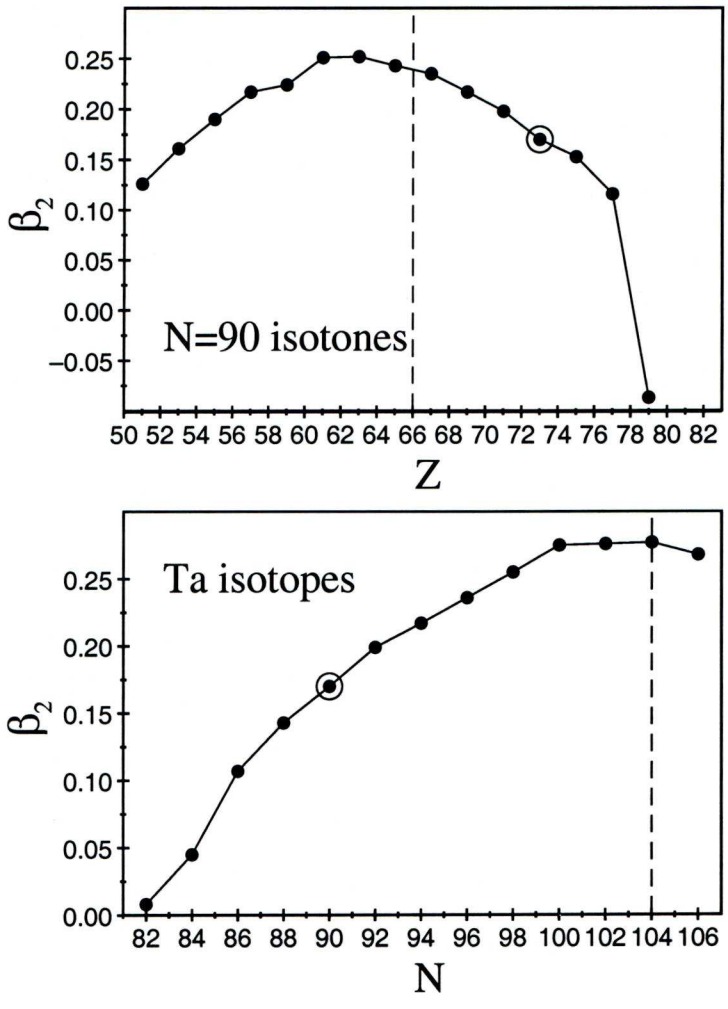

Figure 4.1: Variation of the quadrupole deformation parameter, β_2, as a function of (a) proton number, Z in the N=90 isotones; (b) neutron number, N in the Ta isotopes. The corresponding values for ^{163}Ta are indicated by circles. The dashed vertical line indicates the midshell values for protons and neutrons. The deformations parameters are taken from ref [MNK95] and assume $\gamma = 0°$.

$E(4^+)/E(2^+)$ excitation energies highlight a transition from ideal rotational characteristics observed for isotopes near the neutron mid-shell towards vibrational excitations near N=82 (see previous Chapter).

The evolution of quadrupole deformation has dramatic consequences for the relative excitation energies of single-particle orbits. This can be seen in Fig. 3.2

which shows how the degeneracy of the spherical shell model states is relieved as a function of deformation. The relative positions of the orbitals in close proximity to the Fermi surface dictate the properties of the yrast states.

For the odd-Z Ta nuclei, the proton Fermi level lies near the top of the $\pi h_{11/2}$ subshell, see Fig 3.2(a). Indeed, for the even-N $A \geq 164$ isotopes, the ground state is based on a proton occupying the high-Ω $[514]9/2^-$ ($h_{11/2}$) state. The Ta isotopes may also have configurations where the odd proton occupies orbitals originating from the positive-parity $g_{7/2}$ subshell. For the neutron-deficient Ta isotopes, the neutron Fermi surface will occupy a region where the active orbitals will originate from the $f_{7/2}$, $h_{9/2}$ or $i_{13/2}$ subshells. This scenario where the proton and neutron Fermi surfaces lie at the top (high-Ω orbitals) or bottom (low-Ω orbitals) of their respective shells presents the ideal conditions for γ soft or triaxial nuclear shapes. Such 'soft' nuclei are sensitive to the occupation of core-polarising orbitals at the Fermi surface. For example, the high-j, low-Ω $i_{13/2}$ neutrons have prolate core-polarising tendancies and provide a dominant influence on yrast states for many neutron-deficient nuclei in this region. Figure 3.2 indicates an interesting situation as neutrons are successively removed towards the N=82 closed shell. At N=90, the neutron Fermi surface may lie below the lowest Ω $i_{13/2}$ state and towards lower deformations (lower N) this orbital will achieve higher excitation energy above the Fermi surface allowing the negative parity $f_{7/2}/h_{9/2}$ states to form the yrast spectrum. Some evidence for the ascendancy of the $\nu h_{9/2}$ orbital has been found in the even-even isotopic chains (see previous Chapter and references [Joss04, Joss06a]). However, little is known about these changes in the nearby odd-Z isotopes. The transitional nucleus ^{163}Ta is predicted to have a ground state deformation ($\varepsilon_2 = 0.158$[1] or $\beta_2 = 0.170$ [MNK95]) that would allow not only the interplay of the $\nu i_{13/2}$ and $\nu h_{9/2}$ orbitals to be elucidated, but also highlight the core-polarising role of the odd-proton. This work reports the first

[1]For relatively small deformations ε_2 and β_2 can be related via $\varepsilon_2 \approx \beta_2(1 - 0.1126\beta_2)$.

observation of excited states in ^{163}Ta and discusses the deduced configurations in the context of the evolving nuclear structure towards the N=82 shell closure.

4.2 Previous studies of the $A < 165$ Ta isotopes

Tantalum isotopes have been identified down to the closed neutron shell at N=82 following the recent measurement of the spherical proton emitter, ^{155}Ta [Page07]. Comparisons with WKB barrier penetration models have determined the proton emission to proceed from an $h_{11/2}$ isomeric state rather than the $s_{1/2}$ states measured from radioactive decay spectroscopy for the heavier isotopes. While some progress has been made through decay measurements, the decay properties of the whole isotopic chain are incomplete and, until recently, little was known about the excited states or high-spin structures of the Ta isotopes below ^{164}Ta [Roux02]. The principal reason is because γ-ray spectroscopy is extremely challenging near the proton drip line. The main obstacles are low production cross sections in fusion-evaporation reactions which decrease rapidly towards the proton drip line and the high γ-ray backgrounds due to fission and stronger reaction channels. The application of the recoil-decay tagging technique has led to the identification of excited states in ^{157}Ta [Se05] and ^{159}Ta [Keen01] and established tentatively the yrast structures up to spins of 39/2 and 23/2, respectively. These excited states are built upon an $h_{11/2}$ isomeric state and higher-spin states are formed by aligning the spins of a small number of valence nucleons. Above ^{159}Ta (N=86), the next isotope for which high-spin states have been published is the doubly odd ^{164}Ta [Roux02]. For ^{164}Ta and heavier isotopes, strongly coupled collective bands have been observed [Roux01] [Th92a] [Li93]. A parallel investigation by Lagergren *et al.*, [Lag08] has recently discovered a comprehensive level scheme for ^{161}Ta. Prior to this work no excited states were known in ^{163}Ta.

The isotope ^{163}Ta was first identified in β-decay measurements following the

^{175}Lu(^{3}He,15n) reaction with a 2μA beam current at an energy of 280 MeV [Lia85]. In this moving tape experiment, half-lives of 10.5(18) s and 11.0(10) s were deduced from time differences between implantation in the tape and the detection of β decays and β-delayed K_α X-ray transitions in ^{163}Hf. A value of 10.5(18) s was obtained from the γ-ray data and a slightly larger value of 11.0(10) s from the X-ray data. The higher value was attributed to contamination from peaks associated with ^{166}Ta.

An α-decay branch of ^{163}Ta was observed in a later study by Runte *et al.* [Run86] In that work, the α-decay energy E_α=4.63(1) MeV and half-life $t_{1/2}$ = 11.5(18) s were measured in a He-jet/tape transport experiment. Alpha-decay measurements by Hagberg *et al.*[Hag92] confirmed the earlier measurements of Runte *et al.* yielding α-decay energy, half-life and branching ratio measurements of 4.635(7) MeV, 10(2) s and 0.28(4)%, respectively. This decay was assigned to ^{163}Ta via a relative comparison between the experimental yields and those predicted using the ALICE code [Bl78].

4.3 Results

4.3.1 Assignment of γ rays to ^{163}Ta

Excited states in ^{163}Ta were populated in the ^{60}Ni + ^{106}Cd reaction via the 3p exit channel. These data were collected in the same experiment reported in the previous chapter. The high implantation rate ($\sim$ 4 kHz) in the DSSDs of the GREAT spectrometer, together with the long half-life of the α decay of ^{163}Ta ($t_{1/2}$ $\sim$11 s), create significant problems for unambiguous identification by tagging techniques. In this case, associating a particular radioactive decay to a long-lived recoil is problematic since the probability of false correlations due to multiple hits in the same DSSD pixel is greatly increased. Furthermore,

the α-decay branch is very low (b_α = 0.28(4)%). Thus, it was impossible to provide unambiguous identification using the RDT technique under the present experimental conditions.

Instead, assignments were made by considering the relative yields. Gamma rays belonging to some of the most intense reaction channels in these data were identified in prior studies using, where possible, recoil-decay tagging techniques (see previous chapter). Gamma-ray transitions in ^{163}W were populated intensely suggesting that the three-particle exit channels were likely to have the optimal yield. Calculations based on the ALICE fusion evaporation code support this experimental observation and predict ^{163}Ta to have the largest cross section. On this basis, the observation of intense 432 keV and 287 keV transitions in the recoil-gated γ-ray spectra were assigned to belong to the unknown level scheme of the $3p$ exit channel leading to ^{163}Ta. This appears to be a reasonable assignment since the yrast band is a strongly coupled band consistent with the structure expected for an odd-particle in a high-j orbital as observed for the heavier Ta isotopes. Furthermore, γ rays assigned here to ^{163}Ta were observed in A=163 mass-gated γ-ray spectra obtained in an experiment performed by Simpson *et al.* at Daresbury Laboratory [Simp09]. This experiment exploited the ^{104}Pd(^{63}Cu,xpyn) reaction at a beam energy of 285 MeV and the POLYTESSA γ-ray spectrometer used in conjunction with the Daresbury recoil separator.

4.3.2 Gamma-ray coincidence analysis

High-fold γ-ray coincidences were employed in order to select γ-ray decay paths in ^{163}Ta from the background of γ rays arising from other intense channels. The same recoil-gated cube as described in Chapter 4, Section 3.2.1 was used in this analysis.

A level scheme for ^{163}Ta was constructed using relative γ-ray intensities and

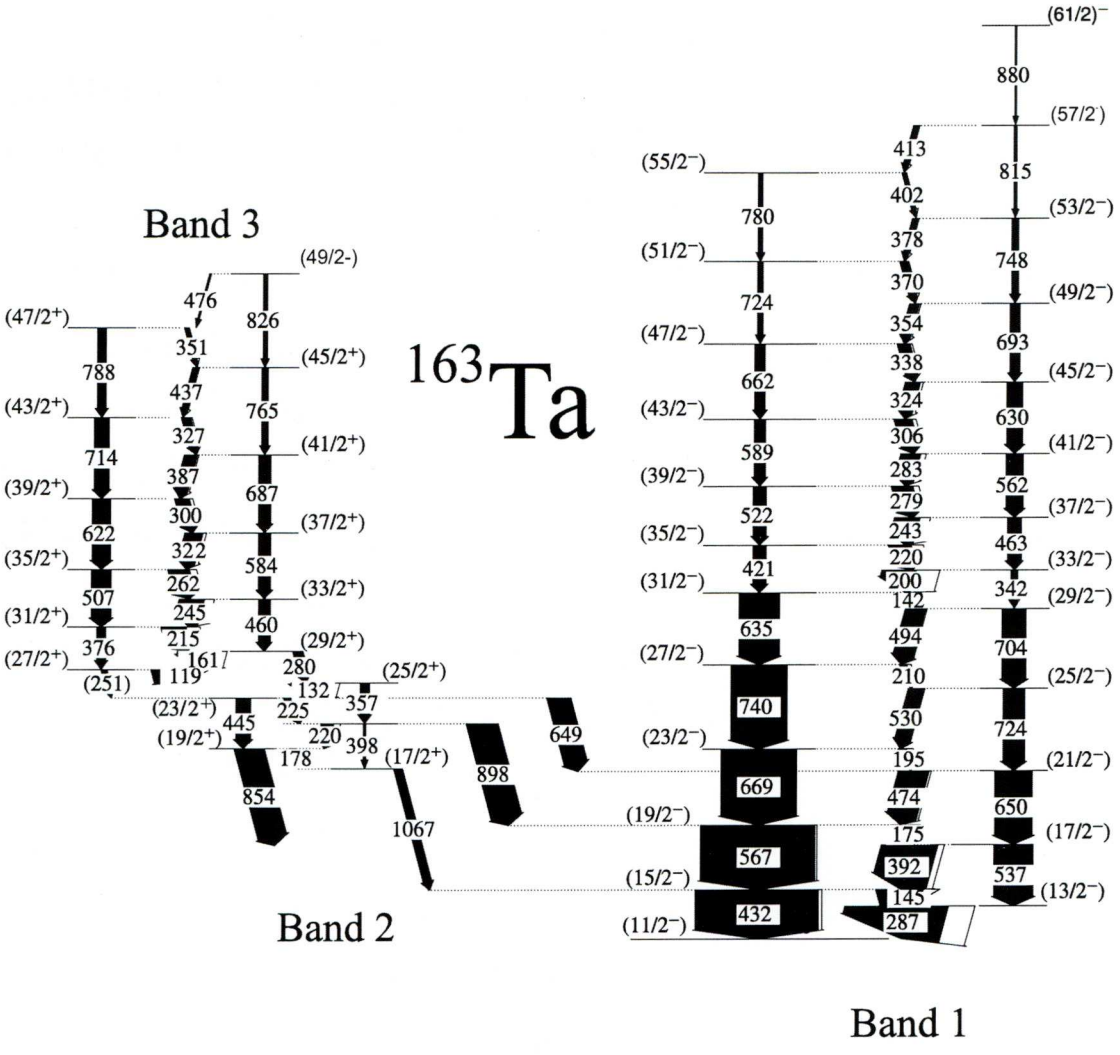

Figure 4.2: Level scheme deduced for ^{163}Ta. The transition energies are given in keV and their relative intensities are proportional to the widths of the arrows.

coincidence relationships from spectra generated from the cube. The level scheme deduced for ^{163}Ta from the present work is displayed in Fig. 4.2.

4.3.3 Band 1: The Yrast Band

The coincidence analysis established that the 432 keV and 287 keV transitions were not in coincidence with each other. However they had mutually coincident γ rays. A strongly coupled band was deduced on top of the respective transitions

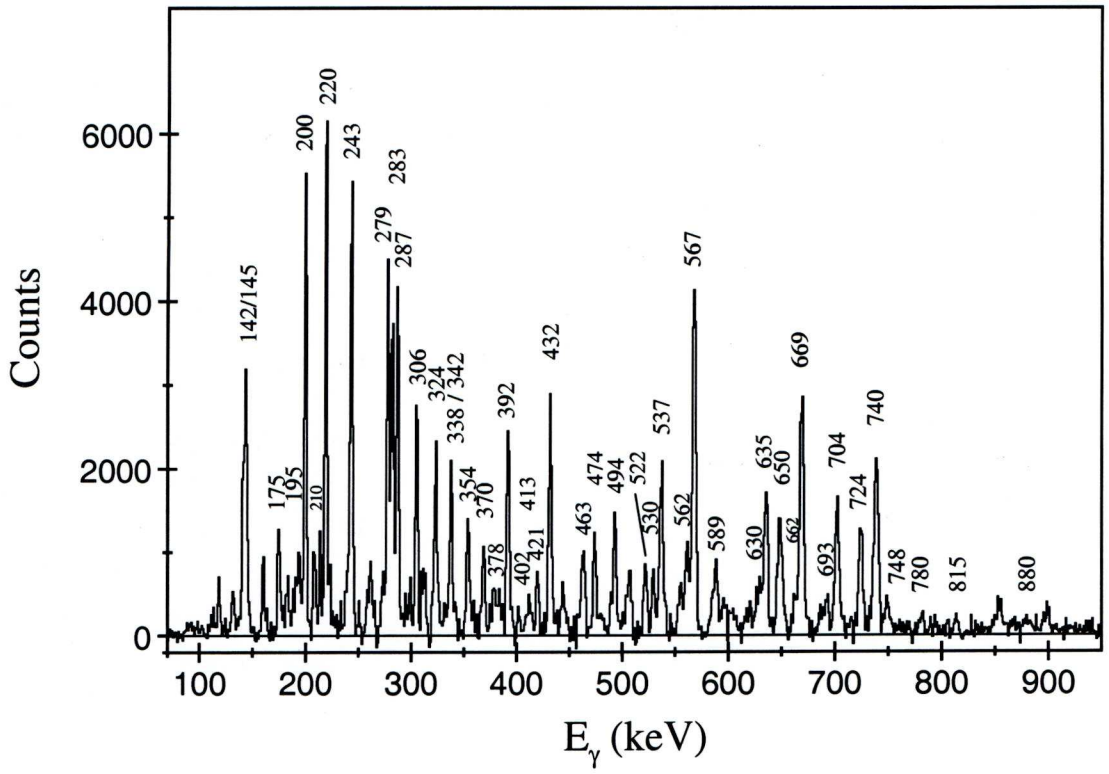

Figure 4.3: A sum of double-gated spectra showing transitions in band 1. The spectrum was generated from summing coincidences demanded between two gate lists, one comprising the 287, 144, 392, 175, 474, 195, 530 keV γ rays and the other comprising the 306, 324, 338, 354, 370, 378, 402 keV transitions. The unlabelled peaks correspond to transitions in bands 2 and 3 brought in by energy doublets in the list. This spectrum was obtained from a recoil-gated cube composed entirely of fold-three events.

where the 287 keV was an interlinking transition between two signature partner bands. Most of the measured intensity was observed in the in-band transitions up to a tentative spin and parity of $29/2^-$. At this point there appears to be a change in behaviour as the intensity is then observed predominantly in the transitions between the signature partners in the band. The yrast band extends to an excitation energy of 8.035 MeV relative to the $11/2^-$ band head and an angular momentum of 61/2. Figure 4.3 shows a γ-ray spectrum generated from the a sum of double gates selected to show transitions in Band 1.

The DCO measurements for the strongest in-band transitions suggest $\Delta I = 2$ character and so these signature partner bands are assigned to be cascades of E2 γ rays. The connecting transitions are found to have similar DCO ratios to those measured for the in-band transitions. The coincidence measurements firmly place these γ rays in the level scheme and constrain the multipolarities to have an M1 character. The measured DCO ratios imply that there must be a positive multipole mixing ratio yielding a mixed M1/E2 assignment for the $\Delta I = 1$ transitions. The sign of the the mixing ratio δ is related to the single-particle g-factors by

$$\text{sign}\left[\delta_{E2/M1}\right] = \text{sign}\left[\frac{g_K - g_R}{Q_0}\right], \tag{4.1}$$

so the mixing ratio will be positive if $g_K > g_R$ where $g_R \sim Z/A$. An odd proton in a $h_{11/2}$ orbital has a large positive g-factor that would induce positive multipole mixing ratios for the $\Delta I = 1$ transitions, which is consistent with the present measurements. The strongly coupled nature of the Band 1 also supports a configuration assignment where the odd proton occupies a high-Ω deformation aligned orbital. The most likely candidate is the $[514]9/2^-$ Nilsson state, see Fig 3.2. Therefore, the yrast band is assigned as a negative-parity odd-spin structure based on the $[514]9/2^-$ proton orbital.

For the purpose of configuration assignments, the branching ratio $\lambda_{out/in}$ of interband to in-band transitions was extracted from the cube. Double gates on the strongest transitions immediately above the state of interest were applied. The resulting spectra allowed the relevant peak areas to be fitted and the $B(M1)/B(E2)$ values extracted via the relation [BM75],

$$\frac{B(M1; I \rightarrow I-1)}{B(E2; I \rightarrow I-2)} = \frac{\lambda_{out/in}}{1.43 \times 10^4} \frac{[E_\gamma(\Delta I = 2)]^5}{[E_\gamma(\Delta I = 1)]^3} (\mu_N^2 e^{-2} \text{fm}^{-4}), \tag{4.2}$$

The properties γ rays in Band 1 are recorded for transitions from levels in each signature in Tables 4.1 and 4.2, respectively.

4.3.4 Band 2

Figure 4.4 shows a sum of double gates generated from coincidences between the 132 keV transition and the dipole transitions in Band 3 showing γ rays in Bands 2 and 3. The first excited band, Band 2, has a strongly coupled character. It is fed directly by Band 3 and decays via several linking transitions to the low-spin states of Band 1. These linking transitions have transition energies at 649 keV, 854 keV, 898 keV and 1067 keV and feed the $21/2^-$, $17/2^-$, $19/2^-$, and $15/2^-$ states in Band 1, respectively. DCO ratios of 0.69(9) and 0.54(8) were measured for the 854 keV and 898 keV γ rays, respectively, indicating that these transitions have $\Delta I = 1$ character. The lower ratio implies that there is no significant mixing from a higher multipolarity. On this basis these γ rays are assigned to have an E1 character fixing Band 2 as a negative-parity odd-spin structure.

Using γ-ray intensity ratios for the out-of-band and in-band linking transitions it has been possible to extract values for the reduced transition strength ratio $B(E1)/B(E2)$ using Equation 3.2. Assuming a quadrupole moment ($Q_0 = 4.2$ eb) derived from the predicted ground-state deformation of ^{163}Ta given in reference [MNK95] yields $B(E1)$ values of $1.9(3) \times 10^{-5}$ Wu for the 898 keV γ ray. This $B(E1)$ value indicates that Band 2 is a formed by coupling the odd proton to an octupole vibration phonon as discussed in the previous Chapter. The properties of γ-rays in Band 2 and the linking transitions to the yrast band are listed in Table 4.3.

4.3.5 Band 3

Figure 4.4 shows γ-ray transitions assigned to Band 3. The coincidence analysis reveals that Band 3 is a strongly coupled band with intense interleaving dipole transitions extending to high spin (49/2). The decay path to the low-spin yrast states (Band 1) proceeds via Band 2. The strongly coupled character of Band 3

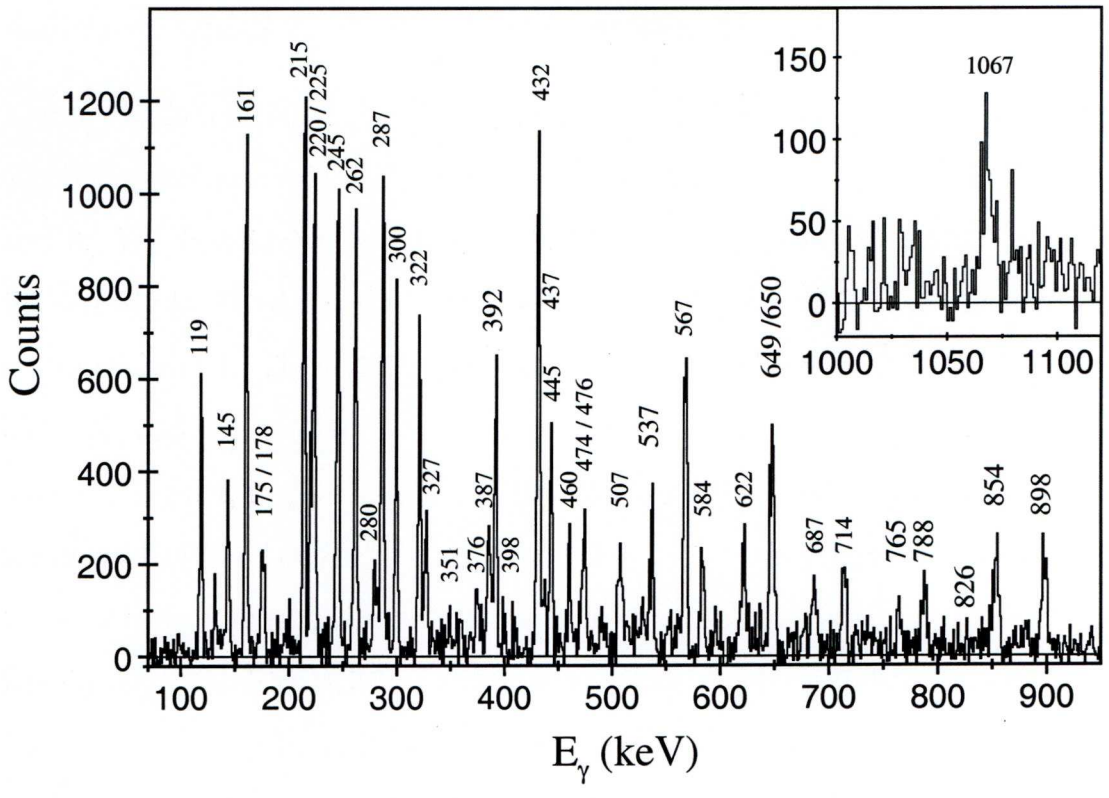

Figure 4.4: A sum of double-gated spectra showing transitions in band 3 and the decay path through band 2 to the yrast sequence. The spectrum was generated from summing coincidences demanded between the 132 keV transition and a list comprising the 119, 161, 215, 245, 262, 322, 300, 387, 327 and 437 keV transitions. This spectrum was obtained from a recoil-gated cube composed entirely of fold-three events.

suggests that the high-Ω $[514]9/2^-$ deformation-aligned orbital also has a role in the underlying configuration of this band. Since Band 3 is likely to be based on coupling the odd proton to a negative-parity two-quasineutron excitation (see later discussion), Band 3 is assigned as a positive parity structure.

Table 4.1: Measured properties of γ rays assigned to band 1 ($\alpha = +1/2$) in ^{163}Ta.

E_γ (keV)	I_γ (%)	DCO	J_i^π	$\rightarrow$	J_f^π	$\frac{B(M1)}{B(E2)}$ $(\mu_N/eb)^2$	λ
144.94(30)	17.8(8)	1.07(10)	$(15/2^-)$	$\rightarrow$	$(13/2^-)$	1.39(40)	2.58(54)
432.15(40)	100(4)	1.06(7)	$(15/2^-)$	$\rightarrow$	$(11/2^-)$		
175.4(10)	12.1(5)		$(19/2^-)$	$\rightarrow$	$(17/2^-)$	0.69(20)	11.06(32)
567.11(10)	93(3)	1.11(6)	$(19/2^-)$	$\rightarrow$	$(15/2^-)$		
194.5(10)	6.9(3)		$(23/2^-)$	$\rightarrow$	$(21/2^-)$	0.97(40)	12.96(54)
669.39(13)	60.7(21)	1.12(7)	$(23/2^-)$	$\rightarrow$	$(19/2^-)$		
210.3(10)	5.8(3)		$(27/2^-)$	$\rightarrow$	$(25/2^-)$	2.28(46)	7.41(16)
739.9(10)	45.3(16)	1.19(12)	$(27/2^-)$	$\rightarrow$	$(23/2^-)$		
141.7(10)	9.7(4)		$(31/2^-)$	$\rightarrow$	$(29/2^-)$		
635.3(10)	32.5(11)		$(31/2^-)$	$\rightarrow$	$(27/2^-)$		
220.4(10)	18.0(6)	0.91(8)	$(35/2^-)$	$\rightarrow$	$(33/2^-)$	4.24(86)	0.20(4)
420.5(10)	10.4(4)		$(35/2^-)$	$\rightarrow$	$(31/2^-)$		
279.0(10)	17.0(6)		$(39/2^-)$	$\rightarrow$	$(37/2^-)$	2.30(40)	0.55(9)
521.8(10)	10.6(4)		$(39/2^-)$	$\rightarrow$	$(35/2^-)$		
305.8(10)	14.4(5)	0.72(15)	$(43/2^-)$	$\rightarrow$	$(41/2^-)$	3.43(167)	0.50(24)
589.1(10)	9.3(4)		$(43/2^-)$	$\rightarrow$	$(39/2^-)$		
338.4(10)	10.2(4)		$(47/2^-)$	$\rightarrow$	$(45/2^-)$		
662.3(10)	8.2(4)		$(47/2^-)$	$\rightarrow$	$(43/2^-)$		
369.9(10)	6.5(3)		$(51/2^-)$	$\rightarrow$	$(49/2^-)$		
724.1(10)	4.4(4)		$(51/2^-)$	$\rightarrow$	$(47/2^-)$		
402.4(10)	3.46(19)		$(55/2^-)$	$\rightarrow$	$(53/2^-)$		
780.2(10)	3.7(3)		$(55/2^-)$	$\rightarrow$	$(51/2^-)$		

Table 4.2: Measured properties of γ rays assigned to band 1 ($\alpha = -1/2$) in ^{163}Ta.

E_γ (keV)	I_γ (%)	DCO	J_i^π	$\rightarrow$	J_f^π	$\frac{B(M1)}{B(E2)}$ $(\mu_N/eb)^2$	λ
287.15(3)	81.0(3)	1.11(4)	$(13/2^-)$	$\rightarrow$	$(11/2^-)$	0.77(12)	0.67(11)
391.9(10)	44.4(17)		$(17/2^-)$	$\rightarrow$	$(15/2^-)$		
537.5(10)	31.3(12)		$(17/2^-)$	$\rightarrow$	$(13/2^-)$		
474.5(10)	24.3(10)		$(21/2^-)$	$\rightarrow$	$(19/2^-)$	0.36(6)	2.08(33)
649.9(10)	30.3(12)	0.99(10)	$(21/2^-)$	$\rightarrow$	$(17/2^-)$		
529.6(10)	12.5(6)		$(25/2^-)$	$\rightarrow$	$(23/2^-)$	0.42(11)	2.25(58)
724.1(10)	17.7(9)		$(25/2^-)$	$\rightarrow$	$(21/2^-)$		
493.6(10)	16.3(6)	1.05(14)	$(29/2^-)$	$\rightarrow$	$(27/2^-)$	0.98(28)	1.01(29)
703.9(10)	19.2(8)		$(29/2^-)$	$\rightarrow$	$(25/2^-)$		
200.1(10)	26.9(9)	1.03(7)	$(33/2^-)$	$\rightarrow$	$(31/2^-)$		
341.8(10)	5.2(3)		$(33/2^-)$	$\rightarrow$	$(29/2^-)$		
242.9(10)	20.2(7)		$(37/2^-)$	$\rightarrow$	$(35/2^-)$	3.94(154)	0.26(10)
463.3(10)	11.0(4)		$(37/2^-)$	$\rightarrow$	$(33/2^-)$		
283.2(10)	15.8(5)		$(41/2^-)$	$\rightarrow$	$(39/2^-)$		
562.2(10)	13.8(6)		$(41/2^-)$	$\rightarrow$	$(37/2^-)$		
323.8(10)	12.0(4)		$(45/2^-)$	$\rightarrow$	$(43/2^-)$		
629.7(10)	12.9(5)		$(45/2^-)$	$\rightarrow$	$(41/2^-)$		
354.2(10)	8.0(3)		$(49/2^-)$	$\rightarrow$	$(47/2^-)$		
692.6(10)	8.0(4)		$(49/2^-)$	$\rightarrow$	$(45/2^-)$		
377.8(10)	4.73(23)		$(53/2^-)$	$\rightarrow$	$(51/2^-)$		
747.7(10)	5.4(3)		$(53/2^-)$	$\rightarrow$	$(49/2^-)$		
413.0(10)	4.62(24)		$(57/2^-)$	$\rightarrow$	$(55/2^-)$		
815.4(10)	2.33(22)		$(57/2^-)$	$\rightarrow$	$(53/2^-)$		
880.0(10)	1.12(20)		$(61/2^-)$	$\rightarrow$	$(57/2^-)$		

Table 4.3: Measured properties of γ rays assigned to Band 2 and linking transitions to Band 1.

E_γ (keV)	I_γ (%)	DCO	J_i^π	$\rightarrow$	J_f^π	$\frac{B(M1)}{B(E2)}$ $(\mu_N/eb)^2$	λ
1067.2(10)	7.4(9)		$(17/2^+)$	$\rightarrow$	$(15/2^-)$		
178.25(10)	3.17(18)		$(19/2^+)$	$\rightarrow$	$(17/2^+)$		
853.5(10)	24.0(11)	0.69(9)	$(19/2^+)$	$\rightarrow$	$(17/2^-)$		
220.1(10)	9.9(5)		$(21/2^+)$	$\rightarrow$	$(19/2^+)$		
398.3(10)	2.12(25)		$(21/2^+)$	$\rightarrow$	$(17/2^+)$		
898.4(10)	25.5(11)	0.54(8)	$(21/2^+)$	$\rightarrow$	$(19/2^-)$		
224.9(10)	9.7(4)	1.04(10)	$(23/2^+)$	$\rightarrow$	$(21/2^+)$		
444.9(10)	11.8(5)	1.55(18)	$(23/2^+)$	$\rightarrow$	$(19/2^+)$		
648.6(10)	19.3(8)		$(23/2^+)$	$\rightarrow$	$(21/2^-)$		
131.7(10)	12.1(5)	1.09(16)	$(25/2^+)$	$\rightarrow$	$(23/2^+)$		
356.6(10)	7.2(3)		$(25/2^+)$	$\rightarrow$	$(21/2^+)$		

Table 4.4: Measured properties of γ rays assigned to Band 3.

E_γ (keV)	I_γ (%)	DCO	J_i^π $\hbar$	$\rightarrow$	J_f^π $\hbar$	$\frac{B(M1)}{B(E2)}$ $(\mu_N eb)^2$	λ
160.8(10)	17.3(6)	1.10(10)	$(29/2^+)$	$\rightarrow$	$(27/2^+)$	1.51(39)	0.19(3)
280.0(10)	7.6(3)		$(29/2^+)$	$\rightarrow$	$(25/2^+)$		
245.1(10)	20.1(7)		$(33/2^+)$	$\rightarrow$	$(31/2^+)$	2.71(62)	0.36(7)
459.9(10)	9.5(4)		$(33/2^+)$	$\rightarrow$	$(29/2^+)$		
321.6(10)	14.4(5)		$(37/2^+)$	$\rightarrow$	$(35/2^+)$	1.35(52)	1.04(30)
583.6(10)	9.9(4)		$(37/2^+)$	$\rightarrow$	$(33/2^+)$		
386.8(10)	10.5(4)		$(41/2^+)$	$\rightarrow$	$(39/2^+)$		
687.0(10)	9.8(5)		$(41/2^+)$	$\rightarrow$	$(37/2^+)$		
437.4(10)	5.2(3)		$(45/2^+)$	$\rightarrow$	$(43/2^+)$		
764.6(10)	5.3(3)		$(45/2^+)$	$\rightarrow$	$(41/2^+)$		
475.6(10)	1.4(3)		$(49/2^+)$	$\rightarrow$	$(47/2^+)$		
826.4(10)	3.3(3)		$(49/2^+)$	$\rightarrow$	$(45/2^+)$		
119.2(10)	11.8(5)	0.96(13)	$(27/2^+)$	$\rightarrow$	$(25/2^+)$		
250.9(10)	4.45(24)		$(27/2^+)$	$\rightarrow$	$(23/2^+)$		
214.8(10)	19.7(7)	0.65(8)	$(31/2^+)$	$\rightarrow$	$(29/2^+)$	3.67(105)	0.14(3)
375.5(10)	7.1(3)		$(31/2^+)$	$\rightarrow$	$(27/2^+)$		
262.0(10)	17.1(6)		$(35/2^+)$	$\rightarrow$	$(33/2^+)$	2.55(78)	0.51(13)
507.1(10)	15.8(7)		$(35/2^+)$	$\rightarrow$	$(31/2^+)$		
300.2(10)	11.7(4)		$(39/2^+)$	$\rightarrow$	$(37/2^+)$	2.72(132)	0.87(40)
621.8(10)	14.8(6)		$(39/2^+)$	$\rightarrow$	$(35/2^+)$		
327.2(10)	7.4(3)		$(43/2^+)$	$\rightarrow$	$(41/2^+)$		
714.0(10)	11.8(5)		$(43/2^+)$	$\rightarrow$	$(39/2^+)$		
350.8(10)	3.50(20)		$(47/2^+)$	$\rightarrow$	$(45/2^+)$		
788.2(10)	7.2(4)		$(47/2^+)$	$\rightarrow$	$(43/2^+)$		

4.4 Discussion

4.4.1 Configuration assignments

The underlying orbital configurations of the strongly coupled bands in ^{163}Ta can be interpreted in terms of quasiparticle configurations within the framework of Woods-Saxon cranking calculations. Quasiparticle Routhians, e', calculated for ^{163}Ta are displayed in Fig. 4.5. Details regarding the cranking calculations and the labelling convention for quasiparticle Routhians are given in Chapter 4, Section 3.5. The deformation parameters (β_2=0.170, γ=0°) used in the cranking calculations are the values predicted in reference [MNK95]. The quasiproton routhians as a function of rotational frequency are shown in Fig. 4.5(a). The negative-parity high-Ω orbitals originating from the proton $h_{11/2}$ sub-shell are the lowest energy proton levels which is consistent with the assignment of the yrast band (Band 1) being based on an odd proton in a deformation-aligned orbital. The first $h_{11/2}$ quasiproton alignment is blocked in ^{163}Ta and the cranking calculations predict that the next available quasiproton alignments do not occur until rotational frequencies higher than $\hbar\omega$=0.4 MeV. On this basis, the protons are not expected to influence the aligned band structures significantly in frequency range observed in this experiment. Thus, the first aligned and excited bands will be based on quasineutron excitations.

In order to determine the underlying orbital structure of the strongly coupled bands in ^{163}Ta, the experimental data are presented in terms of the aligned angular momentum, i_x, as a function of rotational frequency. Figure 4.6(a) compares the deduced alignments, i_x, extracted from the level scheme. A rotational reference, based on a configuration with a rotational moment of inertia defined by the Harris parameters J_0= 25 $\hbar^2$MeV^{-1} and J_1=32 $\hbar^4$MeV^{-3}, has been subtracted from each band. This reference was chosen to give a constant alignment for the

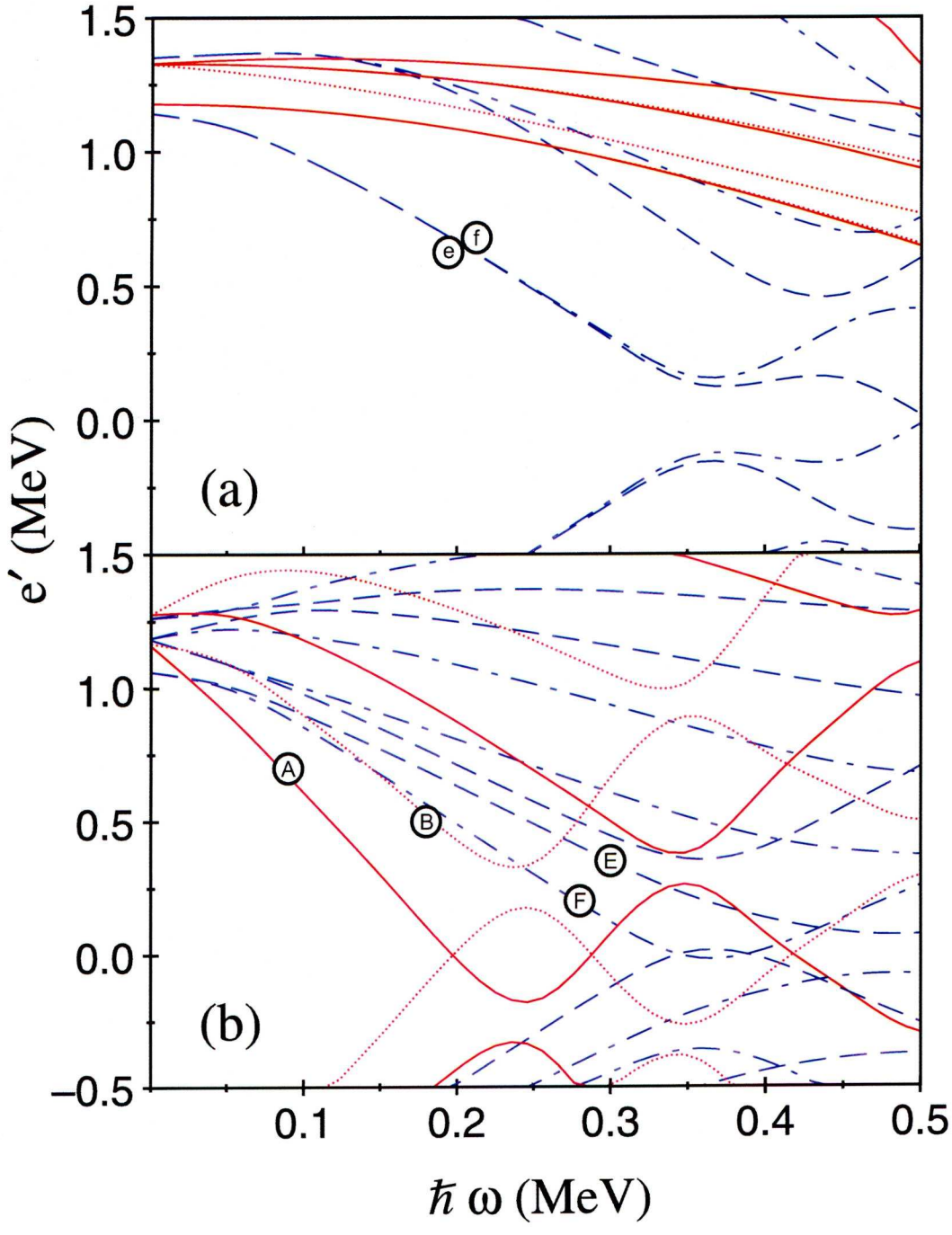

Figure 4.5: Cranked Woods-Saxon Routhian diagrams for ^{163}Ta assuming deformation parameters (β_2=0.170, γ=0°) from reference [MNK95]. (a) Quasiprotons. (b) Quasineutrons.

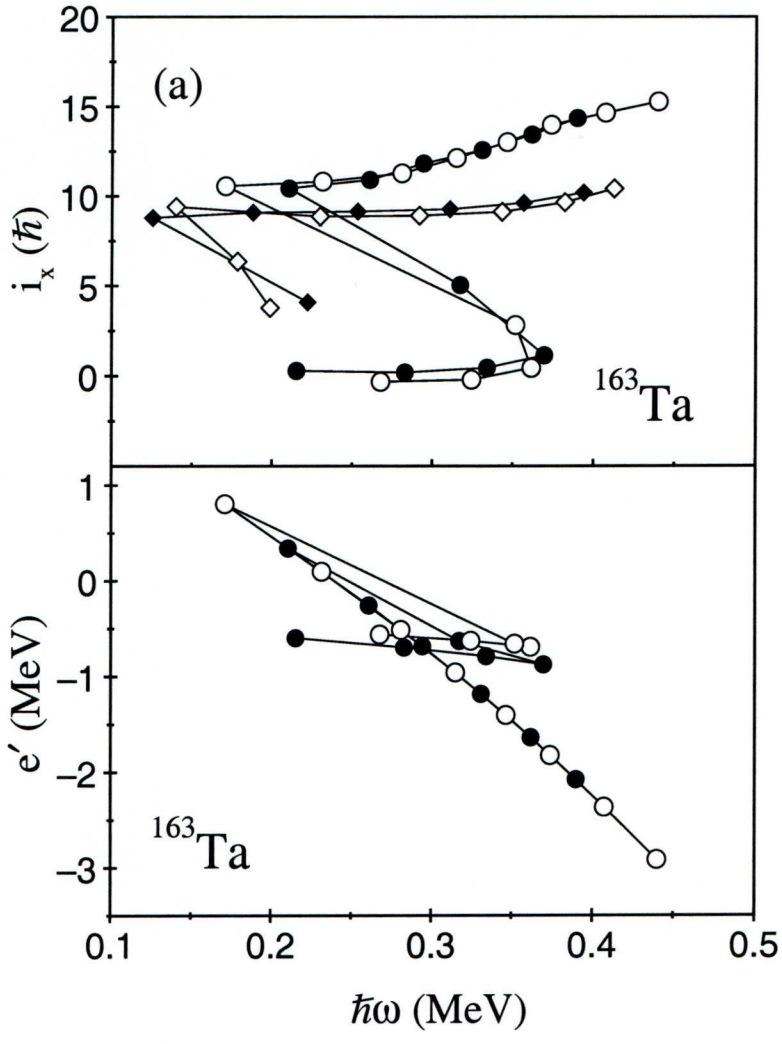

Figure 4.6: (a) The aligned angular momentum, i_x as a function of rotational frequency for the bands in ^{163}Ta. (b) Experimental routhians e' as a function of rotational frequency for the bands in ^{163}Ta.

low-spin states of ^{163}Ta.

The low-spin yrast band (Band 1) in ^{163}Ta is interpreted as a one-quasiproton configuration based on the [514]9/2$^-$ Nilsson state originating from the $h_{11/2}$ subshell and continues the trend established in the heavier even-N Ta isotopes. At higher spins, Band 1 undergoes a quasiparticle alignment. After the backbend, Band 1 carries an alignment of 11.8 $\hbar$ at $\hbar\omega = 0.3$ MeV. The experimental Routhians, shown in Fig. 4.6(b) indicate that the crossing frequency for this alignment is

0.3 MeV. The quasineutron Routhians displayed in Fig. 4.5(b) indicate that the high-j, low-Ω $[660]1/2^+$ orbitals from the $i_{13/2}$ subshell are closest to the Fermi surface aligning at $\sim$ 2.4 MeV. The addition of the slopes of these positive-parity Routhians ($i_x = -de'/d\omega$) yields the predicted alignment gain of 10.6 $\hbar$. This constitutes the largest possible alignment from the orbitals near the Fermi surface and is in excellent agreement with the experimental value.

The experimental alignments for bands in ^{163}Ta are compared with the alignment properties of the neighbouring N=90 isotones ^{162}Hf and ^{164}W in Fig. 4.7. The aligned configurations in the yrast bands in the ^{162}Hf and ^{164}W neighbours have been interpreted as the $(i_{13/2})^2$ (AB) two-quasineutron configurations. Figure 4.7(b) shows the effect of applying an offset ($\Delta I_x = -3$) to the total aligned angular momentum so that the one-quasiparticle $h_{11/2}$ configuration of Band 1 in ^{163}Ta carries the same alignment as the vacuum configuration in the neighbouring even-even isotones. It is clear that same alignment gain is observed in all three nuclei. Thus, the $i_{13/2}$ (AB) quasineutron alignment is responsible for the backbend in Band 1 transforming the one quasiproton $h_{11/2}$ (e or f) configurations into the three quasiparticle $\pi h_{11/2} \otimes \nu(i_{13/2})^2$ (eAB or fAB) configurations. The alignments, i_x, for Bands 2 and 3 in ^{163}Ta, are plotted as a single sequence in Fig. 4.6(a). Band 2 displays an abrupt alignment gain leading to a constant alignment of 9.1 at $\hbar\omega$=0.3 MeV for Band 3. The alignment of Band 2 is too low to originate from a three-quasiparticle configuration. Similar alignment patterns have been observed in neighbouring nuclei in this region which have been interpreted in terms of coupling yrast bandhead configuration to an octupole phonon. The close proximity of $\nu f_{7/2}$ and $\nu i_{13/2}$ (Δj=3) orbitals to the Fermi surface can lead to octupole correlations. Furthermore, the DCO ratios and deduced $B(E1 : I \rightarrow I-1)$ values measured for the 898 keV linking transition between Band 1 and Band 2 are suggestive of E1 character which may indicate octupole correlations. The alignment of Band 3 is lower than the value observed for the

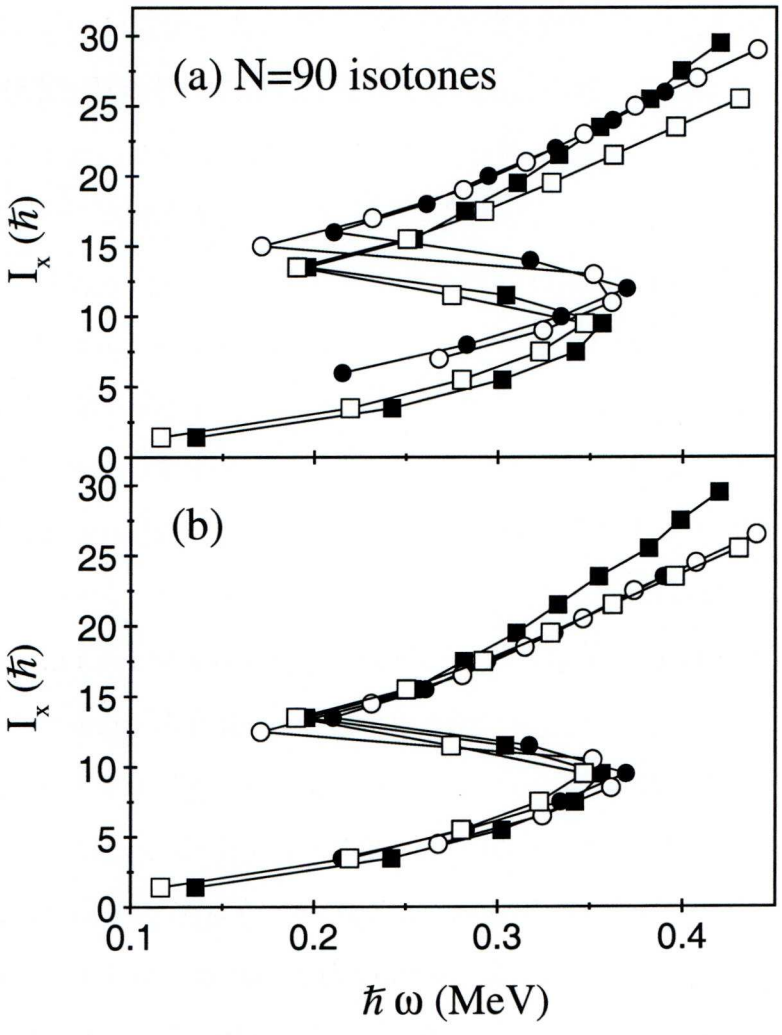

Figure 4.7: Total aligned angular momentum, I_x, as a function of rotational frequency for the N=90 isotones ^{162}Hf (open squares), ^{163}Ta (circles) and ^{164}W (filled squares). (b) The same as (a) but with an offset to give the one-quasiparticle $h_{11/2}$ configuration of Band 1 in ^{163}Ta the same alignment as the vacuum configuration in the neighbouring even-even isotones.

eAB/fAB aligned configurations of Band 1. Figure 4.5(b) indicates that the lowest lying, positive-parity configuration is formed by coupling an $i_{13/2}$ quasineutron and one of the nearby negative-parity $f_{7/2}, h_{9/2}$ states to the odd proton. The predicted alignment gain for this configuration is 9.6 $\hbar$ which is in excellent agreement with the measured value (9.1 $\hbar$). Thus, Band 3 is likely to be a three-quasiparticle

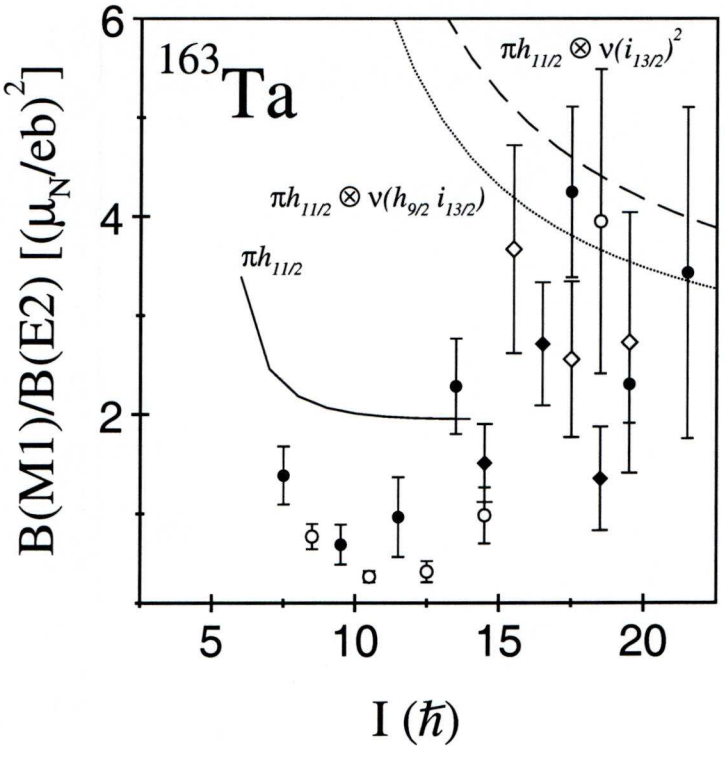

Figure 4.8: Experimental $B(M1 : I \rightarrow I-1)/B(E2 : I \rightarrow I-2)$ reduced transition strength ratios as a function of spin I for ^{163}Ta. Measured values are compared with the predictions of the semiclassical model of Dönau and Frauendorf for the e (solid line), eAB (dashed line), and eAE (dotted line) configurations. Ratios for Band 1 and Band 3 are depicted by circles or diamonds, respectively. The filled (open) symbols represent the α=1/2 ($-1/2$) signature.

configuration based on $\pi h_{11/2} \otimes \nu(i_{13/2})(f_{7/2}, h_{9/2})$ (eAE or fAE) configurations. These assignments are supported by $B(M1; I \rightarrow I-1))/B(E2; I \rightarrow I-2)$ ratios that have been extracted from experimental γ-ray branching ratios of competing $\Delta I = 1$ and $\Delta I = 2$ transitions using Eq. 4.2. Figure 4.8 compares the experimental ratios with theoretical calculations for the assigned configurations using the semiclassical formalism of Dönau and Frauendorf [DF83, Dön87]. The calculations are dependent on many variables and assume a quadrupole deformation of β_2=0.170 and γ=0°. The g-factors were obtained from cranked Woods-Saxon cal-

culations. The M1/E2 multipole mixing ratio was set to zero since the $1/(1+\delta^2)$ term is approximately equal to unity. The calculations do not agree exactly with the measured ratios, but the general trends are in reasonable agreement with theoretical calculations.

4.4.2 Shape changes along the yrast line in ^{163}Ta

The relative positions of the proton and neutron Fermi surfaces at the top and bottom of their respective subshells makes it possible for ^{163}Ta to adopt a triaxial or γ-soft shape [Lean83]. Signature splitting in strongly coupled bands may indicate that a given nucleus has adopted a triaxial deformation. Since γ-soft nuclei are highly susceptible to the core polarising influences of orbitals at the Fermi surface, comparisons of signature splitting with quasiparticle alignments can provide insights into the deformation driving character of specific orbitals. The yrast band in ^{163}Ta exhibits significant signature splitting at low spins in contrast to the predictions of the Woods-Saxon cranking calculations displayed in Fig. 4.5(a). Figure 4.9(a) compares the signature splitting of Band 1 and Band 3 in terms of the staggering parameter $S(I)$ [Krei81] defined as

$$S(I) = E(I) - E(I-1) - \frac{1}{2}\left[E(I+1) - E(I) + E(I-1) - E(I-2)\right]. \quad (4.3)$$

Figure 4.9(a) shows that Band 1 exhibits large staggering until I=17 beyond which the staggering parameter assumes values close to zero. The staggering parameter for Band 1 in ^{163}Ta continues the trend established for the heavier even-N tantalum isotopes, see Fig. 4.9(b). The yrast states of the light even-N tantalum isotopes have almost identical staggering parameter variations as a function of spin. However, at low spin ($< 17\hbar$) the tantalum isotopes exhibit a trend of increased signature splitting towards greater neutron deficiency, indicating that these nuclei achieve greater deviations from γ=0° as the closed shell at N=82 is approached. This feature has also recently been observed in the neutron-deficient

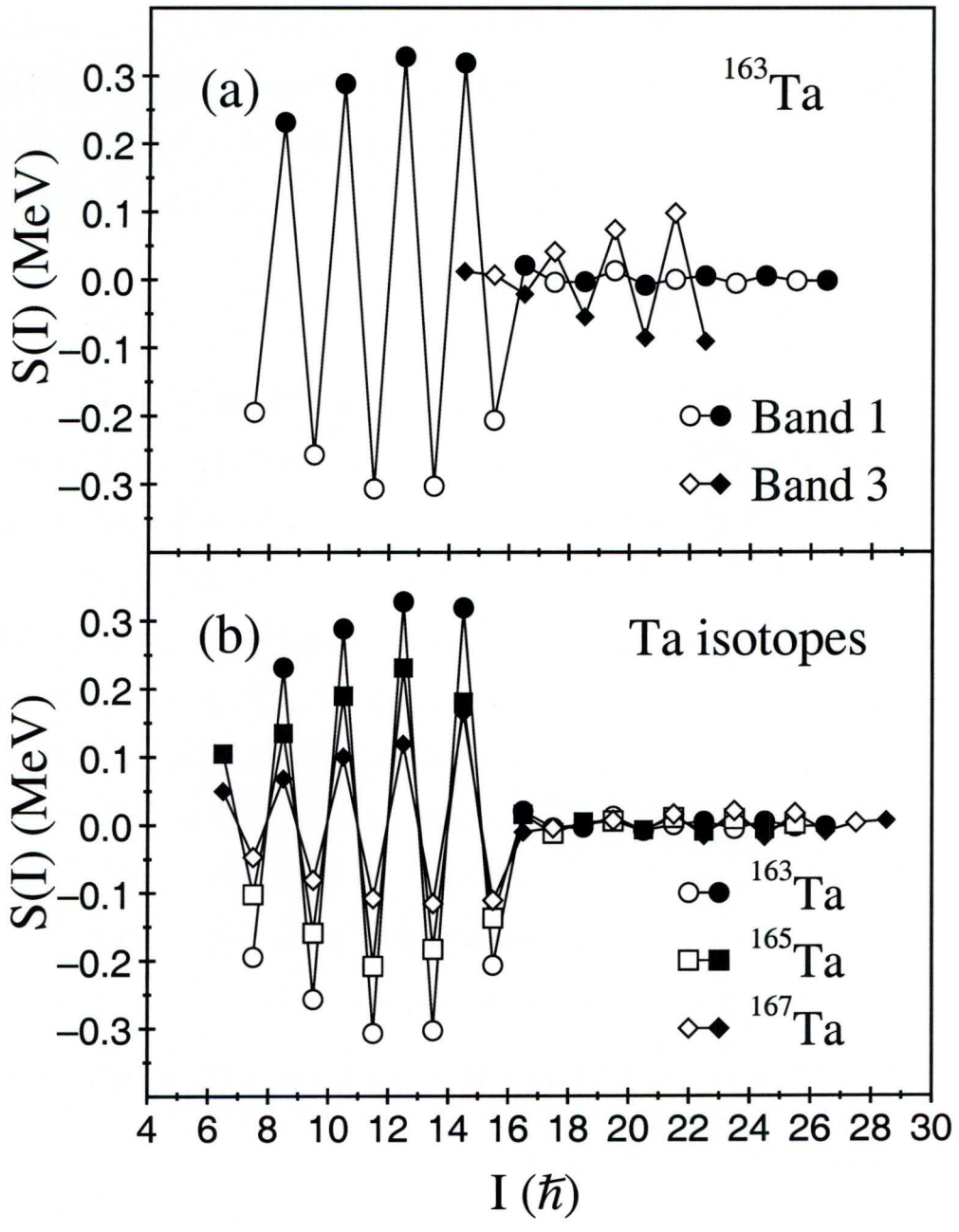

Figure 4.9: Staggering parameter S(I) as a function of spin I for (a) the strongly coupled bands in ^{163}Ta. (b) The [514]9/2$^-$ yrast bands in the neutron-deficient odd-A tantalum isotopes ^{163}Ta, ^{165}Ta and ^{167}Ta. The filled (open) symbols represent the α=1/2 ($-1/2$) signature.

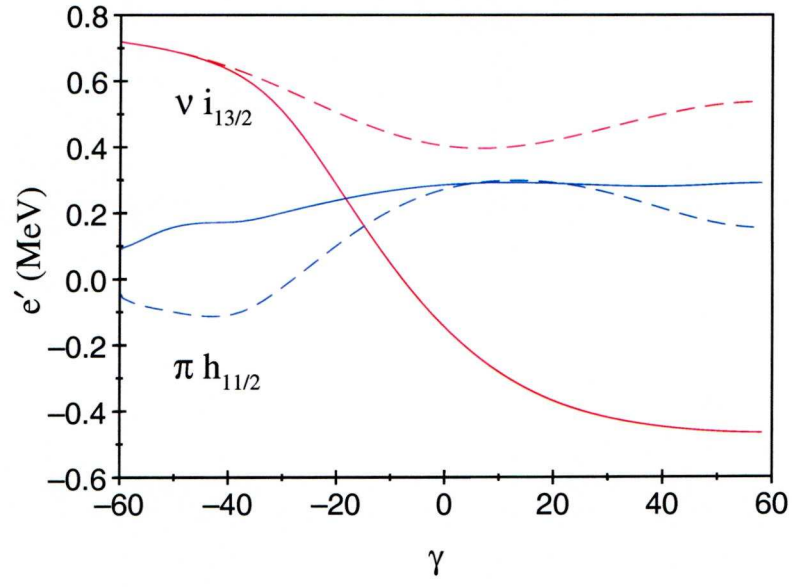

Figure 4.10: Calculated $h_{11/2}$ quasiproton (blue) and $i_{13/2}$ quasineutron (red) energies as a function of γ deformation. The calculations were performed for a nucleus with β_2=0.170 at rotational frequency $\hbar\omega$=0.1 MeV.

Re isotopes [Joss03]. The $E(4^+)/E(2^+)$ ratios in the neighbouring N=90 isotones ^{162}Hf and ^{164}W have values of 2.6 and 2.5, respectively which are close to the ideal ratio for a γ-soft rotor, $E(4^+)/E(2^+)$=2.5. Therefore, it is reasonable to assume that ^{163}Ta is also a γ-soft rotor at low spin.

This large signature splitting in Band 1 at low spin could easily arise from a triaxial deformation caused by the competing core polarizing influences of the high-Ω $h_{11/2}$ proton and the low-Ω $i_{13/2}$ neutrons. After the $i_{13/2}$ quasineutron pair alignment, the staggering parameter virtually disappears, reflecting a dramatic reduction in signature splitting, which is indicative of the transition to an axially symmetric prolate shape. This reveals the prolate driving influence of the aligned low-Ω $i_{13/2}$ neutrons. The influence of γ deformation on these orbitals is shown in Fig. 4.10, which shows the quasiparticle Routhians as a function of γ deformation as calculated in the framework of the cranked shell model. The cranking calculations and the staggering parameter trends are consistent with a

transition from a triaxial deformation ($\gamma \sim -30°$) to an axially symmetric prolate shape ($\gamma = 0°$) with increasing spin in the yrast states of ^{163}Ta.

The staggering parameter for Band 3 exhibits signature splitting to a lower degree than observed for the low-spin states of Band 1 but shows greater staggering than Band 1 at higher spins. Indeed, the staggering parameter for Band 3 increases gradually as a function of angular momentum. These features are consistent with the configuration assignments made in the previous section. Band 3 was assigned the $\pi h_{11/2} \otimes \nu(i_{13/2})(f_{7/2}, h_{9/2})$ (eAE or fAE) configuration. This configuration has only one $i_{13/2}$ quasineutron and so should have more signature splitting than observed for the $\nu(i_{13/2})^2$ (eAB or fAB) configuration. Furthermore, the quasiproton Routhians for the $h_{11/2}$ signature partners in Fig. 4.5(a) will gradually split towards higher rotational frequencies: this effect will be more pronounced at lower frequencies if the nucleus is triaxial.

4.4.3 Evolution of nuclear structure towards N=82

The evolution of quadrupole deformation towards the N=82 closed shell has dramatic consequences for the relative excitation energies of single-particle orbits. This was shown in the discussion of the tungsten isotopes in the previous Chapter. As for the light tungsten isotopes, the neutron Fermi surface is also close to orbitals originating from the $f_{7/2}$, $h_{9/2}$ or $i_{13/2}$ subshells in the nearby odd-Z tantalum isotopes. It is interesting to determine the point where the influence of the lowest-Ω $i_{13/2}$ neutron orbital wanes and the negative parity $f_{7/2}$ and $h_{9/2}$ neutron states begin to dominate the yrast structures of the neutron-deficient Ta isotopes. The total aligned angular momentum as a function of rotational frequency for the lightest known odd-A Ta isotopes with collective bands are plotted in Fig. 4.11. The yrast bands in the ^{163}Ta, ^{165}Ta and ^{167}Ta all exhibit alignment gains consistent with the alignment of a pair of $i_{13/2}$ quasineutrons.

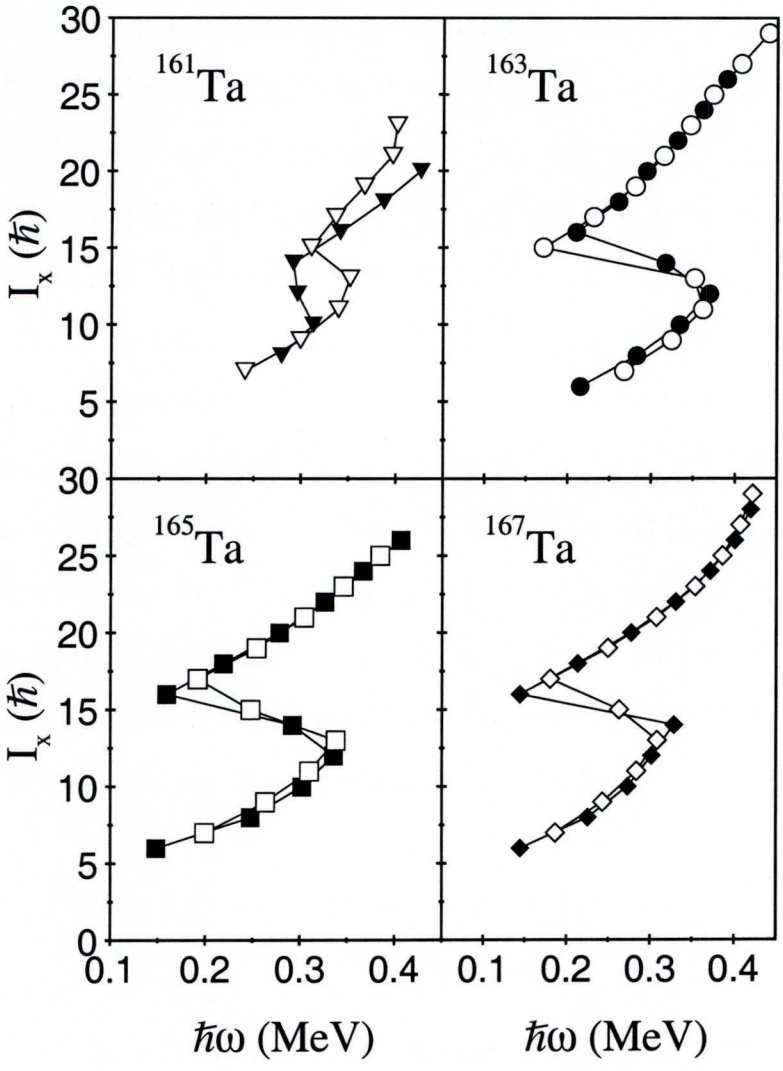

Figure 4.11: A comparison of the total aligned angular momentum for the tantalum isotopes.

However, the yrast sequence of ^{161}Ta, observed by Lagergren *et al.* [Lag08] shows a markedly lower alignment gain. The total aligned angular momenta for ^{161,163}Ta and ^{162,164}W are compared in Fig. 4.12. Indeed, this alignment gain for ^{161}Ta is similar to that observed for ^{162}W ($\Delta I_x \sim 6\hbar$). From these comparisons it is possible to confirm that the $i_{13/2}$ orbital is further from the Fermi surface than the negative-parity orbitals originating from the $f_{7/2}$ and $h_{9/2}$ sub-shells. This feature is interpreted as occurring as a consequence of a trend towards lower

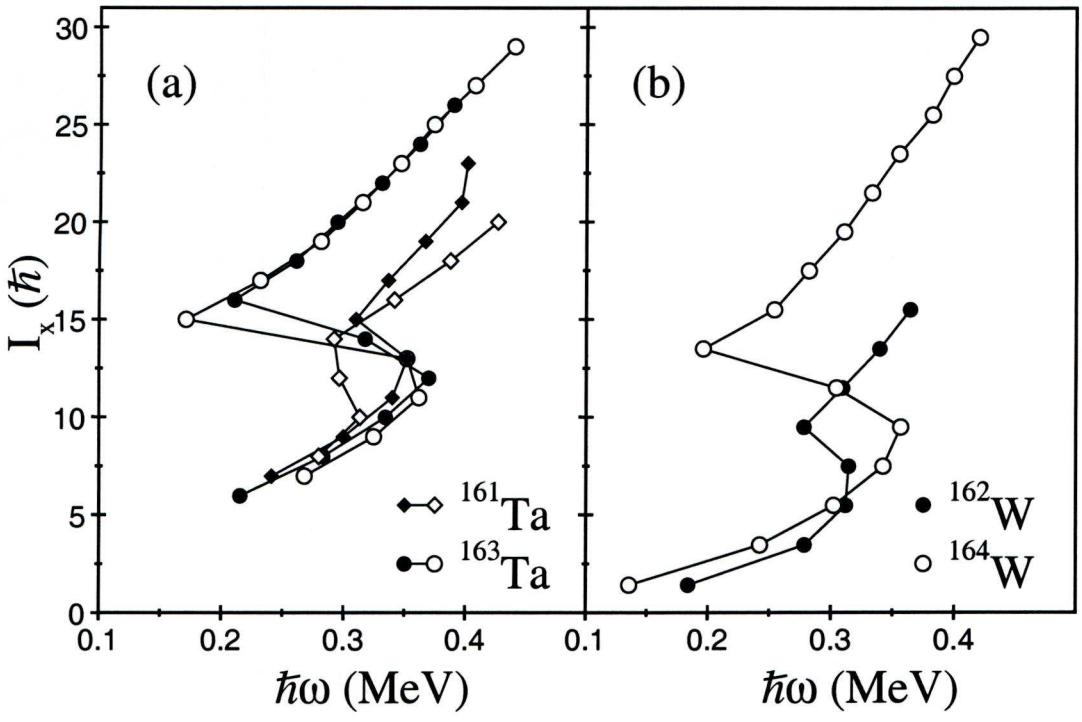

Figure 4.12: A comparison of the total aligned angular momentum, I_x as a function of rotational frequency for the yrast bands of $N = 88$ and N=90 (a) tantalum isotopes and (b) tungsten isotopes.

deformation with the removal of neutron approaching N=82. Thus, the change in structure observed in the Ta isotopes occurs between $N = 88$ and $N = 90$ as observed between ^{162}W and ^{164}W isotopes.

4.5 Summary

Three strongly coupled bands have been established in ^{163}Ta for the first time in an experiment using the JUROGAM γ-ray spectrometer in conjunction with the RITU gas-filled separator and the GREAT spectrometer. The configuration assignments for these new structures are based on comparisons between experimental values for the total aligned angular momenta (I_x) and the predictions of the cranked shell model. Further comparisons of experimental $B(M1)/B(E2)$

ratios have been made with the predictions of the semiclassical model of Dönau and Frauendorf and support the assigned configurations.

At low spin, the yrast band (Band 1), is based on a single quasiparticle configuration based on the odd proton occupying a $h_{11/2}$ state. At higher spins the yrast configuration undergoes an alignment gain consistent with the adoption of a three quasiparticle configuration formed by the rotational alignment of an $i_{13/2}$ quasineutron pair $[\pi h_{11/2} \otimes \nu(i_{13/2})^2]$. The yrast band has been shown to have large signature splitting at low spin continuing the trend of increasing signature splitting with decreasing neutron number established in the heavier odd-A Ta isotopes. The signature splitting vanishes with the alignment of the $i_{13/2}$ quasineutrons. These features are interpreted in terms of a γ-soft triaxial shape at low spin that is polarized by the $i_{13/2}$ neutron alignment to adopt a prolate shape. Comparisons of the total aligned angular momenta as a function of rotational frequency for the yrast bands in the nearby odd-A Ta isotopes reflect changes in the relative order of single-particle orbitals as the N=82 shell gap is approached. The aligning orbitals change from $i_{13/2}$ quasineutrons in the yrast band of ^{163}Ta and heavier isotopes to $h_{9/2}$ quasineutrons in ^{161}Ta.

The first excited band, Band 2, is assigned to be a negative parity structure on the basis of angular correlations and is based on a configuration formed by coupling the odd proton to an octupole excitations $[\pi h_{11/2} \otimes 3^-]$. This is supported by high $B(E1)$ values extracted from experimental $B(E1)/B(E2)$ ratios. Band 3 is assigned to be a three-quasiparticle configuration based on the $\pi h_{11/2} \otimes \nu(i_{13/2})(f_{7/2}, h_{9/2})$ configuration.

Chapter 5

Conclusions

The A ~163 isobars have been investigated using the ^{106}Cd(^{60}Ni,xpyn) reaction at a bombarding energy of 270 MeV in an experiment using the JUROGAM and GREAT spectrometers in conjunction with the RITU gas-filled separator. A high-fold coincidence analysis has revealed five new band structures in ^{163}W and extended the known yrast sequence built on the $13/2^+$ isomer. The decay paths from the $13/2^+$ isomer have been determined using γ-ray and conversion electron spectroscopy allowing the relative excitation energies of single-particle $f_{7/2}$, $h_{9/2}$ and $i_{13/2}$ band heads to be fixed. In addition, the neighbouring isotopes ^{162}W and ^{164}W have been studied. A modest extension has been made to the ^{164}W level scheme and the yrast sequence in ^{162}W has been confirmed by recoil-decay tagging.

The odd-A isobar ^{163}Ta has also been studied in the same experiment and a level scheme comprising three strongly coupled bands has been established for the first time. At low spin, this nucleus has been interpreted in terms of an odd-proton $h_{11/2}$ configuration coupled to a γ-soft core. At higher spins, the yrast band achieves a prolate shape as indicated by the vanishing of signature splitting. This is attributed to the alignment of a pair of $i_{13/2}$ neutrons.

These results suggest that the neutron-deficient isobars, ^{163}Ta and ^{163}W, repre-

sent pivotal points in terms of changing nuclear structure approaching the N=82 shell closure and the proton drip line. Towards greater neutron deficiency, the average quadrupole deformation decreases in each isotopic chain sufficiently to promote a change in the relative positions of the valence orbitals. In the tungsten isotopes A ~163 represents the point where the $i_{13/2}$ achieves a higher excitation energy above the Fermi surface compared to the heavier isotopes. Consequently, the first rotationally aligned configuration is formed by the negative-parity $f_{7/2}, h_{9/2}$ neutron orbitals. In ^{163}Ta, the $i_{13/2}$ neutron orbitals are found to be in closer proximity to the Fermi surface. Indeed, the first rotational alignment is consistent with a pair of $i_{13/2}$ neutrons as observed in the heavier isotopes ^{165}Ta and ^{167}Ta. However, the lighter even-N isotope, ^{161}Ta, has a much lower alignment gain at the first band crossing. This is indicative of the $h_{9/2}$ neutron alignment. Thus, a comparison with the lighter isotope suggests that ^{163}Ta is the lightest even-N isotope for which the $i_{13/2}$ orbitals constitute the first quasiparticle alignment. This is entirely consistent with the observations for the light tungsten isotopes [Drac92].

There is scope for future experimental investigation. The ground-state deformation is also predicted to change as the Z=82 shell closure is approached. Consequently, similar changes in the orbitals responsible for the first rotational alignment should be apparent in the more proton-rich isobars. An investigation of ^{163}Re was undertaken as part of the data analysis for this thesis and has been reported elsewhere [Joss08]. The low production cross section for this nucleus relative to competing the reaction channels proved challenging. An RDT study was undertaken and $E_{\gamma 1} - E_{\gamma 2}$ matrices produced. It was noted that the strongest transitions were found to be self coincident doublets (possibly self-coincident triplets) and it was not possible to determine the level scheme beyond the first band crossing. These issues may be resolved in the future by exploiting the higher photopeak efficiency of the next generation γ-ray spectrometer,

AGATA [Simp05].

In general, investigations closer to (and beyond) the N=Z=82 shell closure and the proton drip line face several experimental challenges. Towards even greater neutron deficiency, the average deformation and collectivity in nuclei wanes and single-particle excitations become dominant. This transition is reflected in the irregular decay patterns observed in γ-ray spectra for the most neutron-deficient nuclei. While increasing the γ-ray detection efficiency can help unravel the complex level schemes, there are problems related to separating γ rays from these weakly populated channels from the large background from other channels including fission. The application of tagging techniques may not help since the half-lives of radioactive decays used as tags may become too short to survive the flight time through the recoil separator [Joss06b, Joss07]. There may be considerable advantages associated with the use of the LISA spectrometer for the detection of sub-microsecond radioactive decays emitted at the target position [Page09]. Such experimental studies may allow the identification of previously inaccessible excited states.

Bibliography

[An04] A. N. Andreyev *et al.*, Nucl. Instrum. and Meth. in Phys. Res. **A533**, 533, (2004).

[Beau92] C.W. Beausang *et al.*, Nucl. Instrum. and Meth. in Phys. Res. **A313**, 37, (1992).

[Beau95] C.W. Beausang *et al.*, Nucl. Instrum. and Meth. in Phys. Res. **A364**, 560, (1995).

[Beau96] C.W. Beausang and J. Simpson, J. Phys. **G22**, 527, (1996).

[Beng79] R. Bengtsson and S. Frauendorf, Nucl. Phys. **A314**, 27 (1979) and Nucl. Phys. **A327**, 139 (1979).

[Beng90] T. Bengtsson, Nucl. Phys. **A512**, 124 (1990).

[BFM86] R. Bengtsson, S Frauendorf and F.R. May, At. Data Nucl. Data Tables **35**, 15, (1986).

[Bl78] M. Blann, University of Rochester Report No. URNSRL-181(1978).

[Bo40] N. Bohr, Phys. Rev. **58**, 654, (1940).

[BMP58] A. Bohr, B.R. Mottelson, and D. Pines, Phys. Rev. **110**, 936, (1958).

[BM75] A. Bohr and B.R. Mottelson, Nuclear Structure, Vol. II. Benjamin, New York, (1975).

[BM81] A. Bohr, and B. R. Mottelson, Phys. Scr. **24**, 71 (1981).

[Br72] M. Brack *et al.*, Rev. Mod. Phys. **44**, 320, (1979).

[But96] P.A. Butler and W. Nazarewicz, Rev. Mod. Phys. **68**, 349, (1996).

[Cab78] C. Cabot, S. Della Negra, C. Deprun, H. Gauvin, and Y. Le Beyec, Z. Phys. **A287**, 71, (1978).

[Coh58] B.L. Cohen and C.B. Fulmer, Nucl. Phys. **6**, 547, (1958).

[Cwi87] S. Cwiok, J. Dudek, W. Nazarewicz, W. Skalsi, and T. Werner, Comput. Phys. Commun. **46**, 379, (1987).

[Darb06] I.G. Darby, PhD Thesis, The University of Liverpool, (2006).

[DF83] F. Dönau and S. Frauendorf, in Proceedings of the Conference on High Angular Momentum Properties of Nuclei, Oak Ridge, edited by N. R. Johnson, Harwood, New York, 143 (1983).

[Dön87] F. Dönau, Nucl. Phys. **A471**, 469 (1987).

[Di27] P.A.M. Dirac, Proc. R. Soc. Lond. **A** 1927 114, 243-265

[Drac92] G.D. Dracoulis *et al.*, Proceedings of the International Conference of Nuclear Structure at High Angular Momentum, Ottawa, (1992), AECL Report No. 10613 (unpublished), Vol. 2, p. 94.

[East73] D.A. Eastham and I.S. Grant, Nucl. Phys. **A**208, 119, (1973).

[Ee06] S. Eeckhaudt PhD Thesis, The University of Jyväskylä, (2006).

[Fr83] S. Frauendorf and F.R. May *et al*, Phys. Lett. **B125**, 245, (1983).

[Gerl00] J. Gerl, Nucl. Instrum. Meth. Phys. Res. **A442**, 238, (2000).

[Gh88] A. Ghiorso *et al.*, Nucl. Instrum. and Meth. in Phys. Res. **A269**, 192, (1988).

[Gom09] M.B. Gòmez-Hornillos *et al.*, Phys. Rev. **C79**, 064314, (2009).

[GLN67] C. Gustafson, I.L. Lamm, B. Nilsson, and S.G. Nilsson, Arkiv Fysik **36**, 613, (1967).

[Hag92] E. Hagberg *et al.*, Phys. Rev. **C45**, 1609, (1992).

[Han93] F.F. Hanna, PhD Thesis, University of Liverpool, (1993).

[Har65] S.M. Harris, Phys. Rev. **138**, 509, (1965).

[Hax49] O. Haxel, J.H.D. Jensen and H.E. Suess, Phys. Rev. **75** 1766, (1949).

[Hey90] K.L.G. Heyde, The Nuclear Shell Model, Springer-Verlag, (1994).

[Hof79] S. Hofmann *et al.*, Z. Phys. **A**291, 53, (1979).

[Hof81] S. Hofmann, G. Münzenberg, F.P. Hessberger, W. Reisdorf, P. Armbruster, and B. Thuma, Z. Phys. **A299**, 281, (1981).

[Ing54] D.R. Inglis, Phys. Rev. **96**, 1059, (1954).

[Ir97] R.J. Irvine *et al.*, Phys. Rev. **C55**, R1621, (1997).

[Jam88] A.N. James *et al.*, Nucl. Instrum. and Meth. in Phys. Res. **A267** 144, (1988).

[John71] A. Johnson, H. Ryde and J. Sztarkier Phys. Lett. **B34**, 605, (1971).

[Joss03] D.T. Joss *et al.*, Phys. Rev. **C68**, 014303, (2003).

[Joss01] D.T. Joss *et al.*, Nucl. Phys. **A689**, 631, (2001).

[Joss04] D.T. Joss *et al.*, Phys. Rev **C70**, 017302, (2004).

[Joss06a] D.T. Joss *et* al., Phys. Rev. **C74**, 014302, (2006).

[Joss06b] D.T. Joss *et* al., Phys. Lett. **641**, 34, (2006).

[Joss07] D.T. Joss *et* al., AIP Conference Proceedings **961**, 28, (2007).

[Joss08] D.T. Joss *et* al., AIP Conference Proceedings **1072**, 154, (2008).

[Keen01] A. Keenan *et al.*, Phys. Rev. **C63**, 64309, (2001).

[Kib08] T. Kibédi, T.W. Burrows, M.B. Trzhaskovskaya, P.M. Davidson, C.W. Nestor Jr, Nucl. Instr. and Meth. **A589**, 202, (2008).

[King98] S.L. King *et al*, Physics Letters **B**443, 82, (1998).

[Knoll] G.F. Knoll, Radiation detection and measurement, Third edition, (2000).

[KSW72] K.S. Krane, R.M. Steffen and R.M. Wheeler, Bulletin of the American Physical Society **17**, 928, (1972).

[Krei81] A.J. Kreiner, M.A.J. Mariscotti, C. Baktash, E. der Mateosian, and P. Thieberger, Phys. Rev. **C23**, 748 (1981).

[Laz01] I.H. Lazarus *et al.*, IEEE Transactions on Nuclear Science **48** 567 (2001)

[Lag06] K.Lagergren *et al.*, Phys. Rev. **C74** 024316 (2006).

[Lag08] K. Lagergren, *Private Communication.*

[Lean83] G.A. Leander, S. Frauendorf, and F.R. May, in *P*roceedings of the Conference on High Angular Momentum Properties of Nucle, Oak Ridge, (1982), edited by N. R. Johnson Harwood Academic, New York, 281 (1983).

[Lee92] I.Y Lee, Prog. in Part. and Nucl. Phys. **28**, 473, (1992).

[Le95] M. Leino *et al.*, Nucl. Instrum. and Meth. in Phys. Res. **B99**, 653, (1995).

[Le03] M. Leino, Nucl. Instrum. and Meth. in Phys. Res. **B204**, 129, (2003).

[Li93] S.G. Li, Nucl. Phys. **A555**, 435, (1993).

[Lia85] C.F. Liang *et al.*, Z. Phys. **A321**, 696, (1985).

[Ma49] M.G. Mayer, Phys. Rev. **75**, 1969, (1949).

[Mo87] J.N. Mo *et al.*, Nucl. Phys. **A472**, 295, (1987).

[MNK95] P. Möller, J. R. Nix, W.D. Myers and W.J. Swiatecki, Atomic Data and Nuclear Data Tables, **59**, (1995).

[Mor63] H. Morinaga and P.C. Gugelot, Nucl. Phys. **46**, 210, (1963).

[New69] J.O. Newton, F.S. Stephens, R.M. Diamond, W.H. Kelly and D. Ward, Nucl. Phys. **A141**, 631, (1969).

[Nil55] S.G. Nilsson, Mat. Fys. Medd. Dan. Vid. Selsk. **69**, 16, (1955).

[Ni69a] B. Nilsson, Nucl. Phys. **A129**, 445, (1969).

[Ni69b] S.G. Nilsson *et al*, Nucl. Phys. **131**, 1, (1969).

[Ni95] S.G. Nilsson and I. Ragnarsson, *Shapes and Shells in Nuclear Structure*, Cambridge University Press, (1995).

[NBF94] P.J. Nolan, F.A. Beck and D.B. Fossan, Ann. Rev. Nucl. and Part. Sci. **44**, 561, (1994).

[O'Don09] D. O'Donnell *et al.*, Phys. Rev. **C79**, 051304(R), (2009).

[Page96] R.D. Page *et al.*, Phys. Rev. **C53**, 660, (1996).

[Page03] R.D. Page *et al.*, Nucl. Instrum. and Meth. in Phys. Res. **B204**, 634, (2003).

[Page07] R.D. Page *et al.*, Phys. Rev. **C**75, 061302(R), (2007).

[Page09] R.D. Page, *Private communication.*

[Paul95] E.S. Paul *et al.*, Phys. Rev. **C51**, 78, (1995).

[Paul97] E.S. Paul *et al.*, Nucl. Phys. **A619**, 177, (1997).

[Paul07] E.S. Paul, Postgraduate lecture notes, University of Liverpool, (2007).

[Paul09] E.S. Paul *et al.*, Phys. Rev. **C79**, 044324, (2009).

[Rad95] D.C. Radford, Nucl. Instrum. and Meth. in Phys. Res. **A361**, 297, (1995).

[Rah08] P. Rahkila, Nucl. Instrum. and Meth. in Phys. Res. **A595**, 637, (2008).

[Run86] E. Runte *et al.*, Z. Phys. **A324**, 119, (1986).

[Roux01] D. G. Roux *et al.*, Phys. Rev. **C63**, 024303, (2001).

[Roux02] D.G. Roux *et al.*, Phys. Rev. **C65**, 014308, (2002).

[Rytz91] A. Rytz *et al.*, At. Data Nucl. Data Tables **47**, 205, (1991).

[Se05] D. Seweryniak *et al.*, Phys. Rev, **C71**, 054319, (2005).

[Sc08] C. Scholey *et al.*, *in preparation.*

[Sc86] K.-H. Schmidt*et al.*, Phys. Lett. **B168**, 39, (1986).

[Sim86] R. S. Simon *et al.*, Z. Phys. **A125**, 197, (1986).

[Simp87] J. Simpson *et al.*, J. Phys. **G13**, 847, (1987).

[Simp91] J. Simpson *et al.*, J. Phys. **G17**, 511, (1991).

[Simp92] J. Simpson *et al.*, J. Phys. **G18**, 1207, (1992).

[Simp05] J. Simpson, J. Phys. **G31**, S1801, (2005).

[Simp09] J. Simpson, *Private Communication.*

[Th92a] K. Theine *et al.*, Nucl. Phys. **A536**, 418, (1992).

[Th92b] K. Theine *et al.*, Nucl. Phys. **A548**, 71, (1992).

[Toth75] K.S. Toth, W.-D. Schmidt-Ott, C.R. Bingham and M.A. Ijaz, Phys. Rev. **C12**, 533, (1975).

[Tw86] P. J. Twin *et al.*, Phys. Rev. Lett. **57**, 811, (1986).

[WM73] M.J. Weber and R.R. Monchamp, J. Appl. Phys. **44**, 5495, (1973).

[WS54] R.D. Woods and D.S. Saxon, Phys. Rev. **95**, 577, (1954).

[Wyss88] R. Wyss, J. Nyberg, A. Johnson, R. Bengtsson and W. Nazarewicz, Phys. Lett. **B215**, 211, (1988).